Diagnosing Energy Transfer in an Idealized Ocean-Atmosphere Model: A Frequency-Domain Approach

by

Paige Martin

A dissertation submitted in partial fulfillment
of the requirements for the degree of
Doctor of Philosophy
(Physics)
in The University of Michigan
2019

Doctoral Committee:

Associate Professor Brian K. Arbic, Co-Chair
Professor Charles R. Doering, Co-Chair
Associate Professor Robert D. Deegan
Associate Professor Andrew McC. Hogg, Australian National University
Associate Professor Christiane Jablonowski

Handstanding at the ocean-atmosphere interface.

Paige E. Martin

paigemar@umich.edu

ORCID ID: 0000-0003-3538-633X

For the future of our planet Earth

ACKNOWLEDGEMENTS

First and foremost, special thanks are due to my advisor, Brian Arbic. His guidance, patience, and mentorship have helped shape me into the scientist that I am today. He has been an attentive advisor who, no matter how busy he was, always made time to meet with me regularly (in person or virtually), and is astonishingly good at responding to emails. In addition to being an advisor for my research, he helped make several formative opportunities available to me, including (but not limited to) the GFD program at Woods Hole Oceanographic Institute, leadership roles in the American Geophysical Union, and teaching at the Coastal Ocean Environment Summer School in Ghana.

I would like to thank the members of my dissertation committee for their comments on this document, and for taking the time to serve on my committee. I would also like to recognize my Physics co-advisor, Charlie Doering, who was always available if help was needed, and who has always been responsive to my yearly emails to fill out the annual report for the department. Additionally, I would like to thank Prof. Andy Hogg who, for the last two years of my PhD has acted as another advisor to me, hosting me twice at the Australian National University (ANU), taking the time to hold regular video meetings when I wasn't in Australia, and providing very insightful contributions to the science in this dissertation. I am also extremely grateful for the helpful discussions and virtual meetings with Dr. Andrew Kiss (ANU) over the last two years, and for his simple yet elegant explanations of difficult concepts. There are several co-authors and other researchers who have contributed greatly to the sci-

ence and technical aspects of this thesis: Bill Dewar, James Munroe, Jeff Blundell, Amanda O'Rourke, Aidan Heerdegen, Bruno Deremble, and many others who have given valuable feedback at talks and conferences.

I am so grateful to my high school math teacher, Elizabeth Jockusch, who gave me the confidence and strong mathematical background that has led me down the PhD path, and who also inspired in me the joy of mathematics. I also want to acknowledge Prof. Dr. Dr. h.c. mult. Jürgen Kurths at the Potsdam Institute for Climate Impact Research (PIK), who introduced me to the wonderful world of mathematical modeling of the climate sciences, and to the German Academic Exchange Service (DAAD) for funding that year of research. Thank you also to my former PIK colleagues who converted me into a Python enthusiast.

Words don't quite do justice to the ways in which my parents have helped me get to where I am today. Through all of the ups and downs along the PhD path, they have always been constant pillars of support and have helped me in whatever way they could, including (but certainly not limited to) reading through portions of this dissertation. As academics themselves, they provided a wonderfully inspiring example of the curiosity and creativity that comes with being a researcher. I am ever so grateful to my grandmother, Mama, who is the shining example of a strong female role model, exemplifying intelligence, strength, and kindness. She and my late grandfather, Papa, have played a major role in my life, from supporting me through my undergraduate studies to providing a swimming pool in which an impressively large portion of my childhood was spent. Thanks also to my inspiring brother, Reed, who is and always has been the coolest person I know. I also owe my gratitude to Peter Varela, who has helped me believe in my own abilities as a scientist (and as a person in general) and who has used his Australian wit and charm to bring light into my life these last few years.

Although I've been the sole Ann Arbor-based member of the Arbic Lab during my

last year, many thanks are due to the previous lab members who made coming into work an enjoyable and constant learning experience. In the last year especially, my productivity has been bolstered by the Wednesday Writing Workshops (which gradually expanded to be nearly every day of the week) I had with friends in other graduate programs at coffee shops around Ann Arbor, and which also provided a network of understanding and encouragement through the PhD process. I am indebted to the Graduate Program Coordinators in both the Physics Department (Lauren Segall) and the Earth and Environmental Sciences Department (Anne Hudon) for helping guide me through all of the requirements of my degree. I also think it prudent to recognize the many activities that have helped me stay happy and healthy throughout my graduate studies: The Penny Seats Theatre Company, The Encore Musical Theatre Company, all of my theatrically-inclined friends, UM Club Gymnastics, Chalmers McGillivray and the rest of the partner acrobatics community in the Ann Arbor area, all of my aerial training partners, and the Friday Friz crew. And of course, thanks to my dog Willow (and former dog Maple) for always being excited to see me.

I would like to acknowledge the funding sources that have supported me throughout my PhD: the National Science Foundation (NSF) Graduate Research Fellowship under grant DGE 1256260 and the associated Graduate Opportunities Worldwide that allowed me to spend several months at the ANU, NSF grants OCE-0960820 and OCE-1351837, the University of Michigan African Studies Center, and the M-Cubed program, the latter supported by the Office of the Provost and the College of Literature, Science, and the Arts. The model and analysis codes in this dissertation were run on the National Computational Infrastructure (NCI), which is supported by the Australian Government, and I am very thankful for the helpful NCI staff that were especially lenient regarding my disk usage while in the final stages of my PhD. Thanks are also due to the Python computing language and the Jupyter framework that made writing and running code so much fun (most of the time).

TABLE OF CONTENTS

LIST OF FIGURES

Figure

LIST OF TABLES

Table

ABSTRACT

Climate variability is an area of great interest. The ocean and atmosphere, two major components of the climate system, are inherently coupled, and there has been recent interest in deciphering whether oceanic and atmospheric variability is primarily due to intrinsic processes driven by nonlinear advection, due to forcing from the other fluid, or due to the inherently coupled nature of the ocean-atmosphere system. In this work, we investigate the oceanic, atmospheric, and coupled sources of variability by calculating a frequency-domain spectral transfer diagnostic, applied to the energy budget of a coupled ocean-atmosphere model.

Spectral transfers are particularly well-suited to study energy transfer, as they are able to pick out energy sources and sinks from specific terms in the energy budget, as a function of (in this study) frequency. While the majority of previous literature on spectral transfers is in the wavenumber domain, our work focuses instead on the frequency domain to investigate how the transfers of energy vary across timescales. We use the Quasi-Geostrophic Coupled Model (Q-GCM; *Hogg et al.* 2014) - an idealized, turbulent, eddy-resolving, double-gyre ocean coupled to a channel atmosphere. The simplified nature of Q-GCM allows for the quantification of all terms in the energy budget, and additionally allows for the adjustment of coupling parameter strength. Spectral transfers are applied to the Q-GCM energy budget over timescales ranging from 2 days to 100 years, and reveal the relative magnitudes of energy sources and sinks in each fluid. We then attribute the observed behavior as driven by either intrinsic or forced dynamics.

In both the ocean and the atmosphere in the fully coupled model configuration,

nonlinear advection of kinetic energy is found to be the dominant source of low-frequency variability, while potential energy advection is the largest source at high frequencies. In the ocean, we identify dynamically distinct regions that display strikingly different behavior: the western boundary current separation is found to be a large source of energy in the ocean at all frequencies, while the western boundary itself is a substantial sink of energy at nearly all frequencies. We argue that there is an important connection between these two regions, whereby energy generated in the current separation region is dissipated along the western boundary, with both regions characterized primarily by intrinsically-driven ocean variability.

Motivated by the finding that the ocean (at non-eddy-resolving scales) only affects the atmosphere at long timescales (*Bjerknes*, 1964; *Gulev et al.*, 2013), we are particularly interested in determining if the inclusion of eddies in our turbulent model will reveal a high-frequency ocean imprint in the atmosphere. We run a partially coupled and an atmosphere-only configuration of Q-GCM in order to start identifying the mechanisms responsible for certain behavior in each fluid. Overall, the energy transfer terms appear quite robust to changes in model coupling; however, there are some interesting differences. Ocean-driven variability is found at a timescale of 17 years that is seen throughout the atmosphere only when it is fully coupled to an ocean model. We also find that eddy interactions in the ocean appear to damp high-frequency atmospheric energetics by up to 10%. The exact mechanism responsible for this high-frequency behavior is still under investigation, but our results, in contrast to traditional results with a non-eddying ocean, indicate that ocean eddies can impact the atmosphere at daily timescales.

CHAPTER I

Introduction

According to the Oxford English Dictionary, the word "climate" is defined as "the weather conditions prevailing in an area in general or over a long period" (*Oxford English Dictionary online*). At the root of its definition, then, the importance of both length scales (in reference to "area[s] in general") and time scales ("over a long period") is apparent. Climate variability is the term used to describe the spatial and temporal fluctuations of the climate system. As quoted by the World Meteorological Organization, climate variability refers to the "variations in the mean state and other statistics of the climate on all temporal and spatial scales" (*World Meteorological Organization website*). It goes on to state that "variations may be due to natural internal processes within the climate system (internal variability), or to variations in natural or anthropogenic external factors (external forcing)." This thesis employs the same idea of framing climate variability in terms of forced and intrinsic factors, with a focus on behavior across timescales.

Within the climate system, however, we can essentially ask the same question about internal versus external sources of variability. The Earth's climate is made up of many different systems, with the largest contributors typically considered to be the atmosphere and the hydrosphere (the oceans plus other water masses like rivers, lakes, etc.). Other important aspects of the climate system include the cryosphere

(ice), land, and the biosphere (the combined effect of ecosystems), as well as human society. The climate system is incredibly complex, and the interactions between each of its components are incredibly difficult to study, with the inherent influence from each of the other components. In this work, we choose to simplify the situation by looking only at oceanic and atmospheric variability, in an attempt to decipher how big of a role each plays in the coupled climate system. As a further simplification, we will only consider a single ocean basin double-gyre configuration (i.e. an ocean whose basin-wide motion is characterized by two large circular currents), such as the North Atlantic Ocean, and the atmospheric strip around the globe that is just above such an ocean basin. This idealized setup allows us to more easily isolate the behavior from specific mechanisms in the ocean or atmosphere.

1.1 Brief Background on Forced Versus Intrinsic Behavior in Ocean-Atmosphere Modeling

The idea of disentangling climate variability due to intrinsic versus forced behavior spans several decades. Forty years ago, the scientist considered to be the "father of chaos theory" (*MIT News Office*, 2008) Ed Lorenz wrote a paper entitled "Forced and Free Variations of Weather and Climate" (*Lorenz*, 1979). In that paper, he classifies forced behavior of the weather and climate systems to be very large-scale, such as changes in solar input, while the intrinsic behavior are phenomena such as cyclones, that occur due to instabilities in the system itself. A recent example (from just last year) of differentiating behavior due to forcing or internal dynamics is found in *Wills et al.* (2018) who quantify Pacific sea surface temperature variability due to internal (ocean-atmosphere dynamics) vs external (global warming) factors.

In this study, when we refer to forced versus intrinsic behavior, we consider each fluid individually. That is, when discussing the ocean, intrinsic motions would be

those that arise from pure ocean dynamics, while forced motions would be those driven by the atmosphere. We also recognize a third option of behavior arising from purely coupled behavior, i.e. that exists only when the two fluids are coupled together.

There are several methods that have been used in previous studies to distinguish between the dynamics in either the ocean or the atmosphere. Perhaps the most obvious method, and one that has been used extensively in the literature, is running either ocean or atmosphere models with different degrees of forcing from the other fluid. This kind of analysis has been implemented from both ends of the climate modeling spectrum - from the atmospheric side of the field with varying ocean forcing, and from the oceanic side by varying the atmospheric forcing.

On the atmospheric side, for example, many previous studies have applied the idea of varying the mechanism or strength of the coupling in ocean-atmosphere models in order to determine the role that coupling plays in driving climate variability. Several papers from the 1990s (e.g. *Manabe and Stouffer* 1996; *Bladé* 1997; *Barsugli and Battisti* 1998) ran atmosphere general circulation models (GCM) with differing levels of ocean coupling: (1) with prescribed sea surface temperature (in a sense "uncoupled") and (2) coupled to an ocean model (either an ocean GCM or a slab ocean mixed-layer model). The results from these papers agree that coupling does affect the atmosphere, namely that coupling with the ocean increases the air surface temperature variance when compared with the uncoupled scenarios. Furthermore, *Manabe and Stouffer* (1996) and *Barsugli and Battisti* (1998) both find that thermal coupling accounts for most of the coupled behavior, and conclude that the ocean's primary effect on the atmosphere is via heat fluxes, rather than mechanical coupling of ocean dynamics. As we discuss later, this and similar results have come into question with eddy-resolving ocean models, that is, models that explicitly resolve the small-scale vortical motions in the ocean.

On the ocean side, there have been numerous studies that have investigated the

ocean's sensitivity to different atmospheric forcing, with specific interest in diagnosing intrinsic ocean variability. For instance, *Dewar* (2003) responds to an idea from previous literature at the time that the ocean responds mostly linearly to atmospheric forcing. By running a suite of idealized ocean models with periodic forcing at different timescales, as well as with stochastic forcing, the authors show that nonlinearities in the ocean are important in more realistically forced simulations, and suggest the importance of ocean dynamics in decadal midlatitude climate variability. *Penduff et al.* (2011) and *Sérazin et al.* (2015) run a global ocean model with both a time-varying seasonal forcing and a mean annual cycle. In this way, they compare the interannual variability of each run and interpret that of the time-mean forcing to be indicative of intrinsic interannual ocean variability (since any variability must necessarily stem from internal ocean dynamics if the forcing does not introduce variability at those timescales). Both studies find that large-scale, low-frequency variability is mostly driven by the atmosphere, with the exception of high-eddying regions that are more intrinsically driven. An argument for the inclusion of both nonlinearity in the ocean and variable forcing is made in *Kiss and Frankcombe* (2016) by running an idealized gyre model under different wind forcing (varying the time-mean and frequency). They find that resulting timescales in the western boundary current of the ocean model can include timescales greater than the forcing of a steadily driven current. This result agrees with the results of *Penduff et al.* (2011) and *Sérazin et al.* (2015), who argue that the high eddying regions are dominated by intrinsic ocean variability.

Another, and more basic way of studying internal dynamics of, say, the ocean is merely by considering the terms associated with ocean circulation to be of intrinsic origin. This is a straight-forward assumption in cases where there is a prescribed atmospheric forcing that can be written out as a single term in the equations. In *Arbic et al.* (2012) and *Arbic et al.* (2014), for example, the authors run an idealized ocean model with a prescribed mean flow that is represented by a single term in

the governing equations. In their energy budget analysis, therefore, they can easily distinguish forced behavior (the forcing term in the equation) from intrinsic variability (e.g. kinetic energy advection). With more complicated coupling mechanisms, as in the fully coupled model used in the present work, the distinction between forced and intrinsic terms is less clear. The coupling terms interact with oceanic and atmospheric dynamics in unexpected ways, and it is hard to tease apart the underlying mechanisms of each term in the energy budget.

Here, we employ both of the previously mentioned methods to disentangle oceanic from atmospheric behavior in a coupled model. First, we do an energy budget analysis that reveals all of the terms that contribute energy into and out of the system; these terms must all balance in order to conserve energy in the model. This separates out the different energetic processes (e.g. kinetic energy advection, potential energy advection, bottom drag, stress, etc.), some of which can be attributed to internal or external dynamics (as in, e.g., *Arbic et al.* 2014). For instance, the advection of oceanic kinetic energy is considered to be a term generated internally by the ocean. Of course, there could be underlying drivers of this kinetic energy advection, which leads us to the second method in which we diagnose forced and intrinsic dynamics. After running the model in a fully coupled mode, we run the model in a partially coupled, as well as an atmosphere-only configuration. By still applying the same spectral technique to the energy budgets in each fluid, we can start to pick apart the sensitivity of each fluid's dynamics to coupling and to the opposing fluid, and how the sensitivity manifests in each term in the energy budget. A similar partially coupled framework has been applied to the same model as used here in *Hogg et al.* (2006), as well as in a realistic, global, coupled model in *Larson et al.* (2018).

Going back to the definition of climate cited above, it seems likely that the way in which the ocean and atmosphere interact will depend upon the scale - spatial or temporal - at which we study. Largely motivated by *Bjerknes* (1964) and *Gulev*

et al. (2013), we choose to focus our attention on the temporal dependence of ocean-atmosphere variability. We are also motivated by the recent work on turbulence indicating the existence of a temporal analog of the well-established spatial inverse cascade of energy (*Arbic et al.*, 2012, 2014; *Sérazin et al.*, 2018). In the literature on turbulence, analysis on temporal scales has been less studied than those on spatial scales, and so we hope that this work can contribute to the temporal literature.

The literature on the temporal variability of the climate system is rich with the characterization of climate variability modes with specific timescales. At the high-frequency end there are tides (at daily or half-daily timescales), midlatitude weather systems at scales of roughly 3 to 7 days, and the seasonal cycle on a yearly timescale (e.g. *Dijkstra and Ghil* 2005). At lower frequencies there are a number of climate modes that have been identified, including the El Nio Southern Oscillation (ENSO) near 5 years, the Pacific Decadal Oscillation near 50 years, and the North Atlantic Oscillation on timescales ranging from seasonal to interdecadal (*Hurrell and Deser*, 2010; *Feliks et al.*, 2016). Of the modes of variability listed above, the model used in this thesis does not have tides or seasonal variation. Due to the equatorial Pacific origin of ENSO, our model will not show ENSO variability either. However, midlatitude weather systems are present in this work, and the model could have modes that resemble the NAO or PDO as well, though we do not address this question directly and future work identifying spatial patterns of variability would be necessary to verify this claim.

As stated above, one of the motivations of this study comes from *Bjerknes* (1964), who found that the atmosphere drives the ocean (specifically, the sea surface temperature field) at short timescales (interannual and shorter), while the ocean plays more of a role in driving sea surface temperature (and thus likely also the atmosphere) at longer timescales. *Gulev et al.* (2013) provide observational evidence to corroborate Bjerknes' theory. However, an obvious drawback in the observational

data in *Gulev et al.* (2013) is its poor oceanic spatial resolution of 5° longitude by 5° latitude (roughly comparable to 500-kilometer resolution on a rectangular grid in the midlatitudes), which does not resolve mesoscale ocean dynamics such as eddies (whose length scales are typically less than 100 km) (*Vallis*, 2006). Recently, it has been shown (*Penduff et al.*, 2011) that increasing model resolution and thus resolving ocean eddies increases the (specifically low-frequency) variability of the ocean, and unlocks more intrinsic ocean variability than was previously thought. This finding that ocean eddies can have a significant impact on the ocean's low-frequency variability has sparked recent interest in understanding exactly how ocean eddies affect atmospheric dynamics and climate variability. There is therefore a renewed interest in considering intrinsic ocean dynamics as a possible driver of climate variability, particularly through momentum (in addition to thermal) coupling. In this work, we investigate the temporal dependence of coupled climate variability via the identification of energy sources and sinks using an eddy-resolving model.

1.2 Spectral Transfer Methods

Spectral analysis of geophysical fluid dynamics is a helpful method to organize the system in terms of spatial or temporal scales. When data is collected, whether from observations or from a model, it is typically packaged in terms of location grid points and time series. When visualizing raw time and space data, it is difficult to see how many scales are present in the system, and to what degree each scale impacts the system. Spectral methods use a Fourier transform to analyze the data in wavenumber (in units of inverse length) and/or frequency (in units of inverse time) domains, which essentially reorganizes the data into spatial scales and/or temporal scales. In the process, any information about specific locations or time stamps is lost, but the ability to see which spatial and temporal scales play the largest roles in the data is revealed.

Spectral analysis has often been used to study turbulence in fluids. From the pioneering theoretical work by *Kolmogorov* (1941) on 3D turbulence, as well as the seminal turbulence work in two dimensions (e.g. *Fjørtoft* 1953, *Batchelor* 1953, *Kraichnan* 1967, 1971), turbulence in geophysical fluids has been, and still is, a topic of great interest. One of the distinguishing factors of classical 2D turbulence is the existence of an inverse cascade of kinetic energy from small to large spatial scales. This inverse cascade theory was found to exist even in the presence of stratification and rotational effects, referred to as geostrophic turbulence (*Charney*, 1971; *Salmon*, 1980; *Vallis*, 2006). This quasi-2D turbulence was shown observationally by *Scott and Wang* (2005), who used satellite sea surface height measurements to prove the existence of an inverse cascade in the real ocean. Even though the ocean and atmosphere are three-dimensional, their horizontal dynamics can be characterized by 2D turbulence, at sufficiently large scales, and under stratification and rotational effects.

The idea of using the spectral transfer method on geophysical fluids (the primary method used in this work) goes back to the work by *Saltzman* (1957). Barry Saltzman is an important figure, particularly in the atmospheric sciences, and is considered "the father of modern climate theory" (*Maasch et al.*, 2005). In a paper from work done as a graduate student (*Saltzman*, 1957), Saltzman converts the governing equations for atmospheric flow from normal grid space into wavenumber space, and then goes on to derive cross spectral equations made up of the products of two functions, which we refer to as spectral transfer equations in this dissertation, or as cross spectral diagnostics, as in *Hayashi* (1980). In addition to his spectral decomposition contributions to the field, Saltzman set the stage for using energetics as the primary metric to understand geophysical fluid properties. *Hayashi* (1980) develop a different way to calculate cross spectra that is simpler and more widely applicable (e.g. to the frequency domain, and not just the wavenumber domain) than *Saltzman* (1957), and it is the Hayashi framework that we use in this work.

Spectral energy transfers, as opposed to, for example, energy spectra, are useful for identifying the sources and sinks in a system. Because they are defined as cross spectra, they are the product of terms, and thus reveal the contribution that each term plays in the energy budget of the fluid. The sign of the spectral transfer term indicates whether the term is a source or a sink of energy in the system, and the relative magnitudes of each term indicate which terms remove or input more energy. The properties of spectral transfers in both wavenumber and frequency space are investigated and discussed in detail in *Morten* (2015). We note that spectral transfers are the divergence of spectral fluxes (*Arbic et al.*, 2014) and that both spectral transfers and fluxes are employed in the literature. In this work, we choose to display our results as spectral transfers, as we feel that they better reveal the sources and sinks of each term visually.

Spectral transfers (and fluxes) have been used in numerous other studies prior to this one, though primarily in the wavenumber domain (*Salmon*, 1978, 1980; *Hua and Haidvogel*, 1986; *Larichev and Held*, 1995; *Scott and Wang*, 2005). *Arbic et al.* (2012, 2014) apply the spectral transfer/flux theory to demonstrate the existence of a temporal equivalent of the inverse energy cascade, namely that energy at short timescales gets transferred to longer timescales. Just last year, two more studies (*O'Rourke et al.*, 2018; *Sérazin et al.*, 2018) have used frequency-domain spectral transfers to study coupled ocean-atmosphere behavior.

More specifically, *Arbic et al.* (2012, 2014) apply the frequency-domain spectral transfer technique to a full energy budget of an idealized, homogeneous, two-layer, geostrophic turbulence model, with prescribed baroclinically unstable background flows. They also investigate the surface kinetic energy (KE) advection term in a realistic ocean model, as well as a satellite altimeter product. *Sérazin et al.* (2018) use the same spectral technique applied to a realistic ocean model, but use two different atmospheric forcing fields, one with minimal time-dependence, and one with the full

spectrum of atmospheric time scales. By comparing the two model runs with differing atmospheric forcing they are able to draw conclusions about the intrinsic versus forced sources of variability. However, they look only at the surface kinetic energy term driven by nonlinear advection. *O'Rourke et al.* (2018) also apply frequency-domain spectral transfer diagnostics but to a realistic fully coupled ocean-atmosphere model, and examine the behavior of the wind stress, in addition to the surface KE advection. This thesis and associated papers seek to fill the gap left open by these four papers — we use a more complicated idealized ocean model than *Arbic et al.* (2012, 2014), and couple it with a fully dynamic atmosphere. Our model is complex in that it is dynamically inhomogeneous and is a fully coupled model but, unlike in *O'Rourke et al.* (2018), *Sérazin et al.* (2018) and the realistic model in *Arbic et al.* (2012, 2014), it is simple enough to easily permit explicit calculation of all of the terms in the energy budget.

1.3 Overview

The research presented in this dissertation follows several previous studies, as discussed in the preceding section. To make clear the contribution of this work compared to previous studies, we provide a graphic (see Figure 1.1) that highlights the model complexity (on the y-axis) and the number of terms in the energy budget that can be calculated (on the x-axis). As visible in Figure 1.1, what sets this work apart from previous studies using the same technique, is that we apply the technique to a model that is the most complex of the idealized models previously used, which still allows us to explicitly calculate every term in the energy budget. Furthermore, our work is novel in that, to our knowledge, we are the first to apply frequency-domain spectral transfers to the atmospheric energy budget in a coupled system, and we are the first to combine the technique with partial coupling of the model.

In chapter II we introduce the model that is used in this work: the Quasi-

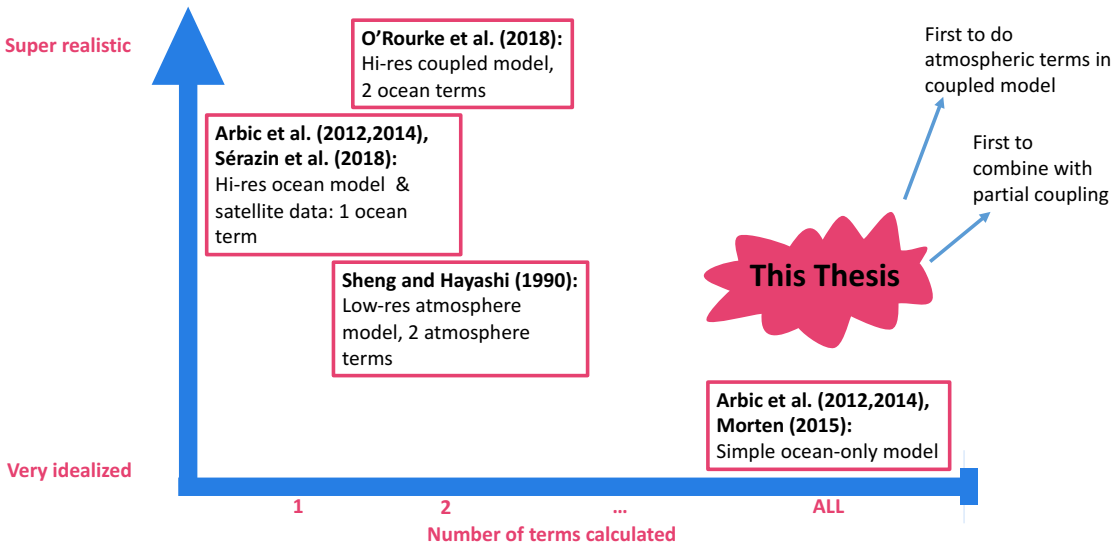

Figure 1.1: Stylized graph showing the context of the work in this thesis, compared to previous studies that have applied the frequency-domain spectral transfer diagnostic to ocean and atmosphere models/data. The y-axis shows the increasing complexity of the model used, while the x-axis displays the number of terms in the energy budget that are explicitly calculated.

Geostrophic Coupled Model (Q-GCM; *Hogg et al.* 2014). In chapter III, we derive the spectral transfer diagnostic that is used to diagnose sources and sinks of energy in the fully coupled Q-GCM energy budget of both the ocean and atmosphere. Within chapter III, when we run a fully coupled Q-GCM, we use these spectral transfer terms applied to the energy budget to discuss forced versus intrinsic variability. That is, we discuss how the behavior of, say, the oceanic kinetic energy advection term is an intrinsic term to the ocean, while the wind stress term is a forcing from the atmosphere. We show the spectral transfers as a function of frequency, for timescales from 2 days up to 100 years, and averaged across the entire domains of each fluid. To get a better idea of the spatial distribution of these spectral transfers, we plot spatial maps of some of the spectral transfers, which reveal that there are distinct regional differences within the ocean domain. We thus divide the oceanic basin into regions - the western boundary, the western boundary current separation, and the remainder of the domain - and plot the regionally area-integrated spectral transfers as functions of frequency. We discuss the results from this analysis and offer some possible insights into the source of the observed behavior.

Chapter IV builds upon the results from chapter III. We apply the same spectral transfer technique to two different configurations of Q-GCM: a partially coupled mode (which differs from the fully coupled configuration in only one way), and an atmosphere-only mode. The partially coupled mode removes the communication from ocean dynamics to the sea-surface temperature, while the decoupled atmosphere run is forced by a climatological sea surface temperature (SST) field. We show a similar set of spectral transfer results as for the fully coupled setup in chapter III for each of these configurations and discuss the similarities and differences, and the physical implications. The middle chapters of this dissertation are portrayed as a flowchart in Figure 1.2 in order to display to the reader how the chapters are linked together.

Finally, we briefly summarize the results of this thesis, and offer some conclusions

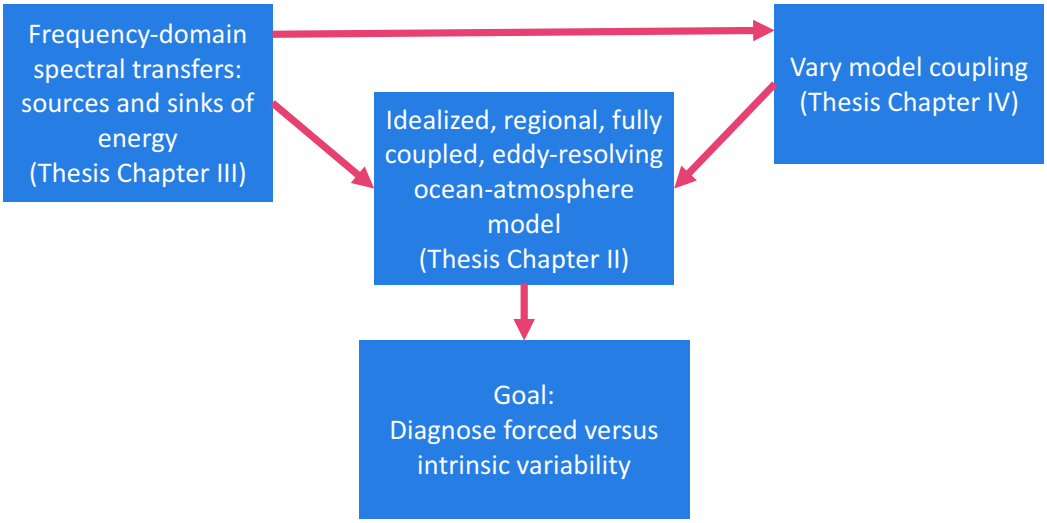

Figure 1.2: Flowchart displaying how the chapters in this thesis link together.

for how this work has contributed to the field, and some further directions that could be taken.

CHAPTER II

Quasi-Geostrophic Coupled Model

The numerical model used to generate the output used for analysis in this work is the Quasi-Geostrophic Coupled Model (Q-GCM). While more details of Q-GCM will be discussed at the start of each chapter, it seems prudent to discuss the model in general terms in its own chapter, since it pertains to everything that follows.

2.1 Model Setup

We use version 1.5.0 of the Quasi-Geostrophic Coupled Model (Q-GCM; *Hogg et al.* 2014), which is a fully coupled, quasi-geostrophic, ocean-atmosphere model, to investigate the sources and sinks of oceanic and atmospheric variability. Q-GCM is a regional model, made up of a box ocean that we have configured to resemble the North Atlantic Ocean (i.e. a double gyre configuration) coupled to an atmosphere. The atmosphere is a reentrant channel, that spans the circumference of the Earth at 40°N. Each fluid consists of three quasi-geostrophic (QG) vertical layers, as depicted in Figure 2.1. We choose three layers as it has been found (e.g. in *Hogg et al.* 2006) that three layers are necessary and sufficient to produce semi-realistic baroclinic instability, and thus yield stronger eddies than, say, in a two-layer configuration. The model is run on a beta-plane, with no bottom topography, and is forced solely by temporally and zonally constant, but latitudinally varying solar radiation, with no

diurnal or seasonal variation. We recognize that the removal of seasonal variation is unrealistic, but we are particularly interested in variability in the two fluids without contamination from the frequencies due to seasonal variations.

Q-GCM has been previously used for various projects, including *Hogg et al.* (2006), who used Q-GCM to study coupled modes of variability, and *Farneti* (2007), who investigated coupled Rossby waves. In this study, we choose Q-GCM because it is well-suited for studying low-frequency variability, can resolve geostrophic eddies in both the ocean and atmosphere, allows us to calculate each term in a closed energy budget, and is computationally cheap to run compared to many large-scale coupled climate models.

Before we proceed, we provide a very brief description of quasi-geostrophy, a key dynamical assumption of Q-GCM. Quasi-geostrophy is an extension of geostrophy, which assumes that a fluid is in a steady state characterized by a balance between the pressure gradient force and the Coriolis force. Quasi-geostrophy describes a fluid that is in near geostrophic balance, but that includes the advective terms in the momentum equation governing the fluid movement (e.g. *Vallis* 2006). In a QG fluid, it is assumed that vertical motions are small and the variations in the Coriolis parameter are assumed to be small and nonzero (hence why quasi-geostrophy is well-suited to study the mid-latitudes). The quasi-geostrophic equations permit us to assume near-geostrophic balance while at the same time permitting prognostic time evolution, in contrast to the diagnostic case of pure geostrophic balance.

The ocean-atmosphere coupling in Q-GCM is accomplished through mixed layers that are embedded into the first layers (the layers at the ocean-atmosphere interface) of each fluid. The incoming solar radiation varies latitudinally and ranges from 260 to 180 Wm^{-2}, on par with the global average of actual incoming solar radiation of roughly 150 to 250 Wm^{-2} (*Vallis*, 2006), as the latitude increases northward from near 20°N to 60°N. This shortwave solar radiation is deposited into the ocean

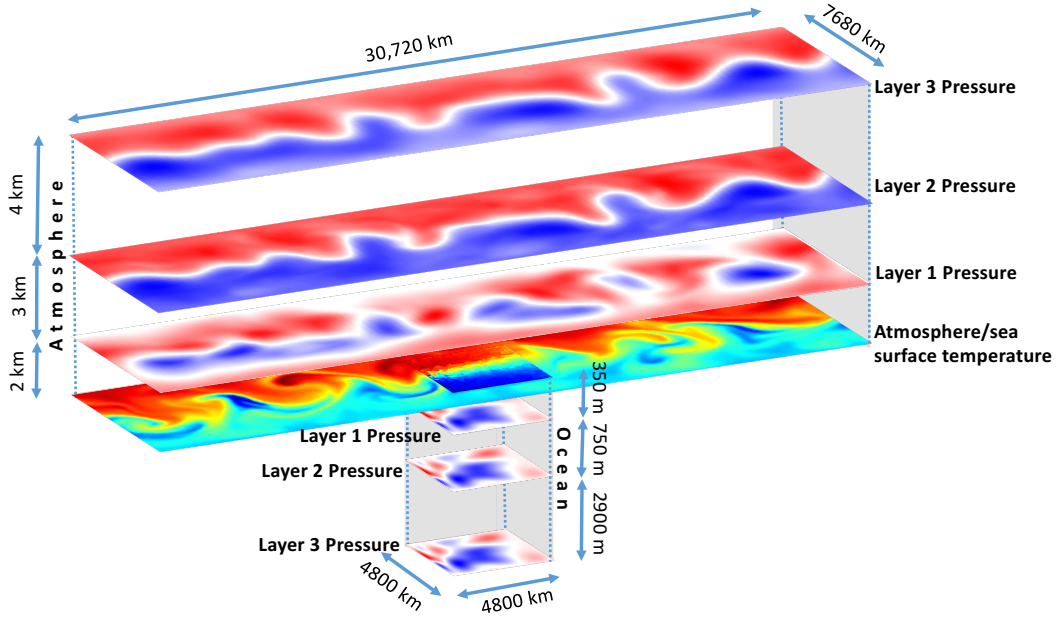

Figure 2.1: An exploded view of the Quasi-Geostrophic Coupled Model setup used in this paper. Layers are shown with snapshots of pressure for each of the three layers in the ocean and atmosphere, and snapshots of surface temperature for each fluid at the ocean-atmosphere interface. Note that the vertical axis is not drawn to scale.

mixed layer, and re-emitted as long-wave radiation into the atmospheric mixed layer and QG layers. The mixed layers also allow for the vertical transport of heat, via parameterized radiation and convection schemes, as well as wind stress via Ekman pumping.

The atmospheric channel in the model displays an eastward jet with eastward propagating waves through the center of the channel, with some westward motions in the northern and southern portions of the domain. The ocean portion of the model shows a double-gyre configuration, with a subtropical gyre and a subpolar gyre, and a strongly eddying western boundary current separation (meant to mimic the Gulf Stream) between the two gyres. This strong current in the ocean roughly aligns with the peak of the atmospheric jet, which occurs where the wind stress curl changes sign. Snapshots with overlaid average contours of pressure and potential vorticity in both the ocean and atmosphere are shown in Figure 2.2. We note that throughout this manuscript the variable we refer to as "pressure" is in fact the pressure divided by density (the latter of which is a different constant for each fluid; values are given in Table 2.1), which behaves like a streamfunction. In fact, the pressure variable p used here is related to streamfunction ψ merely by the Coriolis constant f_0: $p = f_0\psi$. Quasi-geostrophic equations are often written in terms of streamfunction ψ, but due to their linear relationship we will proceed using the pressure variable p.

2.2 QG Layer Governing Equations

Following *Hogg et al.* (2014), the Q-GCM governing equations are written in terms of potential vorticity conservation, with potential vorticity $\mathbf{q}$ and pressure $\mathbf{p}$:

$$\begin{aligned} \frac{\partial}{\partial t}\mathbf{q} &= \frac{1}{f_0}J(\mathbf{q},\mathbf{p}) + \mathbf{Be} - \frac{A_4}{f_0}\nabla^6\mathbf{p} \\ \mathbf{q} &= \beta(y-y_0) + \frac{1}{f_0}\nabla^2\mathbf{p} - f_0\mathbf{Ap}, \end{aligned} \tag{2.1}$$

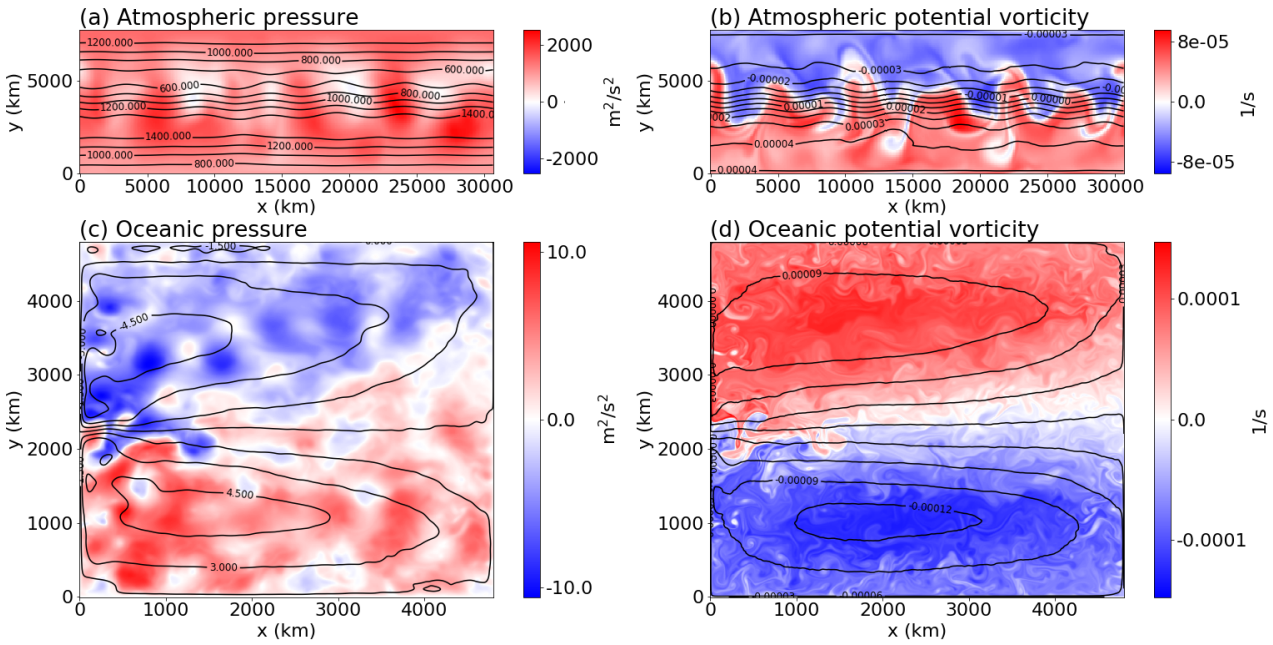

Figure 2.2: Q-GCM layer 1 snapshots (in color) and 20-year averages (black contours) of atmospheric pressure (a) and potential vorticity (b), and oceanic pressure (c) and potential vorticity (d).

with Jacobian J defined as:

$$J(\mathbf{q}, \mathbf{p}) = \left(\frac{\partial \mathbf{q}}{\partial x}\right)\left(\frac{\partial \mathbf{p}}{\partial y}\right) - \left(\frac{\partial \mathbf{p}}{\partial x}\right)\left(\frac{\partial \mathbf{q}}{\partial y}\right) \tag{2.2}$$

where $\mathbf{q} = [q_1, q_2, q_3]$, $\mathbf{p} = [p_1, p_2, p_3]$ (with subscripts indicating vertical layer, and layer numbers increasing away from the ocean-atmosphere interface), t is time, x and y are (respectively) the zonal and meridional coordinates, y_0 is the middle latitude of $40°N$, A_4 is the biharmonic viscosity constant, ∇ is the horizontal gradient operator, and we use the β-plane approximation with $f = f_0 + \beta(y - y_0)$. Other symbols are defined in Table 2.1. In the above equations, $\mathbf{q}$ and $\mathbf{p}$ have been divided by the density of the fluid. The matrices $\mathbf{A}$, $\mathbf{B}$, and vector $\mathbf{e}$ are defined as follows, and superscripts are used to distinguish between ocean (o) and atmosphere (a):

$$ {}^{o}\mathbf{A} = {}^{a}\mathbf{A} = \begin{bmatrix} \frac{1}{H_1 g_1'} & -\frac{1}{H_1 g_1'} & 0 \\ -\frac{1}{H_2 g_1'} & \frac{1}{H_2}(\frac{1}{g_1'} + \frac{1}{g_2'}) & -\frac{1}{H_2 g_2'} \\ 0 & -\frac{1}{H_3 g_2'} & \frac{1}{H_3 g_2'} \end{bmatrix} \tag{2.3} $$

$$ {}^{o}\mathbf{B} = -{}^{a}\mathbf{B} = \begin{bmatrix} \frac{f_0}{H_1} & -\frac{f_0}{H_1} & 0 & 0 \\ 0 & \frac{f_0}{H_2} & -\frac{f_0}{H_2} & 0 \\ 0 & 0 & \frac{f_0}{H_3} & -\frac{f_0}{H_3} \end{bmatrix} \tag{2.4} $$

$$ {}^{o}\mathbf{e} = \begin{bmatrix} {}^{o}w_{ek} \\ {}^{o}e_1 \\ 0 \\ \frac{\delta_{ek}}{2f_0}\nabla^2 p_3 \end{bmatrix} \tag{2.5} $$

$$ {}^{a}\mathbf{e} = \begin{bmatrix} {}^{a}w_{ek} \\ {}^{a}e_1 \\ 0 \\ 0 \end{bmatrix} \tag{2.6} $$

where we have defined Ekman velocity w_{ek} to be proportional to the vertical component of the curl of the wind stress τ:

$$ \begin{aligned} {}^{o}w_{ek} &= \vec{k} \cdot \frac{\vec{\nabla} \times {}^{o}\vec{\tau}}{f_0} \\ {}^{a}w_{ek} &= \vec{k} \cdot \frac{\vec{\nabla} \times {}^{a}\vec{\tau}}{f_0}, \end{aligned} \tag{2.7} $$

where $\vec{k}$ is the vertical unit vector. We use the notation of an arrow over the variable to denote a vector in the (x, y, z, t) space, and a bold-letter notation to indicate a matrix with scalar values for each vertical layer. The oceanic and atmospheric stresses differ only by a factor of the density ratio. Stress is calculated using relative wind (except

in the atmosphere-only run), such that the wind stress depends on the difference between the atmospheric and oceanic surface velocities (*Duhaut and Straub*, 2006). The expressions ${}^{o}e_1$ and ${}^{a}e_1$ are made up of layer temperatures and heat fluxes, as detailed in the following section. The values of constants H_k (layer heights), δ_{ek} (bottom Ekman layer thickness), and g'_i (reduced gravity values at each interface i) are given in Table 2.1, along with descriptions and values of other constants we use. The reduced gravity parameter, defined as the gravity multiplied by the relative density difference between layers (normalized by the mean density), is used in lieu of gravity because in a stratified fluid, horizontal pressure gradients are proportional to relative differences in density between layers (e.g. *Vallis* 2006).

2.3 Mixed Layer Temperature Evolution Equations

The mixed layers in Q-GCM have explicitly defined temporal evolution, given by the following equations with temperature T (anomalous from a constant average value), subscript "m" denoting mixed layer, and superscripts "o" and "a" designating ocean and atmosphere as above:

$$
{}^{o}T_{mt} + \underbrace{\left({}^{o}u_m\,{}^{o}T_m\right)_x + \left({}^{o}v_m\,{}^{o}T_m\right)_y}_{\text{contains horizontal temperature advection}} - \overbrace{\frac{{}^{o}w_{ek}\,{}^{o}T_m}{{}^{o}H_m}}^{\text{vertical temperature advection}} =
$$

$$
\underbrace{\frac{{}^{o}F_0}{\rho^{o}C_p\,{}^{o}H_m}}_{\text{heat flux into and out of ocean mixed layer}} + \overbrace{\frac{F_m^{e+}}{\rho^{o}C_p\,{}^{o}H_m}}^{\text{entrainment heat flux}}
$$

$$
+ \underbrace{{}^{o}K_2\nabla_H^2\,{}^{o}T_m - {}^{o}K_4\nabla_H^4\,{}^{o}T_m}_{\text{diffusion}} \tag{2.8}
$$

$$
{}^{a}T_{mt} + \underbrace{\left({}^{a}u_m\,{}^{a}T_m\right)_x + \left({}^{a}v_m\,{}^{a}T_m\right)_y}_{\text{contains horizontal temperature advection}} + \overbrace{\frac{{}^{a}w_{ek}\,{}^{a}T_m}{{}^{a}H_m}}^{\text{vertical temperature advection}} =
$$

$$
\underbrace{\frac{{}^{a}F_0}{\rho^{a}C_p\,{}^{a}H_m}}_{\text{heat flux at bottom of atmosphere mixed layer}} - \overbrace{\frac{{}^{a}F_m}{\rho^{a}C_p\,{}^{a}H_m}}^{\text{heat flux at top of atmosphere mixed layer}}
$$

$$
+ \underbrace{{}^{a}K_2\nabla_H^2\,{}^{a}T_m - {}^{a}K_4\nabla_H^4\,{}^{a}T_m}_{\text{diffusion}}\,.
$$

Here we have labeled the terms according to their function for ease of understanding. The variables u_m and v_m are zonal and meridional mixed layer velocities, respectively, defined by the sum of a pressure gradient term and a term from Ekman pumping:

$$
\left({}^{o}u_m, {}^{o}v_m\right) = \frac{1}{f_0}\left(-{}^{o}p_{1y}, {}^{o}p_{1x}\right) + \frac{1}{f_0\,{}^{o}H_m}\left({}^{o}\tau_y, -{}^{o}\tau_x\right). \tag{2.9}
$$

New constants here are density ρ, heat capacity C_p, average mixed layer height H_m, and second-order (K_2) and fourth-order (K_4) temperature diffusion coefficients, all given in Table 2.1.

The ocean heat flux terms are defined as follows:

$$ {}^{o}F_0 = -F_\lambda - F_0^{\uparrow} - {}^{o}F_m^{\downarrow} - F_s, \tag{2.10} $$

where

$$ F_\lambda = \overline{F_\lambda} + \lambda({}^{o}T_m - {}^{a}T_m) \rightarrow \text{Sensible and latent heat} \tag{2.11a} $$

$$ F_0^{\uparrow} = \overline{F_0^{\uparrow}} + D_0^{\uparrow o}T_m \rightarrow \text{Oceanic radiative heat} \tag{2.11b} $$

$$ F_m^{\downarrow} = \overline{F_m^{\downarrow}} + D_m^{\downarrow}{}^{a}T_m \rightarrow \text{Atmospheric radiative heat over ocean} \tag{2.11c} $$

$$ F_s(y) = \overline{F_s} + \frac{F_s'}{2}\sin\left(\frac{\pi(y-y_0)}{{}^{a}Y}\right) \rightarrow \text{Incoming shortwave solar radiation} \tag{2.11d} $$

and

$$ {}^{o}F_m^{e+} = -\frac{1}{2}{}^{o}\rho\,{}^{o}C_p w_{ek}({}^{o}T_m - {}^{o}T_1) \rightarrow \text{Entrainment heat flux.} \tag{2.12} $$

The entrainment heat flux is what accounts for the effective vertical heat exchange between layers when their interface changes height. The atmosphere heat fluxes are:

$$ {}^{a}F_0 = \begin{cases} F_m^{\downarrow} + F_\lambda + F_0^{\uparrow} \rightarrow \text{Over ocean} \\ F_s \rightarrow \text{Over land} \end{cases} \tag{2.13} $$

which have all been defined above, and

$$ {}^{a}F_m = F_m^{\uparrow} + F_1^{\downarrow} + {}^{a}F_m^{e-} \tag{2.14} $$

where

$$F_m^{\uparrow} = \overline{F_m^{\uparrow}} + B_m^{\uparrow\,a}\eta_m + D_m^{\uparrow\,a}T_m \rightarrow \text{Upward atmospheric mixed layer radiation} \tag{2.15a}$$

$$F_1^{\downarrow} = \overline{F_1^{\downarrow}} + A_{1,1}^{\downarrow\,a}\eta_1 + A_{1,2}^{\downarrow\,a}\eta_2 + B_1^{\downarrow a}\eta_m \rightarrow \text{Downward atmospheric layer 1 radiation} \tag{2.15b}$$

$${}^{a}F_m^{e-} = \overline{{}^{a}F_m^{e-}} + {}^{a}\phi_m\eta_m \rightarrow \text{Atmospheric entrainment heat flux} \tag{2.15c}$$

We have kept our notation consistent with that of *Hogg et al.* (2014) in that positive (negative) heat flux terms denote an upward (downward) transport of heat. The up- (down-) arrows are used to specify heat fluxes that are emitted and absorbed at the top (bottom) of the specified layer. The horizontal overbars are time means, A, B, and D are radiative constants, ϕ_m is a mixed layer constant, η_i is the interface height between layers i and $i+1$, and $\eta_m = {}^{a}h_m - {}^{a}H_m$ (the difference between the evolving and the average atmospheric mixed layer heights).

In the atmopshere, in addition to a time-evolving mixed layer temperature, it is necessary to have an evolving mixed layer height (h_m) as well (in order to avoid an instability due to large vertical heat transfer):

$${}^{a}h_{mt} + ({}^{a}u_m\,{}^{a}h_m)_x + ({}^{a}v_m\,{}^{a}h_m)_y = -{}^{a}e_m, \tag{2.16}$$

where

$${}^{a}e_m = \frac{{}^{a}\phi_m\eta_m}{{}^{a}\rho\,{}^{a}C_p({}^{a}T_1 - {}^{a}T_m)}. \tag{2.17}$$

The ocean and atmosphere entrainment vectors e_1 from Equations (2.5) and (2.6) and are defined as:

$$ {}^{o}e_1 = -\frac{{}^{o}T_m - {}^{o}T_1}{2(T_1 - T_2)} w_{ek} \tag{2.18a} $$

$$ {}^{a}e_1 = \frac{F_m^{\uparrow} + F_1^{\downarrow}}{{}^{a}\rho^{a} C_p ({}^{a}T_2 - {}^{a}T_1)}. \tag{2.18b} $$

The ocean and atmosphere have resolutions of 5 and 80 km, respectively, and the model is run for a total of 400 years after a 50-year spin-up period. The time resolution is 3 minutes in the atmosphere, and 9 minutes in the ocean, and the output is in daily snapshots. The Q-GCM parameters of reduced gravity, layer thicknesses, Coriolis parameters, and basin size have been tuned to mimic the North Atlantic Ocean double-gyre circulation and the atmosphere at those same latitudes. We set a constant value of pressure along each of the ocean boundaries that varies in time, and use a mixed condition on the non-periodic boundaries in the atmosphere, such that there is a different value of pressure at the north and south boundaries. For derivatives of pressure on all solid boundaries, we use a partial slip condition based on the value of a constant α_{bc} (included in Table 2.1). A more thorough explanation of the model's mixed boundary conditions can be found in Appendix C of *Hogg et al.* (2014). For more detailed information about Q-GCM in general, we refer the reader to *Hogg et al.* (2003, 2014).

The parameter set used in this thesis is displayed in Table 2.1. The parameters were tuned by Drs. Jeffrey Blundell and Chris Wilson (personal communication, May 19, 2015), using the same procedure as described in Section 2.1 of *Wilson et al.* (2015), which in turn was based on *Flierl* (1978).

Table 2.1: Q-GCM constants

Parameters	**Ocean Values**	**Atmosphere Values**
Basin dimensions	4800 km x 4800 km	30720 km x 7680 km
Number of grid points	960 x 960	384 x 96
QG layer thicknesses (H_1, H_2, H_3)	350 m, 750 m, 2900 m	2000 m, 3000 m, 4000 m
Average mixed layer thicknesses (H_m)	100 m	1000 m
Timestep	9 min.	3 min.
Bottom Ekman layer thickness (δ_{ek})	1 m	–
Reduced gravities (g_1', g_2')	0.015 ms^{-2}, 0.0075 ms^{-2}	1.2 ms^{-2}, 0.4 ms^{-2}
Biharmonic viscosity (A_4)	$2 \times 10^9 \text{m}^4\text{s}^{-1}$	$1.5 \times 10^{14} \text{m}^4\text{s}^{-1}$
Mean Coriolis parameter at $40°N$ (f_0)	9.37456×10^{-5} s^{-1}	9.37456×10^{-5} s^{-1}
y-derivative of Coriolis parameter (β)	1.75360×10^{-11} $\text{m}^{-1}\text{s}^{-1}$	1.75360×10^{-11} $\text{m}^{-1}\text{s}^{-1}$
Mixed boundary condition parameter (α_{bc})	0.2	1.0
Density (ρ)	1000 kg m^{-3}	1 kg m^{-3}
Heat capacity (C_p)	1×10^3 $\text{Jkg}^{-1}\text{K}^{-1}$	4×10^3 $\text{Jkg}^{-1}\text{K}^{-1}$
Temperature diffusion coefficients (K_2, K_4)	200 m^2s^{-1}, 2×10^9 m^4s^{-1}	2.5×10^4 m^2s^{-1}, 2×10^{14} m^4s^{-1}

CHAPTER III

Spectral Energy Transfers in a Fully Coupled Configuration

3.1 Introduction

As discussed in Chapter I, there has been recent interest in deciphering whether oceanic and atmospheric variability is primarily due to forced or to the intrinsic behavior in each fluid. The inherently coupled nature of the ocean-atmosphere system makes it difficult to tease apart the mechanisms underlying oceanic and atmospheric variability. In this chapter, we run the fully coupled version of Q-GCM and identify energy budget terms associated with intrinsic and forced behavior to address the following question: is the variability in the ocean/atmosphere "free" (intrinsic), "forced" (by the opposing fluid), or intrinsically coupled? This question, with particular interest in showing the existence and importance of low-frequency intrinsic ocean variability, has been discussed by many previous studies (e.g. *Dijkstra and Ghil* 2005; *Quattrocchi et al.* 2012; *Kiss and Frankcombe* 2016; *Dewar* 2003; *Hogg and Blundell* 2006; *Berloff et al.* 2007a,b; *Kravtsov et al.* 2006; *Penduff et al.* 2011; *Sérazin et al.* 2015; *Huck et al.* 2015).

This chapter follows recent studies using frequency-domain spectral transfer techniques to diagnose intrinsic versus forced ocean variability (*Arbic et al.*, 2012, 2014;

O'Rourke et al., 2018; *Sérazin et al.*, 2018). Spectral energy transfers are used here to diagnose energy sources and sinks in a fully coupled Q-GCM, in which we address both oceanic and atmospheric variability. As described in Chapter I, spectral transfer analysis is a useful tool for picking out the sources and sinks for each term in the energy budget. Unlike the majority of previous literature focused on spatial scales, we follow *Arbic et al.* (2012, 2014), *Sérazin et al.* (2018), and *O'Rourke et al.* (2018) in calculating frequency-domain spectral transfers. This chapter in particular is meant to fill a gap left open by these three papers, where we use a reasonably complex and coupled model, while still being able to explicitly calculate all of the terms in the energy budget. To determine the origin of the system's behavior, this chapter employs the method of attributing individual terms in the energy budget to forced motion (directly influenced by the opposing fluid) or intrinsic motion (depending only on the same fluid's variables).

In this chapter, we apply the frequency-domain spectral transfer diagnostic to the energy budget of the fully coupled Q-GCM in order to quantify, as a function of frequency, the relative importance of each of the terms in the energy budget, including intrinsic nonlinear advection and forcing from each fluid. Furthermore, we investigate different spatial regions in the ocean — along the western boundary and the western boundary current separation — that display distinct dynamics, and compare how the sources and sinks of energy differ from one region to the next. In Section 3.2, we derive the spectral transfer equations. In Section 3.3, we discuss results from energy spectra and the spectral transfers. We examine domain-integrated transfers over all frequencies and spatial maps of transfers integrated over defined frequency bands. Finally, in Section 3.4, we offer some physical interpretations of the results.

3.2 Methods: Spectral Transfer Analysis

We analyze output from the Quasi-Geostrophic Coupled Model (described in Chapter 2) using frequency-domain spectral transfer equations, as used in *Arbic et al.* (2012, 2014), *O'Rourke et al.* (2018), *Sérazin et al.* (2018), *Morten* (2015), *Hayashi* (1980), and *Saltzman* (1957). To derive the spectral transfer equations, we first need to obtain the energy tendency equations for both the ocean and the atmosphere. We note that the temperature and mixed layer height equations will not be used explicitly in this thesis. We start with the governing equations given in Equation (2.1) in the previous section, and rewrite them in terms of pressure only:

$$\begin{aligned}\nabla^2\left(\frac{\partial}{\partial t}\mathbf{p}\right) - f_0^2\frac{\partial}{\partial t}\mathbf{A}\mathbf{p} = -\beta\frac{d\mathbf{p}}{dx} + \frac{1}{f_0}J(\nabla^2\mathbf{p},\mathbf{p}) - f_0 J(\mathbf{A}\mathbf{p},\mathbf{p}) \\ +f_0\mathbf{B}\mathbf{e} - A_4\nabla^6\mathbf{p}.\end{aligned} \tag{3.1}$$

To derive the remainder of the calculations, we continue by writing out only the first layer ocean equation, and consequently omit the "o" superscript. All other layers in both fluids follow nearly identical steps. Rewriting equation (3.1) for ocean layer 1 yields

$$\begin{aligned}\nabla^2\left(\frac{\partial}{\partial t}p_1\right) = \frac{f_0^2}{H_1 g_1'}\frac{\partial}{\partial t}(p_1 - p_2) - \beta\frac{dp_1}{dx} + \frac{1}{f_0}J(\nabla^2 p_1, p_1) + \frac{f_0}{H_1 g_1'}J(p_2,p_1) \\ +\frac{f_0^2}{H_1}(w_{ek} - e_1) - A_4\nabla^6 p_1.\end{aligned} \tag{3.2}$$

We now take the Fourier transform of this equation in time:

$$a = \sum_{x,y,\omega}\widehat{a}(x,y,\omega)e^{i\omega t}, \tag{3.3}$$

where a is an arbitrary function, and $\widehat{a}$ is its Fourier transform. If we rewrite the terms in this form, and divide both sides by $e^{i\omega t}$, we are left with (omitting the summation symbol for readability):

$$i\omega\nabla^2\widehat{p_1} = i\omega\frac{f_0^2}{H_1 g_1'}(\widehat{p_1} - \widehat{p_2}) - \beta\frac{d\widehat{p_1}}{dx} + \frac{1}{f_0}J(\widehat{\nabla^2 p_1}, p_1) + \frac{f_0}{H_1 g_1'}J(\widehat{p_2, p_1}) + \frac{f_0^2}{H_1}(\widehat{w_{ek}} - \widehat{e_1}) - A_4\nabla^6\widehat{p_1}. \tag{3.4}$$

To obtain an equation for the energy tendency of the system, we first multiply Equation (3.4) by $\widehat{p_1}^*$, where the star indicates the complex conjugate. We also multiply the complex conjugate of Equation (3.4) by $\widehat{p_1}$, and then add the two equations together and divide by two, collecting terms using the property $\frac{a^*b + b^*a}{2} = \mathrm{Re}[a^*b]$ (where $\mathrm{Re}[x]$ is the real part of x):

$$\frac{1}{2}i\omega\left(\widehat{p_1}^*\widehat{\nabla^2 p_1} - \widehat{p_1}\widehat{\nabla^2 p_1}^*\right) = i\omega\frac{f_0^2}{2H_1 g_1'}(\widehat{p_2}^*\widehat{p_1} - \widehat{p_2}\widehat{p_1}^*) - \beta\,\mathrm{Re}\left[\widehat{p_1}^*\frac{d\widehat{p_1}}{dx}\right] + \frac{1}{f_0}\mathrm{Re}\left[\widehat{p_1}^* J(\widehat{\nabla^2 p_1}, p_1)\right] + \frac{f_0}{H_1 g_1'}\mathrm{Re}\left[\widehat{p_1}^* J(\widehat{p_2, p_1})\right] + \frac{f_0^2}{H_1}\mathrm{Re}\left[\widehat{p_1}^*\widehat{w_{ek}}\right] - \frac{f_0^2}{H_1}\mathrm{Re}\left[\widehat{p_1}^*\widehat{e_1}\right] - A_4\,\mathrm{Re}\left[\widehat{p_1}^*\widehat{\nabla^6 p_1}\right]. \tag{3.5}$$

The same steps are followed for the remainder of the layers to produce equations similar to Equation (3.5) for every layer in both the ocean and the atmosphere. To obtain thickness-weighted equations, we multiply each layer equation by the constant $\frac{H_n}{H_1+H_2+H_3} = \frac{H_n}{H_{tot}}$, with n denoting layer. Since the system is in steady state, we can assume that the time derivative of energy (the term on the left-hand-side of the equation) is zero. We then sum all of the layers together to yield energy budget equations in the ocean and in the atmosphere. We note that the first term on the right-hand-side of Equation (3.5) sums to zero across all layers in the thickness-weighted sum.

The final step is to take the area integral to find an equation in terms of frequency only. The β term drops out upon domain-integration, and we are left with the final spectral transfer equation for the ocean (where we have multiplied through by $\frac{1}{f_0^2}$ to

yield units of $\frac{m^2}{s^3}$):

$$0 = \int\int \Bigg(\underbrace{\frac{1}{f_0^3 H_{tot}} \sum_{n=1}^{3} H_n \,\mathrm{Re}\left[\widehat{p_n}^* J(\widehat{\nabla^2 p_n}, p_n)\right]}_{\text{Advection of KE, layer n}} + \underbrace{\frac{1}{f_0 g_1' H_{tot}} \sum_{i=1}^{2} \mathrm{Re}\left[\widehat{(p_{i+1} - p_i)}^* J(\widehat{p_{i+1}, p_i})\right]}_{\text{Advection of PE, interface i}}$$
$$+ \underbrace{\frac{1}{H_{tot}} \mathrm{Re}\left[\widehat{p_1}^* \widehat{w_{ek}}\right]}_{\text{Wind stress}} - \underbrace{\frac{1}{H_{tot}} \mathrm{Re}\left[\widehat{(p_2 - p_1)}^* \widehat{e_1}\right]}_{\text{Buoyancy forcing}} - \underbrace{\frac{\delta_{ek}}{2 f_0 H_{tot}} \mathrm{Re}\left[\widehat{p_3}^* \widehat{\nabla^2 p_3}\right]}_{\text{Bottom drag}}$$
$$+ [\text{biharmonic viscosity}] \Bigg) dxdy. \tag{3.6}$$

The spectral transfer equation for the atmosphere is very similar:

$$0 = \int\int \Bigg(\underbrace{\frac{1}{f_0^3 H_{tot}} \sum_{n=1}^{3} H_n \,\mathrm{Re}\left[\widehat{p_n}^* J(\widehat{\nabla^2 p_n}, p_n)\right]}_{\text{Advection of KE, layer n}} - \underbrace{\frac{1}{f_0 g_1' H_{tot}} \sum_{i=1}^{2} \mathrm{Re}\left[\widehat{(p_{i+1} - p_i)}^* J(\widehat{p_{i+1}, p_i})\right]}_{\text{Advection of PE, interface i}}$$
$$+ \underbrace{\frac{1}{H_{tot}} \mathrm{Re}\left[\widehat{p_1}^* \widehat{w_{ek}}\right]}_{\text{Bottom drag}} - \underbrace{\frac{1}{H_{tot}} \mathrm{Re}\left[\widehat{(p_2 - p_1)}^* \widehat{e_1}\right]}_{\text{Buoyancy forcing}} + [\text{biharmonic viscosity}] \Bigg) dxdy. \tag{3.7}$$

Note the different definitions behind the terms titled "Bottom drag" between the ocean and atmosphere. For details about integrating over the domain and the handling of boundary conditions we refer the reader to Appendix E of *Hogg et al.* (2014).

These spectral transfer equations allow us to determine whether each term is a source or sink of energy at a given frequency. Additionally, the relative magnitudes of the transfers indicate the terms that contribute more or less to the spectral energy budget at each frequency. It should be noted, that this diagnostic alone does not reveal specific information about how the energy is transferred from a specific term or frequency to any other. However, we can infer some directionality of the energy transfer based on the shape of the curves, as we discuss in the next section. We also wish to point out the terms that we consider to be intrinsic to each fluid. The

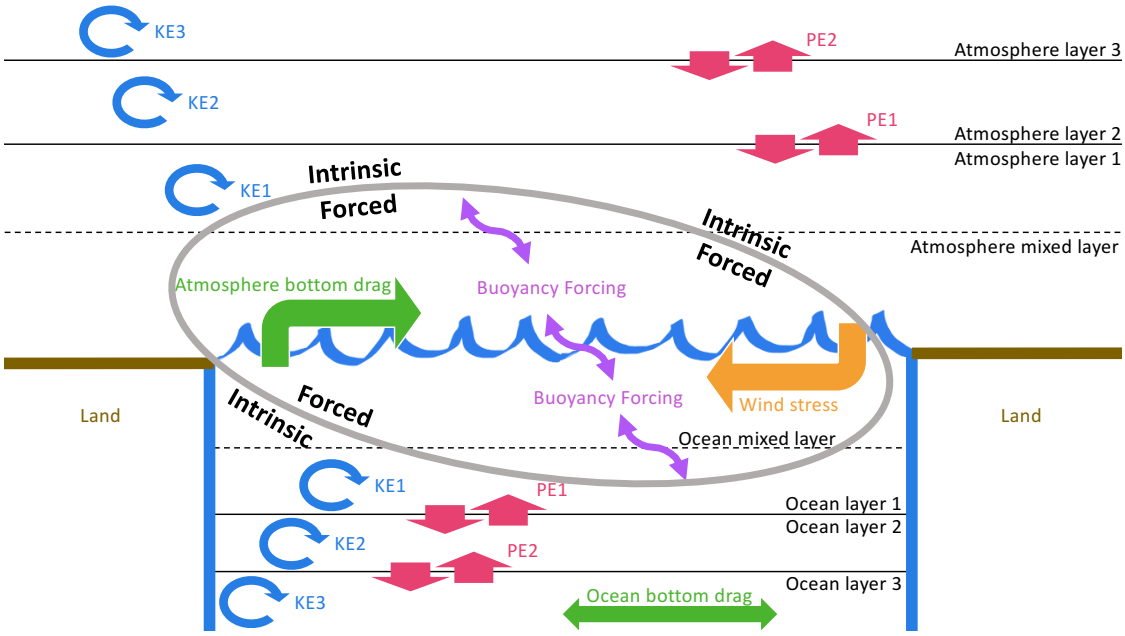

Figure 3.1: A diagram showing where the spectral terms act in the model, as well as which terms are considered intrinsic versus forced. The kinetic (potential) energy advection terms are abbreviated KE (PE) with their associated layer number.

kinetic energy advection terms are interpreted to be the largest indicator of intrinsic variability in each fluid. The potential energy advection in both fluids and bottom drag term in the ocean are also considered to be intrinsic, since they do not depend directly on atmospheric variables. The stress ("bottom drag" in the atmosphere) and buoyancy terms (the latter of which depend on air-sea heat fluxes and mixed layer temperatures) are interpreted as the forced terms in our discussion. A diagram illustrating the forced and intrinsic spectral transfer terms, as well as the location of action of the transfer terms in the model is given in Figure 3.1.

These equations are applied to the Q-GCM output for periods of 100 model years,

in order to capture decadal variability in the ocean. With a 400-year model run, we average over seven overlapping 100-year windows to get better statistical significance, particularly in the lower frequencies. Before the Fourier transform is applied to the data, we apply a detrending to remove any trends that are present in the model output and a Tukey window function (with a taper-to-constant ratio of 20%) in the time-domain of the data to account for its non-periodicity.

We want to make clear that this work exclusively addresses the frequency-dependence of ocean-atmosphere variability. By detrending the data (removing the time-mean), we have gotten rid of any explicit contribution from the time-mean. Thus, a major source of variability in the system, the instability of the time mean flow, does not play an explicit role in this analysis. Our goal is to understand how different mechanisms redistribute energy in the time-variable flow.

Before moving on to the results, we wish to highlight the great effort that was spent on the computation of these spectral transfers. The computational cost for calculating the spectral transfer diagnostics is quite high, particularly for long timeseries. The problem arises when taking the Fourier transform of 100 years of daily data, since the full timeseries is needed to do this computation. We found that calculating the full 3-dimensional matrices in (x,y,t) required more memory than was available on the computer we used (the National Computational Infrastructure supported by the Australian Government). Therefore we split the data into chunks in (x,y), but then ran into trouble with the opening and closing of files taking impractical amounts of time. We thus made use of Dask - a library to aid with parallelized computing in Python. Dask is extremely powerful, in that it uses schedulers to assign small chunks of computation to unused memory, such that it dynamically allocates memory as needed and scales the computations according to the system being used. It interfaces with many of the common Python packages, including Numpy (used here) via Dask Array (*Dask Website*). This computational aspect of this thesis was made possible

through help from Prof. James Munroe, who is currently at Memorial University of Newfoundland in Canada.

3.3 Results

3.3.1 Kinetic Energy Spectra

The domain-integrated kinetic energy spectra of each layer in both the atmosphere and ocean are shown in Figure 3.2. The domain-integrated spectra are calculated according to the equation:

$$\int\int \frac{1}{2f_0^2} \left| \nabla_H \widehat{p_1(x,y,\omega)} \right|^2 dxdy. \tag{3.8}$$

The grey lines show the spectra of the seven 100-year periods discussed in the previous section, and the colored lines are the average over these seven periods. The black dashed lines on the right-hand-side of each plot have a slope of -2. This line is included to compare our results with section 8.5 in *Tennekes and Lumley* (1972) which shows that, analogous to the classic Kolmogorov argument in wavenumber space, frequency-domain slopes in 2D turbulent flows have a -2 slope. (Note on terminology: though we are using the term "spectra" throughout this dissertation, we have in fact plotted spectral density, i.e. the energy spectra divided through by the spacing between frequencies—see section 8.6.2 of *Stull* 1988.)

In the atmosphere (Figure 3.2a), layer 3 follows a slope of -2 at high frequencies, with layer 2 exhibiting a slightly shallower slope, and layer 1 even shallower. We speculate that this behavior stems from the buoyancy terms communicating heat fluxes from the atmosphere mixed layer into layer 1 and disrupting the classical turbulent cascade behavior. At a frequency corresponding to a period of 20 days, we observe a peak in all of the spectra that is roughly at the timescale it takes for waves to cross the atmospheric basin. At all lower frequencies the shapes of the energy spectra

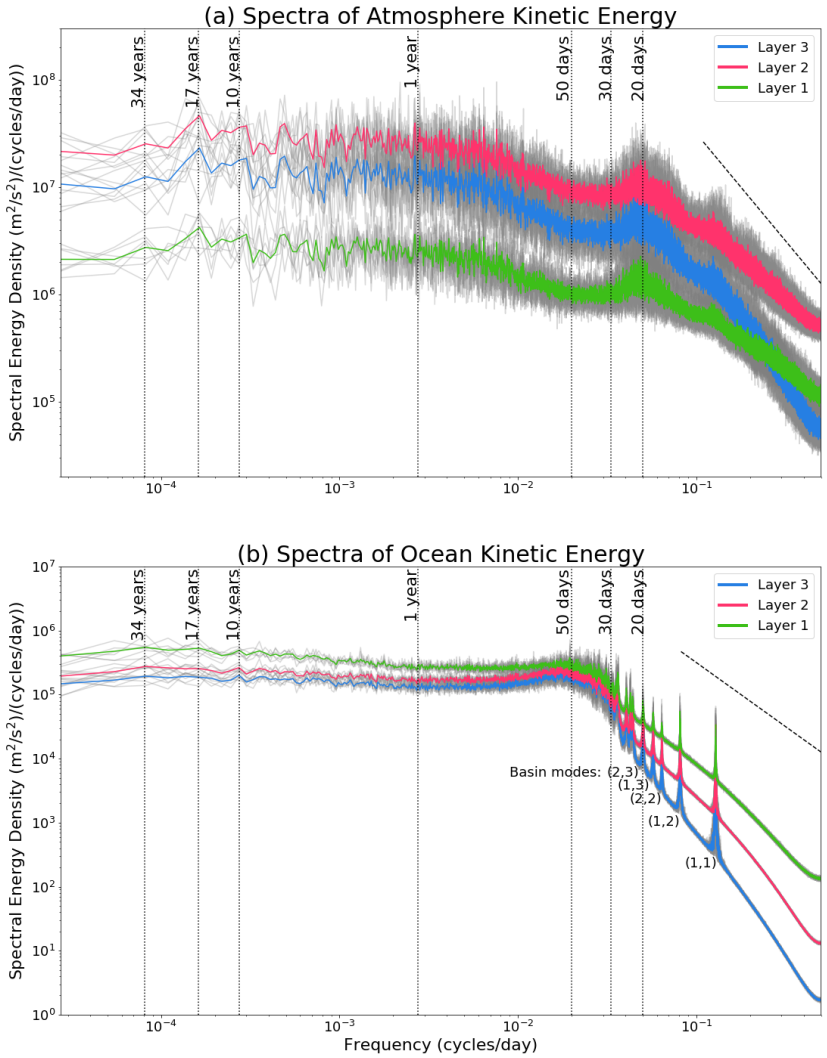

Figure 3.2: Domain-integrated kinetic energy spectra of the three layers in the atmosphere (a) and the ocean (b). The grey lines are of each 100-year analysis, and the colored lines show the average over the seven 100-year periods. Basin mode peaks are labeled in (b) with their corresponding wavenumbers (m,n). The dashed line in each figure has the theorized 2D-turbulent regime slope of -2.

in each layer are nearly identical. It is worth noting that these spectra have been weighted by layer thickness. Thus, we see that layer 2 harbors the most energy of any layer. Layer 1 spectral values are an order of magnitude smaller than either layer 2 or 3, which is likely due to bottom drag over the ocean and land points.

In the ocean (Figure 3.2b), we observe the same slope of -2 in the high frequencies corresponding to about 30 days and shorter. In the ocean, however, it is layer 1 that is the most energetic, while layer 3 is the least energetic. Neither of these results is a surprise, since the first ocean layer is in contact with the dynamic atmosphere, and the third ocean layer experiences the direct effects of bottom drag. An obvious feature of the ocean spectra are the large, narrow peaks in the high frequencies, present in all of the layers. These peaks are due to barotropic Rossby wave basin modes (*LaCasce*, 2002) that are excited due to the geometry of the Q-GCM ocean basin (in this case, a square). Each narrow peak corresponds to the different number of modes in each excited 2D standing wave. We have calculated the theoretical frequencies at which the basin modes should occur in the Q-GCM ocean basin, as given by Equation (5) in *LaCasce* (2002), and found that the locations of the high-frequency peaks in the spectra shown in Figure 3.2b are consistent with the theory to within 2%. The first five modes are labeled in Figure 3.2b as (m,n), where m and n are the wavenumbers in the x- and y-direction, respectively. We have also included (x, y) plots of the distinct spatial patterns of four basin modes in Figure 3.3, for the bottom drag spectral transfer term, since the modes are clearer in this term than in the spectra. We refer the reader to *LaCasce* (2002) for a deeper understanding of these basin modes in geostrophic turbulence models.

3.3.2 Domain-Integrated Spectral Transfers

The domain-integrated spectral transfers in both the ocean and atmosphere are shown in Figure 3.4. The spectral energy budgets are closed in the same way as the

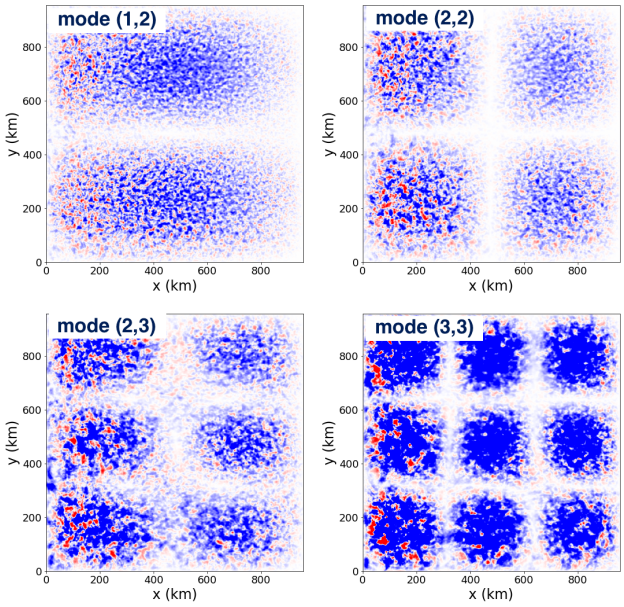

Figure 3.3: The spatial patterns of four basin modes in the spectral transfer of bottom drag.

physical-space energy budgets (i.e. energy is conserved), and the residual (the sum of all terms) is plotted for both fluids to show that the terms balance at each frequency. It should be noted that the biharmonic viscosity term is not included in these plots, as the non-spectral energy budgets revealed that they are of much smaller magnitude than all of the other terms. Additionally, two cells at the non-periodic boundaries are masked in the calculation of the transfers (to ease with derivative calculations). However, the plotted residuals are sufficiently close to zero at each frequency, that we deem the aforementioned effects to be of small enough order to merit neglect.

3.3.2.1 Atmosphere

In Figure 3.4a, which shows the area-integrated spectral transfers in the atmosphere, we observe that the second layer kinetic energy advection (KE2) is the dominant source of energy at all frequencies corresponding to timescales of around 20

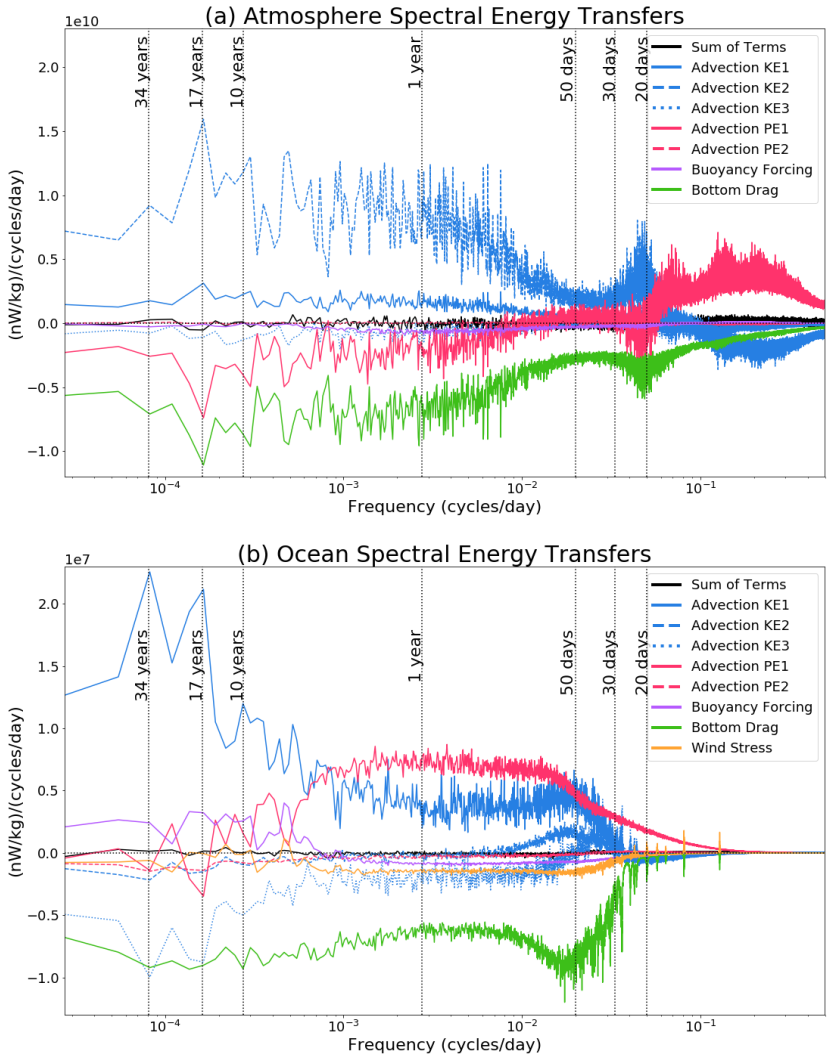

Figure 3.4: Domain-integrated spectral transfers in the atmosphere (a) and ocean (b). The residuals (the sum of all of the terms) in each fluid are shown in black.

days and longer. The same term is also a sink of energy at higher frequencies. This behavior of taking energy out of the system at high frequencies, and adding energy to the system at low frequencies is consistent with the "inverse temporal cascade" seen in *Arbic et al.* (2012, 2014), *O'Rourke et al.* (2018), *Sérazin et al.* (2018), and *Morten* (2015), where energy is transferred from high to low frequencies. We see this same inverse cascade behavior in the advection of first layer kinetic energy (KE1), but with a much smaller magnitude. This behavior can likely be explained by the smaller velocities in atmospheric layer 1 compared with layer 2. We also note that there is a low-frequency peak in KE2 at a timescale of 17 years, which we discuss later as to how this might relate to the ocean variability. The spectral transfer of third layer KE advection (KE3) is not a significant contributor to the overall energy budget of the atmosphere.

The potential energy advection at the first interface (PE1) roughly opposes KE2 (except in the 20-100 day band), with positive values at high frequencies (shorter than around 20 days) in which it also opposes bottom drag, and mostly negative at lower frequencies. This result suggests the presence of a forward cascade of energy — energy is transferred out of the low frequencies and deposited into the high frequencies. This behavior is consistent with *Arbic et al.* (2014), who find that the KE and PE advection terms almost perfectly mirror one another in their idealized ocean-only model. In turn, the mirroring of frequency-domain PE and KE transfers is consistent with the classical paradigm of wavenumber-domain transfers given in *Salmon* (1980) and *Steinberg et al.* (1971). The small, though nonzero magnitude of PE2 suggests that it plays a very small role in the transfer of energy in the system, and we will thus not discuss the term in any more detail.

The primary sink of energy in the atmosphere is the bottom drag. This is to be expected, as this term is designed to extract energy out of the system. At very high frequencies, though, it is KE2 that removes the most energy from the system.

The buoyancy term is very close to zero throughout the frequency domain and thus appears to play a very small role in the transfer of energy across frequencies, but we will come back this term in Chapter IV.

3.3.2.2 Ocean

Figure 3.4b shows the domain-integrated spectral transfers for the ocean portion of Q-GCM. The KE1 term is the dominant term among the layers in the ocean, contrary to the layer 2-dominated atmosphere KE advection. This can be explained by the highest ocean velocities being in ocean layer 1, whereas the highest atmospheric velocities are in layer 2. Like the shape of KE2 in the atmosphere, the shape of the ocean's KE1 spectral transfer with negative values at high frequencies (timescales less than about 30 days) and positive at lower frequencies again implies the existence of the "inverse temporal cascade". KE1 advection is the dominant source of energy at low frequencies, from around a timescale of two years and longer. At timescales longer than around 12 years, there is a noticeable increase in the magnitude of KE1, with two peaks corresponding to timescales of 17 and 34 years. Spectral peaks at nearly the exact same frequencies were also found in *Hogg et al.* (2006) in the first layer ocean height and sea surface temperature fields. The 17-year peak coincides with a peak in KE2 at the same timescale in the atmosphere. We revisit and offer some physical insight on these low-frequency peaks in Sections 3.3.4 and 3.4.

KE2 and KE3 are also negative at high frequencies in the ocean, becoming positive around 30 days. However, they both quickly become negative again for all low frequencies. This spectral transfer shape with positive values in the mid-range, and negative values in both high and low frequencies may indicate that, in layers 2 and 3, KE cascades from both low and high frequencies to the mid-range frequencies. KE3 advection is surprisingly large at timescales longer than around 12 years, when its magnitude roughly matches that of the bottom drag, as they work together to

balance the large low-frequency energy input from KE1. We will look more into why KE3 plays such a large role as a sink in the ocean's energy budget in Section 3.3.4.

PE1 shows a very different shape than in the atmosphere. It is positive at nearly all frequencies, except at the lowest of the frequency range (longer than 12 years), when the term appears to oscillate around zero. The mostly positive values tell us that PE1 is a major source of energy in the ocean at all frequencies up to around 12 years. This behavior differs from both the atmosphere and the behavior seen in *Arbic et al.* (2014), *Steinberg et al.* (1971), and *Salmon* (1980), as it does not appear to indicate a forward cascade, which would mirror the inverse cascade of the first layer KE. The behavior of PE1 advection is discussed further in Section 3.3.4. We will not discuss PE2 much, as it appears to be very close to zero at timescales shorter than about a year. It does, however, act as a non-negligible sink of energy at longer timescales, with a magnitude comparable to KE2.

As expected, and as in the atmosphere, the bottom drag term is negative (removing energy) at all frequencies and opposes KE1 at timescales longer than about 30 days. Shorter than 30 days, bottom drag is mostly compensated by positive PE1 values. At high frequencies, we again observe several sharp peaks due to the barotropic Rossby wave basin modes. In the spectral transfers, the basin modes appear negative in the bottom drag term and are balanced by the wind stress, suggesting that the basin modes are excited by wind variability at their resonant frequency and have their amplitude limited by bottom drag.

We observe that the wind stress in the ocean is negative across nearly the entire frequency domain (except between around 5 and 20 years, when it dips barely above zero several times), implying that the wind stress is removing energy at nearly all timescales. This result may appear counterintuitive, as atmospheric wind is a major source of oceanic variability. However, our spectral transfer plots show the effects of the anomalous wind — what remains after the mean wind contribution has been

subtracted out (this occurs when we detrend the fields in order to take a Fourier transform). Thus, the variations in wind stress appear to be removing energy at nearly all frequencies in the domain, albeit at a relatively small amplitude compared to other terms. This damping of eddy energy by anomalous winds is consistent with the results of other studies, including *O'Rourke et al.* (2018) and *von Storch et al.* (2007). In a paper discussing how winds affect ocean eddies, *Wilson* (2016) explain the mechanism by which relative wind—where the wind stress takes into account the difference in velocities between the atmosphere and ocean (*Duhaut and Straub*, 2006)—systematically damps ocean eddies. We run Q-GCM with relative wind stress, and so the mechanism described in *Wilson* (2016) explains our results. A negative wind stress is also consistent with work by *Renault et al.* (2016), who demonstrate that the use of relative winds to calculate stress in a coupled ocean-atmosphere model can cause the "killing" of ocean eddies, thus acting as a sink of energy in the ocean.

This wind stress transfer term was also calculated in *O'Rourke et al.* (2018), but for the GFDL Coupled Model — a realistic, global ocean-atmosphere model. In their case, shown in Figure 7 of *O'Rourke et al.* (2018) for different regions, the wind stress transfer terms are also largely negative, with two obvious exceptions. The first, seen in most of the regions, is the large positive peak at around a year (with an associated six-month harmonic) due to seasonal contributions. In all regions, however, they observe that wind stress is a source of energy at high frequencies. With no seasonal forcing in Q-GCM, it is not surprising that we see no positive seasonal signatures in the wind stress term in Figure 3.4b. However, we do observe a difference in the high frequencies where the wind stress in Q-GCM remains negative, except for the large, positive, basin mode peaks. We believe that the positive high frequency wind stress in *O'Rourke et al.* (2018) may partially stem from similar basin mode resonances, but for a more complex model with realistic coastlines and bathymetry. More realistic ocean basins experience a continuum of background modes, as it is essentially made

up of many highly irregular basin shapes (*Müller*, 2009). We therefore argue that the positive high-frequency wind stress transfer term seen in *O'Rourke et al.* (2018) may be due to the same mechanisms that give rise to the discrete basin mode spikes in Figure 3.4b of this paper. With a continuum of background modes, the semi-realistic ocean displays a more continuous positive signature for high-frequency wind stress transfer terms, and hence the different behavior of wind stress in our idealized coupled model compared to the GFDL coupled model.

The buoyancy term in Figure 3.4b appears to be a small sink of energy at frequencies exceeding those corresponding to timescales of four years, but a source of energy at lower frequencies. This buoyancy term is where the mixed layer temperatures enter into the energy budget. Since the magnitude of buoyancy is small compared to other terms, we will not discuss it much further in this chapter, but it will play a larger role in the next chapter.

For reference, we calculate a characteristic timescale of the two fluids, based on the deformation radius L_d, that is obtained using the reduced gravity values and layer thicknesses. The deformation radii in this model are calculated in a similar fashion to the idealized two-layer model used in, e.g. *Arbic et al.* (2014), that defines L_d as $\sqrt{\frac{g' H_1 H_2}{f_0^2 (H_1 + H_2)}}$, but for three layers. We calculate a root-mean-square velocity (U_{rms}) using the definition of equation (9) in *Arbic et al.* 2014 for the first layers in each fluid. Then, we calculate L_d/U_{rms} to obtain characteristic timescales of 3.2 days in the ocean, and 1.5 days in the atmosphere. Since we are most interested in eddies, we can multiply these values by 2π to get the effective eddy turnover times, which yields an eddy turnover time of 20.1 days in the ocean and 9.3 in the atmosphere. These timescales fall in the high-frequency regions of each fluid's spectral transfer plot, where the KE advection terms are negative, which agrees with the spectral transfer results in *Arbic et al.* (2014).

To help understand the behavior behind these area-integrated spectral transfer

plots, in the next section we will look at the spectral transfers at individual grid points, before domain integration is performed. There are two primary questions about transfers in the ocean that are especially interesting: (1) Why is PE1 positive across nearly all frequencies, and why does it not counteract KE1? (2) Why is KE3 such a large sink of energy at low frequencies?

3.3.3 Spatial Maps of Spectral Transfers

To get a better intuition for these spectral transfers, we examine their spatial distribution. In the above calculations, we integrated over the (x, y) domain to yield a closed spectral energy budget as a function of frequency. In order to examine regional behavior, we now plot the spatial pattern of specific terms integrated over frequency bands. We refer to these plots as spatial maps of spectral transfer, which are functions of spatial axes x and y, as well as the limits of the frequency band integrated over. Due to restraints on computational resources, we average the Q-GCM output over 5 days in order to calculate the spatial maps, and we thus do not capture the highest frequencies in these maps. We aim to be careful with terminology here, since the spatial integration in the previous section allowed for the cancellation of some of the terms in the equations. For instance, when we refer to the spatial map of kinetic energy advection, we are in fact referring to the spatial map of the contribution to kinetic energy that remains after spatial integration. The purpose of these spatial maps is to help us understand the terms that we observe in the area-integrated spectral transfers, particularly the ocean's PE1, KE1, and KE3.

3.3.3.1 Ocean

Several spatial maps of spectral transfers are shown in Figure 3.5. From left to right, the columns show PE1, KE1, and KE3. The top row displays the domain-integrated spectral transfer terms, with highlighted frequencies indicating the fre-

quency band over which we average to create the spatial maps in the rest of the rows. The frequency bands were chosen to demonstrate the spatial distribution across low frequencies (180 days to 100 years; highlighted in blue and shown in row 2), mid-range frequencies (60-90 days, highlighted in red, shown in row 3), and high frequencies (18-20 days, highlighted in green, shown in row 4). Note that in many cases there is significant cancellation between regions of opposite sign in Figure 3.5 to give the integrated values in Figure 3.4.

First, we observe that both KE1 and PE1 show a very clear signature from the western boundary current separation region, which shows up as a triangular-shaped protrusion from the western boundary near the middle latitude of the domain. This triangular region is distinguishable due to the high magnitudes of energy transfer values across all frequency bands, as well as large-scale solid-color patches in the low- and mid-frequency bands. Interestingly, if we compare the spatial distribution of the signs of the transfer values between KE1 and PE1, we see that they are mostly opposites of one another. In the low-frequency band, KE1 shows positive values in the western boundary current separation, with PE1 showing negative values in the same region. This opposition is even more pronounced in the mid-frequencies with the appearance of a narrow, north-south oriented band of negative transfer (blue) in KE1 and positive transfer (red) in PE1, in the middle of the triangular western boundary current separation region of opposite sign. We argue that this mirroring in sign between the KE1 and PE1 terms is an indication that there is a distinct oppositional relationship between KE1 and PE1, as found in *Arbic et al.* (2014), *Steinberg et al.* (1971), and *Salmon* (1980), but that these relationships are visible only in certain dynamical regions. We note the different colorbar bounds used to plot each transfer, and so the magnitudes vary significantly across terms.

Another region where we see the same kind of opposing behavior is along the entire western boundary of the ocean basin. Especially pronounced in the low-frequency

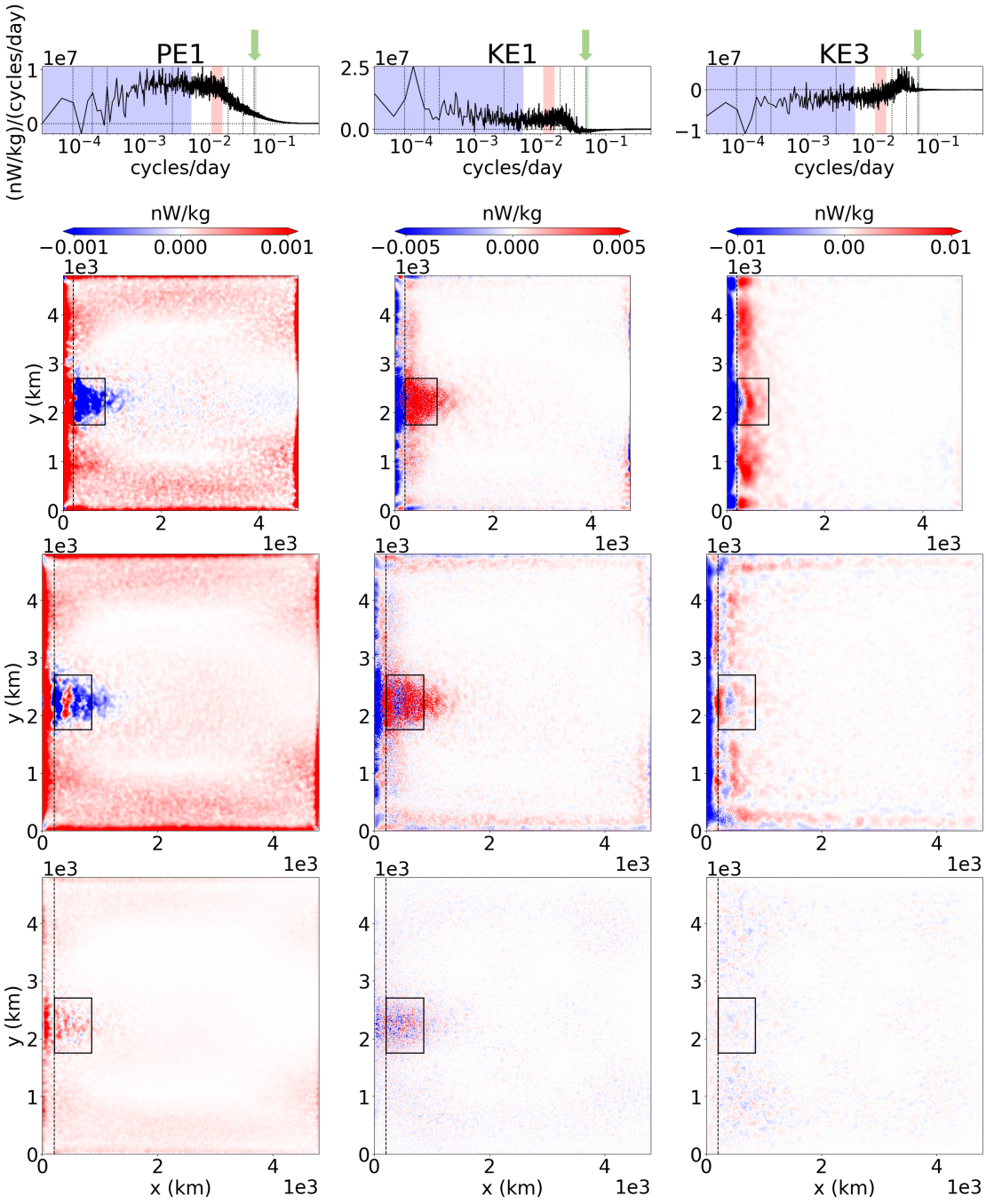

Figure 3.5: Spatial maps of spectral transfers for layer 1 PE advection (1st column), layer 1 KE advection (2nd column), and layer 3 KE advection (3rd column). The top row shows the domain-integrated spectral transfers indicating the three frequency ranges that are averaged over: low frequencies (shaded in blue, 1st row), middle frequencies (shaded in red, 2nd row), and high frequencies (shaded in green and indicated with a green arrow, 3rd row). Note the different colorbar bounds for each column.

band, the western boundary appears to be mostly negative (blue) in KE1, and mostly positive (red) in PE1, indicating that KE1 is a sink and PE1 a source in the western boundary. The mid-frequency band displays some of this behavior, as well, but it is not easily seen in the high-frequencies. However, the western boundary appears to play a very large role in the advection of third layer KE, unlike the current separation region, which is only barely visible as a small bump just to the east of the western boundary. In the low-frequency band of KE3, we observe a negative transfer along the western boundary wall, with a strong positive band of values immediately to the east. The mid-range and high frequencies show noisier signatures, but still display larger magnitudes along the western boundary, relative to the rest of the domain.

There is also a noticeable difference in the spatial scales that are present across frequency bands, particularly in the KE terms displayed in Figure 3.5. In the high-frequency band, the small scales are apparent due to the small alternating patches of positive and negative values. In the mid- and low-frequency bands, small-scale features are still present, but with a larger-scale background signature. It therefore appears that large scales occur preferentially at lower frequencies, but that small scales are present at all frequencies. This preference for broader scales to occur at lower frequencies may be an indication as to why an inverse cascade in temporal space has been shown to accompany the more well-known inverse cascade in wavenumber space. This frequency-dependent difference in spatial scale is also present in the PE1 term, but to a much lesser degree.

3.3.4 Regional Area-Integrated Spectral Transfers

By visual inspection, we split the ocean domain into regions, based on the distinctive spatial signatures in both the western boundary and current separation regions discussed in the previous section. In this section, we will therefore discuss the ocean as the sum of three parts: the western boundary current separation (CS; indicated by

Table 3.1: Indices of regions in spatial maps of spectral transfers

Region	**Bounding Indices: x-axis**	**Bounding Indices: y-axis**
Western Boundary (WB)	40,170	351, 540
Western Boundary Current Separation (CS)	0, 40	0, 960

the black rectangle in Figure 3.5), the western boundary (WB; the portion to the left of the dotted vertical line in Figure 3.5), and the remainder of the domain (ROD). The bounding indices used to define these regions are shown in Table 3.1. Figure 3.6 displays the area-integrated plots for each of these three regions, which were made following the same steps as in Figure 3.4, by taking the average of seven 100-year-long time series with 50-year overlapping windows. Unlike in Figure 3.4, these regional spectral transfers do not each sum to zero, since they are not summed across the entire domain. The non-zero residuals in these regions can be explained by the fact that, for a subregion of the domain, the fluxes coming through the boundaries prevent the terms we are looking at from adding to zero. However, if we were to sum across all three regions, we would obtain the full-domain ocean spectral transfer plot shown in Figure 3.4b. Note also that the vertical scales vary between each plot in Figure 3.6, in order to best illustrate all of the terms in each region.

The spectral transfers in the CS region are shown in Figure 3.6a. KE1 is the clear dominant source of energy throughout nearly the entire frequency range, corresponding to timescales from about 20 days up through 100 years. Furthermore, it appears that the only significant sources of energy come from the KE advection terms in each layer, with nearly all other terms negative throughout most of the frequency range, corresponding to timescales beyond around 20 days. PE1 plays the largest role as a sink, particularly at low frequencies. This plot shows that what we observed in the first two columns of Figure 3.5 with the opposing role of KE1 and PE1, is true for the majority of frequencies in the CS. However, their magnitudes are drastically different,

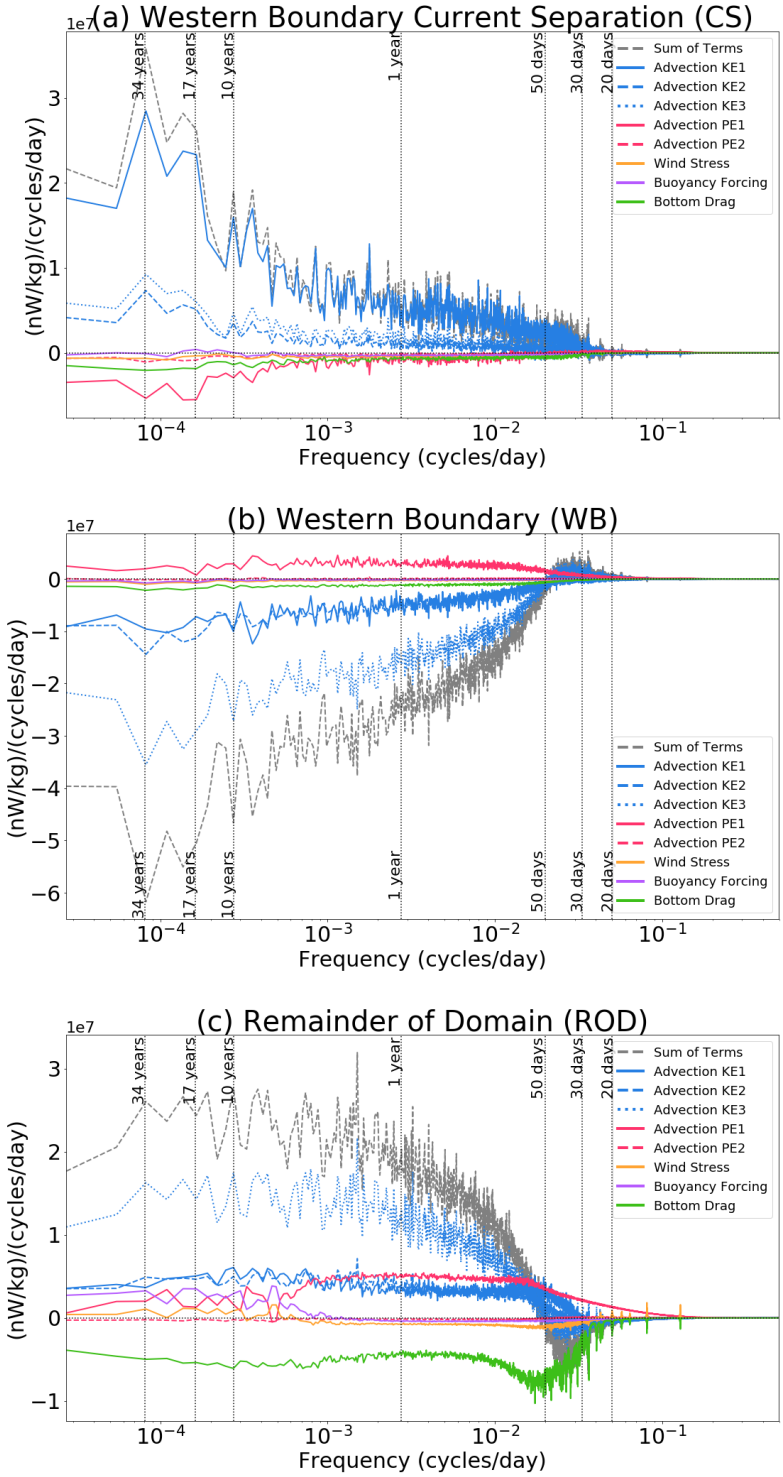

Figure 3.6: Regionally area integrated spectral transfers in (a) the western boundary current separation (CS), (b) the western boundary (WB), and (c) the rest of the domain (ROD). The dashed grey line shows the sum of all the terms in each region.

and they thus do not completely balance one another, as *Arbic et al.* (2014) observed in their doubly-periodic QG ocean model. Here we see that the KE advection terms are of far greater magnitude than the PE advection terms, with KE1 nearly six times the magnitude of PE1.

The WB spectral transfers (Figure 3.6b) show nearly the reverse of what we observed in the CS region. The KE advection terms are all negative at low frequencies (beyond 50 days), while the PE1 term is positive at all frequencies. So, we still observe oppositional behavior at low frequencies between the KE and PE1 advection terms, but with their roles reversed: KE advection is a (very) large sink of energy at the western boundary, whereas PE1 is a significantly smaller, but still the largest, source of energy in the region. Interestingly, the bottom drag and wind stress do not appear significantly different between the CS and WB regions, while the buoyancy term shows slight differences, but is still very close to zero in both regions. One noticeable difference in the western boundary is that there is a pronounced positive range of KE advection at frequencies corresponding to timescales shorter than around 50 days, which we don't see being opposed by PE1 (PE1 remains positive at all frequencies).

The area-integrated spectral transfers for the ROD region are shown in Figure 3.6c. We include this plot mostly to show what the behavior of the ocean terms must be to sum to zero across the entire domain, as shown in Figure 3.4b. The region itself was not chosen for its single type of dynamics, and is much larger than the CS or WB regions; we are thus careful to draw conclusions from the ROD region. Still, it is interesting to see how the terms behave outside of the strongly eddying regions. The third layer KE advection is the largest energy source at timescales of 60 days and longer. This may not be too much of a surprise, given that layer 3 is the thickest ocean layer. Bottom drag acts as the largest sink in the ROD region. In contrast to the CS and WB regions, the wind stress is positive at timescales greater than around two years. We suggest that this may be due to the fact that the ROD region

is less eddy-dominated, and so the wind adds energy to the system. The buoyancy also appears to act as a noticeable source of energy at low frequencies, and looks as though it interacts in opposite ways with PE1. Finally, we note that the barotropic Rossby basin modes are most obvious in this region, as expected given that the ROD region encompasses the majority of the ocean domain.

These regional transfer plots reveal the locations responsible for the large low-frequency energy input via KE1, featuring the two peaks at 17 and 34 years that we observed in the full domain transfer plot in Figure 3.4b. The low-frequency peaks (whether positive or negative) are shown prominently in the CS and WB regions (Figure 3.6a,b), but there is a conspicuous absence of this low-frequency behavior in the ROD region (Figure 3.6c). This observation indicates that the 17-and 34-year peaks are limited to the CS and WB regions. In fact, in ROD the KE1 and KE2 terms are of similar magnitude and appear nearly flat beyond 50 days, suggesting that there is no noticeable low-frequency signal in ROD for those terms. We thus suggest that there is low-frequency variability sourced by nonlinear advection of oceanic KE (dominated by layer 1) in the CS region that gets dissipated along the western boundary, also mostly by KE advection (dominated by layer 3). We will investigate this relationship between CS and WB more in the next chapter.

We also notice that the shapes of the KE curves in all three layers in the CS region appear very similar, at least at low frequencies. With similar behavior that spans the water column, we suggest that this might indicate barotropic behavior in the region. In both the WB and ROD regions, the KE terms have similar peaks and troughs, but are not as similar as seen in CS. At low frequencies, KE2 and KE3 look more similar in WB, while KE1 is noticeably different. This may suggest more baroclinic behavior away from the eddy-active CS region in the ocean.

After splitting the ocean into these three different dynamical regions, it becomes apparent that averaging over the entire ocean domain masks a great deal of variability

within the different dynamical regimes. It is clear in Figure 3.6 that the KE advection terms, in particular, are extremely different depending on the region, and cancel out a lot of their behavior when summed all together. For example, KE3 is actually quite positive, and thus a large source of energy throughout most of ROD, but is cancelled out by the even larger negative magnitudes in WB. In the full domain, this cancellation results in a net negative transfer of KE3 at low-frequencies, and completely masks the fact that it is positive in both the CS and ROD regions, and the primary source of energy in the latter. By using "energy" in this and the previous section, we remind the reader that we are only discussing the contributions to the basin integral. There are other terms in the energy budget that remain prior to domain-integration that we are not considering here.

The grey dashed lines in each plot of Figure 3.6 are the sums of the terms and indicate the overall sign of energy transfer in each region, thus revealing the regions that are overall sources or sinks of energy for the entire system. The CS and ROD regions are primarily sources of energy, whereas WB is a very large sink of energy overall. We can therefore conclude that in the Q-GCM ocean, the primary sink of energy occurs in the western boundary region. This result is consistent with *Zhai et al.* (2010), who also identify the western boundary as an important sink of ocean eddies in both a single-layer idealized model and in observations. The primary sources of energy in the Q-GCM ocean are located both in the CS region, and in the ROD. It is worth remembering that the CS region is a much smaller geographic region than the ROD, and yet they are behaving as energy sources of similar magnitude. This size discrepancy indicates that, per unit area, the CS is a very significant source of variability in the ocean. With all of these regional differences, we therefore emphasize the importance of considering regions of differing dynamics when interpreting spectral transfers so as to not mask the different behaviors in each region. We note that this work follows that of *Arbic et al.* (2012, 2014), who investigated only the full-domain

integrated spectral transfers. However, they utilize a doubly-periodic QG turbulence model that displays only one dynamical regime, and thus did not need to be split into regions.

3.4 Summary and Discussion

We have used the spectral transfer framework of *Arbic et al.* (2012, 2014) in the frequency domain to investigate the energy variability in the Quasi-Geostrophic Coupled Model. Through a combination of area-integrated spectral transfers and spatial maps of frequency-averaged spectral transfer, we have diagnosed the dominant energetic source and sink terms in the ocean and atmosphere in the frequency domain, and have identified dynamically distinct oceanic regions that display strikingly different behavior of energy variability.

Our analysis differs from previous work in several ways:

- We use a model that is both more complex than the idealized, doubly-periodic, dynamically homogeneous models used in *Arbic et al.* (2012, 2014), but simpler than the realistic models used by *Arbic et al.* (2012, 2014), *Sérazin et al.* (2018), and *O'Rourke et al.* (2018), which thus allows us more complicated dynamics, while still explicitly solving for each term in the energy budget.

- We use frequency-domain (and not wavenumber) spectral transfers, as in *Arbic et al.* (2012, 2014), *O'Rourke et al.* (2018), and *Sérazin et al.* (2018), but different from the majority of earlier literature.

- We extend our analysis into lower frequencies, up to 100 years, to compare the differences in variability at high versus low frequencies. With specific interest in climate variability, we considered 100 years to be the minimum length of time to see decadal variability - a particularly important timescale of variability in the ocean. This is in contrast to the 3–20 year ranges used in *Arbic et al.* (2012,

2014) and *O'Rourke et al.* (2018) and the realistic model/altimetry calculations in *Arbic et al.* (2012, 2014), and is more in line with the longer, multidecadal model records used in *Sérazin et al.* (2018).

In this paper, we have made several observations about the behavior of ocean and atmosphere variability:

- Nonlinear advection of KE1 is the dominant source of energy in the ocean at low frequencies (timescales $>$ 3 years).
- Nonlinear advection of KE2 is the dominant source of energy in the atmosphere at nearly all frequencies (timescales $>$ 20 days).
- PE1 and KE1 spectral transfer terms show opposite behavior in the area-averaged atmosphere, but not in the area-averaged ocean. The western boundary current separation (CS) and western boundary (WB) regions, however, do display this classical opposite behavior (*Steinberg et al.*, 1971; *Salmon*, 1980).
- The WB region is a large overall sink of ocean energy at timescales larger than about 50 days, dominated by the KE advection terms (mostly KE3).
- The CS region is an overall source of ocean energy, dominated by the KE advection terms (mostly KE1).
- The 17- and 34-year peaks of KE1 are seen as energy sources in the CS and sinks in the WB, suggesting that there is important variability at these timescales in the western boundary current separation and that they are extracted along the western boundary.
- KE3 is a large sink of energy averaged over the domain, and this appears to stem only from the WB. KE3 is a source of energy in both the CS and ROD.

- The wind stress extracts energy from the ocean overall, as predicted for perturbative wind contributions and using relative winds (*von Storch et al.*, 2007; *Wilson*, 2016; *Renault et al.*, 2016).

- The KE terms display larger-scale spatial structures in the low-frequencies, but smaller-scale spatial structures are found at all frequencies.

In this chapter, we have shown that the ocean sources and sinks in the strongly eddying regions of the CS and the WB are driven primarily by the nonlinear advection of kinetic energy. This result implies that, in our idealized model, aside from explicit time-mean contributions (which are inherently removed in our spectral analysis method), the ocean eddies and jets are the largest driver of energy transfer in and out of the ocean. These ocean motions at low frequencies, corresponding to timescales of 50 days up to 100 years, appear to mostly be sourced in the CS (and ROD for the third layer), and extracted via the WB. Since the CS region is dominated by KE1 and the WB by KE3, our results suggest that ocean eddies generated near the surface of the ocean (and possibly also westward-propagating Rossby waves), hit the western boundary of the domain, where their energy is transported downward, and is ultimately dissipated in the bottom layer along the western boundary. This finding is consistent with *Zhai et al.* (2010) who also found that the western boundary is a hot spot for ocean eddy dissipation, though the exact physical mechanism responsible for removing eddy energy along the western boundary remains an open question. This behavior will be further discussed in the next chapter.

The two low-frequency peaks of KE1 in the CS region are difficult to explain physically based solely on the methods used here. It is interesting, however, that these peaks are not obvious in the ocean KE spectra shown in 3.2b, thus indicating that these spectral transfers identify special behavior of the system beyond what can be seen through examination only of spectra. As mentioned previously, spectral peaks at nearly identical timescales as we have seen in this work (17 and 34 years) were

found by *Hogg et al.* (2006) also in a coupled run of Q-GCM. In their case, these spectral peaks appear broader than those found in our results, and were observed in the spectra of first mode Hilbert empirical orthogonal functions (see *Hogg et al.* 2006 for full details) of ocean interface height and sea-surface temperature. The fact that these peaks have been observed in Q-GCM in both the current study and in *Hogg et al.* (2006) implies that Q-GCM has significant variability at these timescales (17 and 34 years, and more generally at timescales longer than 12 years). We suggest that this may be caused by a low-frequency meander in the western boundary current separation (which mimics the Gulf Stream in this work), and this idea will be discussed further in the following chapter.

The fact that our analysis has highlighted the eddying regions of the model (the WB and CS) as the most interesting and relevant to the energy budget may help extend some results from other studies. *Penduff et al.* (2011) and *Sérazin et al.* (2015) both find that the low-frequency variability in the active eddying regions, namely the western boundary currents, are mostly due to intrinsic dynamics. In the current work, the KE advection terms dominate the eddying regions of the WB and CS at nearly all frequencies, with largest signatures in the low frequencies. These transfers of KE advection can be thought of as the "coupled intrinsic" behavior of the ocean in our setup. We are calling it "coupled intrinsic", because the nonlinear advection of KE is an inherently oceanic process (so "intrinsic" to the ocean), but we are in a coupled regime thus making it difficult to determine what the overall driver is of the oceanic KE advection. In the sense that KE advection is an indicator of intrinsic behavior, our results are consistent with *Penduff et al.* (2011) and *Sérazin et al.* (2015), as well as *Sérazin et al.* (2018) and *Arbic et al.* (2012, 2014) who find that nonlinear KE advection is the largest source of energy at low frequencies in their respective models, regardless of eddy activity. Our results can go a step further to say that the primary role of KE advection in low-frequency oceanic variability,

especially in the eddying regions, still exists in a fully coupled system. That is, the dynamic coupling with the atmosphere does not remove the dominance of KE advection in the maintenance of low-frequency variability in the eddy-active regions of the ocean. In fact, we also observe peaks in most of the atmosphere terms, particularly KE2, PE1, and bottom drag, at the same timescales (though more prominently at 17 years). If the peaks in ocean KE advection are in fact intrinsic, the similarly peaked behavior in the atmosphere could be an indication that the ocean forces the atmosphere at these timescales. This will be further investigated with the comparison of decoupled and partially-coupled Q-GCM runs, in Chapter IV. Furthermore, future work with explicit mixed layer temperature dependence will help us to diagnose how these eddying regions might affect atmospheric variability, which has been a topic of interest (e.g. *Minobe et al.* 2008 and *Small et al.* 2008).

In contrast to *Arbic et al.* (2014), we are unable, as of yet, to draw broader conclusions regarding the question of intrinsic versus forced behavior in a dynamical system meant to represent the ocean or atmosphere. In the *Arbic et al.* (2012, 2014) analysis of an idealized horizontally homogeneous geostrophic turbulence model, the authors make the claim that nonlinear advection of kinetic energy is the dominant source of low-frequency variability in the ocean, as its spectral transfer term is of greater magnitude than the forcing term, i.e. the forcing from the imposed baroclinically unstable mean flow. With a fully coupled model such as the one we use here, it is trickier to pick apart the inherently intrinsic behavior, compared to the forcing from each fluid. However, all of our results here are by definition due to the behavior of a fully coupled model. Some of the behavior may also persist in an ocean-only model, for instance, but we can state with certainty that all of the results shown here can occur with coupled ocean-atmosphere dynamics. In the next chapter, we will examine how the results from this chapter change when subject to different coupling scenarios.

This chapter uses frequency-domain spectral transfers to study the energy budget

of Q-GCM with the goal of identifying intrinsic versus forced versus coupled behavior, based on the dependence of the terms in the energy budget. The results in this chapter are designed to demonstrate that spectral transfers in the frequency-domain are a powerful tool for determining which terms are sources and sinks of energy in the climate system, and at what locations, organized by frequency. We have highlighted specific oceanic regions and timescales in this simplified model that may be of particular importance to understanding the sources of variability in more complex models and in the climate system as a whole, and will be used to inform the results in the following chapter where we vary the coupling configuration.

CHAPTER IV

Spectral Energy Transfers in Partially Coupled and Decoupled Configurations

4.1 Introduction

While the previous chapter approaches the question of forced versus intrinsic behavior in a coupled ocean-atmosphere system using the definition of terms in the energy budget, this chapter applies the same framework but to a partially coupled and an atmosphere-only run of Q-GCM. In this chapter, therefore, we employ the method of varying model coupling as a way of distinguishing between forced and intrinsic dynamics, in addition to the method using the energy budget terms as in the previous chapter. As discussed in Chapter I, there have been numerous previous studies of ocean models with varying levels of atmospheric forcing, and models of the atmosphere with varying levels of oceanic forcing, as well as fully coupled models. The majority of these papers start with the most basic of models (say, an ocean) and start adding different atmospheric forcing to see how the new addition affects the fluid of interest - a "build-up" technique. In this chapter, we use the reverse method. In this "build-down" method, we start with a fully coupled ocean-atmosphere model and start removing specific mechanisms to see how such a removal affects the system as a whole. It is this "build-down" method that we call partial coupling: we run

a fully coupled Q-GCM and cut out a one-way communication channel between the two fluids. In this way, we can attribute specific behavior to its driving mechanism. We then compare partial coupling to an atmosphere-only setup, where there are no ocean dynamics. In this chapter we use this method of varying the ocean-atmosphere coupling and comparing the outcome to the fully coupled results from the previous chapter in order to distinguish between forced and intrinsic variability, combined with the previous chapter's method based on term dependencies.

A previous study by *Hogg et al.* (2006) examines the effects of partial coupling in a nearly identical setup of Q-GCM as used here. They employ empirical orthogonal functions and canonical correlation analysis, instead of spectral transfers, to study low-frequency variability in the system. They find a mode of (primarily interdecadal) ocean variability that is intrinsically driven and affects the SST field, which in turn modifies the atmospheric variability. *Hogg et al.* (2006) claim, is that the intrinsic ocean dynamics do not create new modes of variability, but rather project onto existing atmospherically-driven modes, by altering the associated time scales. They thus find that intrinsic ocean dynamics affect atmospheric variability, particularly in the time domain.

More recently, *Larson et al.* (2018) also employ partial coupling to quantify the contribution that momentum coupling plays in climate models, and specifically how it affects the ocean. The authors use the realistic, global Community Earth System Model (CESM) created by the National Center for Atmospheric Research (NCAR). They compare a fully coupled run with a "mechanically decoupled" run, i.e. a run where only a climatological (as opposed to a time-varying) wind stress drives the ocean. However, all other buoyancy and thermal fluxes remain intact. They find that in the mechanically decoupled run, SST variance is reduced in midlatitudes (though the opposite is true in the subtropics). Their focus is thus on how mechanical coupling from the atmosphere to the ocean affects the SST field, which is not a main goal of

this chapter.

Here, we use partial coupling and a de-coupled atmosphere-only setup to investigate how the ocean influences the atmosphere. As previously discussed in Chapter I, our primary motivation stems from theoretical and observational work by *Bjerknes* (1964) and *Gulev et al.* (2013) that the ocean only affects low-frequency behavior in the atmosphere. Neither of these earlier studies, however, were able to explicitly resolve ocean eddies. With our turbulent eddy-resolving model, we are interested in determining how the ocean-atmosphere feedback might be modified with the inclusion of small-scale motions in the ocean.

In this chapter, we vary the coupling to examine how the ocean dynamics may drive atmospheric variability across timescales (from 2 days to 100 years). We apply the spectral transfer diagnostic to a partially coupled run of Q-GCM, as well as an atmosphere-only run, and compare the results with those of the fully coupled configuration from Chapter 3. The details of the partially coupled and atmosphere-only runs are outlined in Section 4.2, and results are outlined and discussed in Sections 4.3 and 4.4, respectively.

4.2 Modified Coupling in Q-GCM

Built in to Version 1.5 of Q-GCM is the possibility of partial coupling between the ocean and atmosphere. In the fully coupled version of the model, there are vertical exchanges of energy at each layer interface, in the form of pressure gradients between QG layers, and in the form of Ekman pumping, temperature advection, and heat fluxes in the mixed layers and atmospheric QG layers.

The partially coupled setup that we use removes the influence from the QG ocean dynamics in the advection of ocean sea surface temperature (SST). In other words, the mixed layer velocities that are, when in a fully coupled state, defined by contributions from both QG ocean pressure gradients and Ekman pumping, as given in equation

(2.9), are now only functions of the Ekman pumping. We can thus rewrite equation (2.9) with the introduction of coupling parameter Y_C as:

$$({}^{o}u_m, {}^{o}v_m) = \frac{Y_C}{f_0}\left(-{}^{o}p_{1y}, {}^{o}p_{1x}\right) + \frac{1}{f_0 {}^{o}H_m}\left({}^{o}\tau_y, -{}^{o}\tau_x\right), \tag{4.1}$$

where u_m and v_m are the mixed layer velocities in the zonal and meridional directions, respectively, and the rest of the terms are as defined in Chapter II.

This configuration (hereafter "YPC" for "Y_C Partial Coupling") thus removes the effect of QG ocean dynamics from the rest of the system, though the ocean dynamics are still fed the information from the mixed layers and QG atmosphere as in the fully coupled (henceforth "FC") setup. This scenario damps the effects from internal ocean dynamics, but leaves in any contributions from intrinsic atmospheric and limited coupled behavior, similar to a swamp ocean model (*Hogg et al.*, 2006), which allows for a dynamic SST field to couple with the atmosphere, but with no momentum contributions. Figure 4.1 shows a diagram of how YPC (and the atmosphere-only setup described below) is different from FC. We note that there is still coupling due to the relative stress terms which do not change in the YPC run. In YPC, we are more interested in how the atmosphere responds to the partial coupling, rather than the ocean, because the ocean forcing remains exactly the same. In fact, we will interpret any changes in the ocean as adjustments either to the atmosphere's response to the removal of ocean dynamics from the coupling or to the direct influence of an altered SST field on the QG ocean dynamics. Therefore, any ocean adjustments may not be as physically relevant, but are still very useful to inform us about the way in which the coupled system as a whole responds to perturbations in the coupling.

The other model configuration that we use is what the model user guide refers to as atmosphere-only (hereafter "ATO"). This configuration is not partially coupled, because there are no ocean dynamics. In ATO, the ocean portion of the model does not run at all, and is instead represented by a climatological SST field (averaged

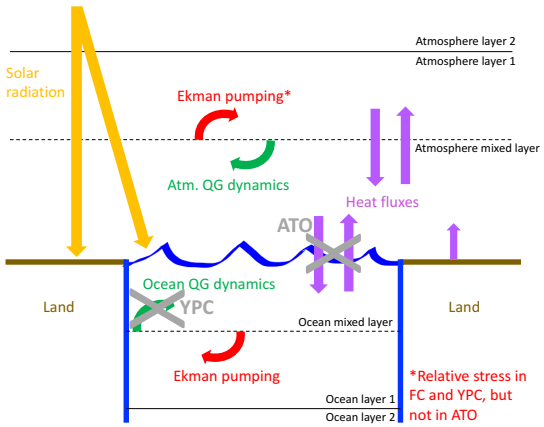

Figure 4.1: Diagram of Q-GCM coupling mechanisms illustrating the differences between fully coupled (FC), Y_C partial coupling (YPC), and atmosphere-only (ATO) model configurations.

over 100 years from the fully coupled run). The atmospheric mixed layer still has an evolving temperature and height field, and heat fluxes are still exchanged between the atmospheric mixed layer and the QG layers. ATO then effectively removes the time-varying mechanical and diabatic coupling contributions from the ocean to the atmosphere (see the diagram in Figure 4.1). This setup does not use relative wind stress, since there are no ocean velocities calculated. We consider these two configurations, YPC and ATO, to work well together as they build upon each other. The YPC setup removes the effect of ocean dynamics in the SST field, leaving only the time-varying Ekman-driven field. The ATO takes this a step further and removes all time-varying portions of SST, replacing them with an averaged field. To help illustrate the differences in these configurations, we display snapshots and averages of the SST field in the three different model setups in Figure 4.2.

The difference between FC and YPC are apparent in the snapshots of SST shown in Figure 4.2. The small-scale eddies in the FC setup are not present in YPC (or the averaged ATO field), but the overall double-gyre pattern is intact in all of the configurations. A unique feature of the YPC setup appears to be a different path of

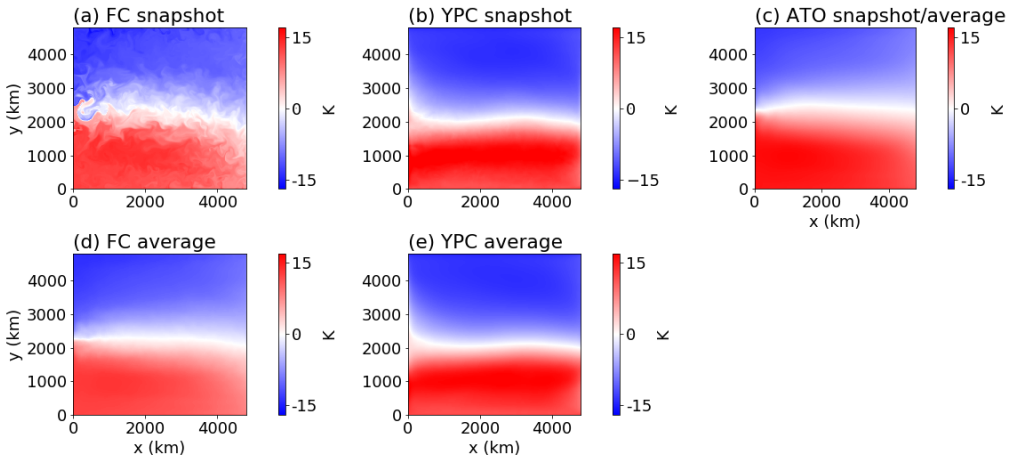

Figure 4.2: Snapshots and averages of SST anomaly in the different model configurations.

the boundary between the two gyres. The separation point from the western boundary appears to be further north than in FC, which may be consistent with *Smith et al.* (2000) who find that the presence of explicitly-resolved eddies in an ocean model play a key role in determining the correct position of the Gulf Stream separation point. Another difference we see between YPC and FC (and thus also ATO as an FC average) is that the eastward protrusion dips further south across the basin than in FC, yielding a smaller subtropical gyre. These differences may play crucial roles in altering the ocean-atmosphere variability in Q-GCM.

4.3 Results

In this section, we use the spectral energy transfer method as in Chapter 3. Because a primary goal of this work is to investigate how the ocean dynamics affect the atmosphere, we focus mainly on comparing the YPC with the FC configuration. We identify a couple key differences that we then compare to the ATO run in order to observe how the behavior changes under more coupling simplifications. As in the previous chapter, we look at kinetic energy spectra, domain-integrated spectral energy

transfers, regionally-integrated ocean spectral transfers, and we also compare ratios of many terms in the different configurations with their coupled counterparts.

4.3.1 Significance Measures

We compare kinetic energy spectra and transfers in the different model configurations: FC, YPC, and ATO. In order to robustly compare each of the terms in these runs, we include a statistical confidence envelope on each term plotted. This confidence envelope is calculated using the standard error of the seven 100-year model runs in each configuration. We calculate the standard deviation σ across the seven runs and define the error as:

$$\frac{\sigma}{\sqrt{N}}, \tag{4.2}$$

where N is the number of degrees of freedom—in this case, 7. The minimum and maximum of the confidence envelope of term x are then defined as:

$$\overline{x} \pm \frac{\sigma}{\sqrt{N}}, \tag{4.3}$$

where $\overline{x}$ is the average of term x across all seven 100-year runs.

This method does not take into account the inherent difference between various frequencies in a Fourier analysis. For instance, the number of 20-day samples over 100 years is far greater than the number of, say, 34-year samples. This discrepancy means that we expect the lower frequencies to be less statistically robust than the higher frequencies. To make use of the fact that the density of frequencies at each timescale increases toward shorter timescales, we apply a frequency averaging scheme that averages over more frequencies, the higher the frequency. The number of points averaged over is given in Table 4.1. These values were chosen by visual inspection, in order to best preserve important features of each term, while reducing the noisy

Table 4.1: Frequency averages in spectral plots

Number of frequency points averaged over	Number of points over which the average is applied	Associated timescales
1 (i.e. no averaging)	22	4.5 - 100 years
3	37	1.7 - 4.5 years
9	91	244 days - 1.7 years
15	91	152 - 244 days
21	7,059	5 - 152 days
51	10,950	2 - 5 days

behavior as much as possible.

4.3.2 Y_C Partial Coupling (YPC)

4.3.2.1 YPC Kinetic Energy Spectra

In the YPC setup, the information from the ocean dynamics does not get translated from the ocean and into the SST field. Thus, the atmosphere's behavior in this scenario is not directly influenced by the ocean dynamics (except via the relative stress term), but the rest of the coupling mechanisms are still intact.

The atmospheric kinetic energy (KE) spectra are shown in Figure 4.3a for each configuration: FC (blue), YPC (green), and ATO (orange). Overall, the spectra do not appear to change greatly across the different model setups, with the shapes of each layer remaining intact, with small variations at specific frequencies. For now, we concentrate on the YPC results in this section, and will address the ATO results later in Section 4.3.3. The most prominent difference between YPC and FC in all of the atmospheric layers is the oppositely oriented peak at 17 years. In each layer, the FC line shows an upward peak at 17 years, while the YPC line shows a downward peak. This not only means that there is less energy in the YPC compared to the FC configuration, but also suggests that, in the FC case, there is a noticeable increase in energy at 17 years, while in the YPC case there is a noticeable decrease in energy

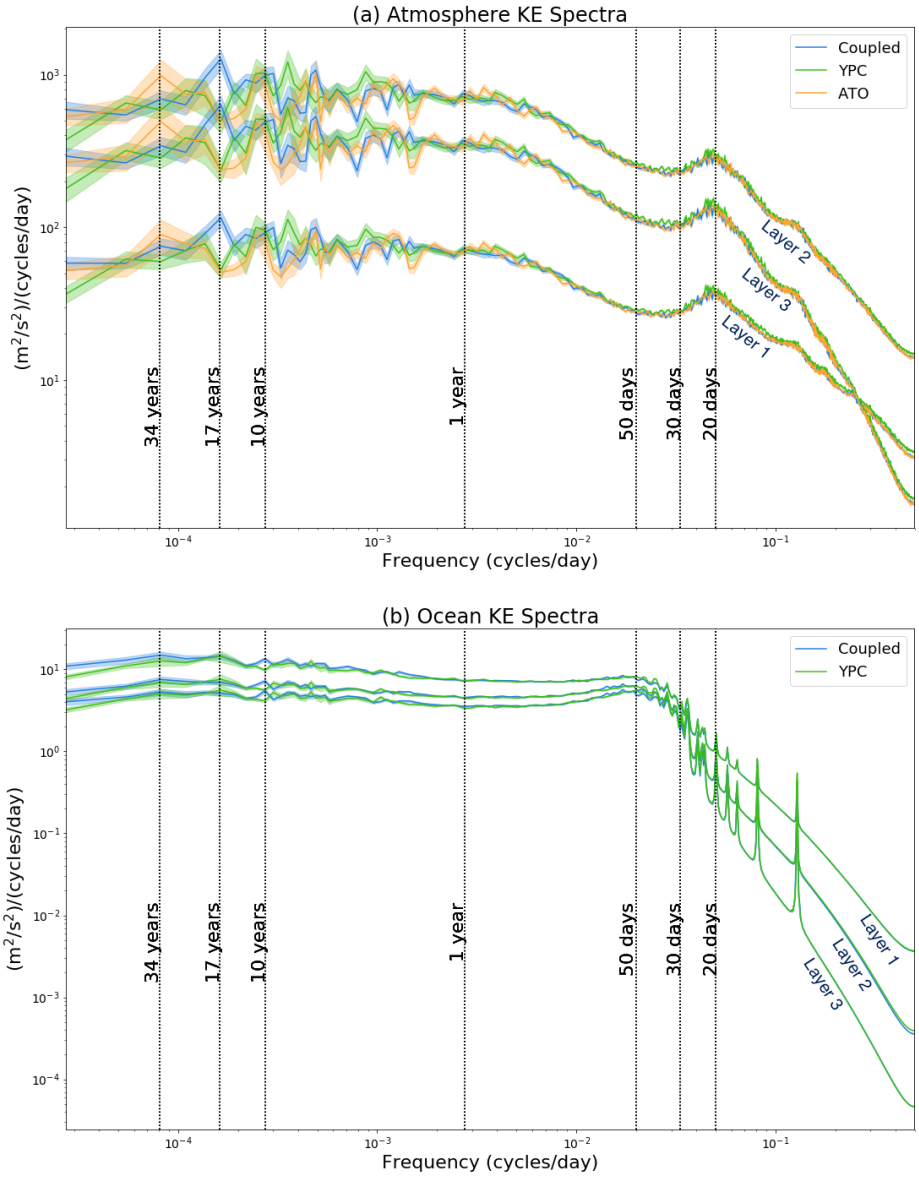

Figure 4.3: Domain-integrated kinetic energy spectra in each of the three layers in the (a) atmosphere and the (b) ocean. The colors indicate the different model configurations: FC (blue), YPC (green), and ATO (orange). The solid lines are the average over 7 100-year time periods, and the confidence envelopes designate the standard error across all 7 time periods.

at the same timescale. The relatively narrow confidence envelope at the 17-year timescale indicates that this behavior is likely statistically relevant and likely due to physical mechanisms in each model run. This difference at 17 years implies that there is an injection of energy at 17 years in the FC case that is not present when ocean dynamics are removed from SST advection, thus indicating that there is internally sourced ocean variability at 17 years. This is consistent with an intrinsically sourced ocean mode of variability at 17 years that we found in the previous chapter, and that was also found by *Hogg et al.* (2006).

At high frequencies, there appears to be a subtle but consistent difference between YPC and FC across all atmospheric layers. Note that the FC and ATO spectra almost completely overlap at high frequencies, so the blue FC line is hidden behind the orange ATO line. The YPC result appears to be marginally greater than the FC result at the highest frequencies. To help visualize these differences, we plot the ratios of the YPC (as well as the ATO) to FC spectra in Figure 4.4. We've plotted the ratios of each YPC layer to the corresponding FC layer (green), as well the ratios between ATO and FC (orange), which we will return to later on. There are black dotted lines on the 1:1 lines, and we have included dotted grey lines indicating a 5% increase (a ratio of 1.05) in order to show the scale of the high-frequency differences. Indeed, it appears as though the YPC run has about 5% more energy in each of the three atmospheric layers at time scales of 2 to roughly 20 days. This result suggests that the ocean dynamics in the FC setup cause a slight decrease in the amount of energy present at high frequencies in the atmosphere. While this high-frequency behavior may be associated with the lack of ocean eddies in the YPC SST field, we will find later that the stress term may be the responsible term.

In addition to helping visualize the high-frequency behavior, the ratios in Figure 4.4 also emphasize the similarity in shape and magnitude across the spectra in different model runs. In both fluids, and especially the ocean, the ratios hover close to the

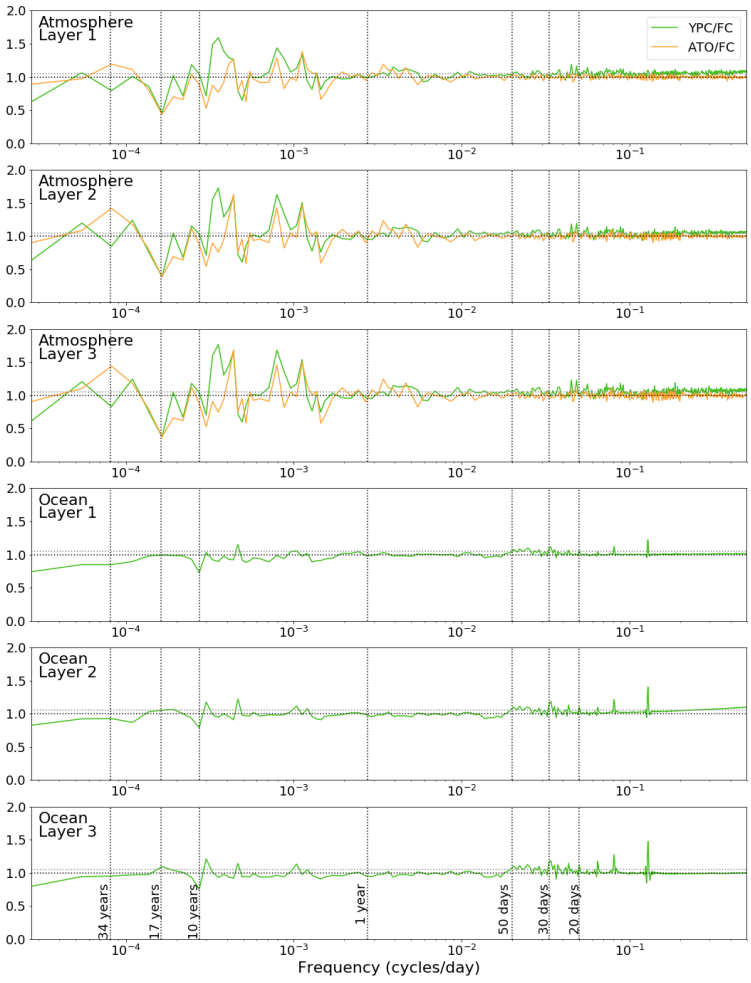

Figure 4.4: Ratios of kinetic energy spectra for YPC and ATO compared to FC, in all three layers of the ocean and the atmosphere. The black dotted line shows a ratio of 1, and the grey dotted line indicates a ratio of 1.05—a 5% difference.

1:1 line. Furthermore, the ratios highlight the fact that each of the layers (in both fluids) responds very similarly to the different model configurations. Such similarities suggest that the amount of energy in the system may adjust barotropically to the YPC (and ATO) setup.

There are several other differences between FC and YPC atmospheric spectra, including a segment between about 2 and 4 years when YPC is larger, and does not display the two downward peaks at 2.4 and 3.5 years present in FC (hence the two large upward peaks in the ratios). Near 6-8 years there is also a peak of energy in YPC that appears to be the largest difference in the ratios, but we note that the width of the confidence intervals in Figure 4.3 are much larger at these timescales.

The oceanic KE spectra in Figure 4.3b show that there is even less of a difference between the YPC and FC model scenarios than we observed in the atmosphere. There are almost no noticeable differences in any of the three layers, the clear exception being the opposing peaks at a timescale of 10 years. Across all layers, the FC line peaks upward while the YPC line peaks downward, which mimics the behavior seen at 17 years in the atmospheric spectra. It is unclear at this time what the source of these two different peaks might be, but it is possible that their similar characteristics could indicate a connection of some sort. We will discuss the 17-year behavior more with regards to atmospheric spectral transfers in Section 4.3.2.2, but we find that the 10-year peak does not play as large a role in the transfer of energy.

At high frequencies (more visible in the ratios shown in Figure 4.4) we see that the first and third layer oceanic spectra appear to show no changes, but the YPC is slightly larger at high frequencies in the second layer spectrum. This is curious, as the rest of the spectra appear to be nearly identical across model setups. It is an indication that the KE2 term may play a larger role than initially thought, and may indicate that there is baroclinic behavior at the high frequencies. It is surprising that we see this difference in the second, and not the first layer, given the direct

impact from the modified coupling. Still, it appears as though the atmosphere is more consistently affected by the increase in high-frequency behavior at short timescales, indicating that the QG ocean dynamics appear to (slightly) decrease the amount of energy harbored in the atmosphere at high frequencies (from roughly 2 to 100 days). There are a couple of other smaller differences in the ocean KE spectra, such as the fact that the coupled run appears more energetic at the lowest frequencies (at 100 years). Because there are so few samples at these extreme low frequencies, we will not spend time discussing these potential differences.

4.3.2.2 YPC Domain-Integrated Spectral Energy Transfers

Figure 4.5 shows the domain-integrated atmospheric and oceanic spectral transfer plots for the YPC configuration. Compared to Figure 3.3 in the previous chapter, there are only very slight differences in each fluid. For instance, the 17-year atmospheric peak in the FC run is noticeably absent in the YPC run. Beginning with the atmospheric transfers, we directly compare the individual terms between FC and YPC, by showing each term for all configurations on its own set of axes (see Figure 4.6). Before we continue, we remind the reader that we consider the nonlinear advection terms (as well as the ocean bottom drag) to be a measure of intrinsic variability in each fluid, and we thus consider any changes in the transfers of (specifically KE) advection in the non-fully coupled runs as an indication of a change in that fluid's dynamics. For instance, we interpret a change to the atmospheric KE transfers as a change to the atmospheric dynamics (and the same in the ocean). On the other hand, the buoyancy and stress terms contain variables from both fluids, and are thus deemed "forcing" terms. As such, any modifications to these terms in YPC compared to FC are not considered indications of intrinsic dynamics. In fact, we expect the buoyancy and stress terms to show the greatest differences between the runs, since these are the terms most directly impacted by the variations in coupling. We start the

discussion with the spectral transfer of atmospheric buoyancy, because it is this term that directly translates information from the mixed layer heat fluxes and temperature field to the QG atmospheric layers. Thus, in the YPC model run it is the buoyancy term that directly sees the altered SST state (via the AST).

A comparison between atmospheric spectral energy transfers in the FC (blue) and the YPC (green) runs is shown in Figure 4.6. Again, the orange ATO line is also shown and will be discussed later. We have included a small inset in each of the subplots to better discern the high-frequency differences. These insets display timescales shorter than 30 days for the spectral transfer terms multiplied by the frequency vector (i.e. in variance-preserving form), and effectively highlight the high-frequency behavior. As was the case for the atmospheric spectra, we again see that the high-frequency behavior of FC is almost completely hidden by the ATO result.

Overall, the spectral transfers look very similar across model setups, except for the buoyancy term. The spectral transfer of buoyancy in the FC and YPC model configurations appear to be similarly shaped at high frequencies, but differ drastically at low frequencies. From about 8 to 100 years the YPC buoyancy is a significant source of energy, while the coupled term is a sink of energy. There are other differences, including a broad negative YPC peak centered around 3 years, and more narrow peaks at 5 and 6 years, as well as at 250 and 300 days. In fact, at most timescales the YPC buoyancy has a larger magnitude than its FC counterpart, sometimes much larger and sometimes only marginally larger. Although the high-frequency behavior is difficult to see, even in the variance-preserving inset, there is a noticeable increase in energy transfer in the YPC run at the highest frequencies, corresponding to timescales between 2 and 5 days. This behavior is more apparent in Figure 4.7(a), which shows the ratios of domain-integrated atmospheric spectral transfer terms in the YPC compared to the FC setup. This ratio plot actually indicates that all of the transfer terms display greater high-frequency YPC magnitude by up to 10%, with the bottom drag

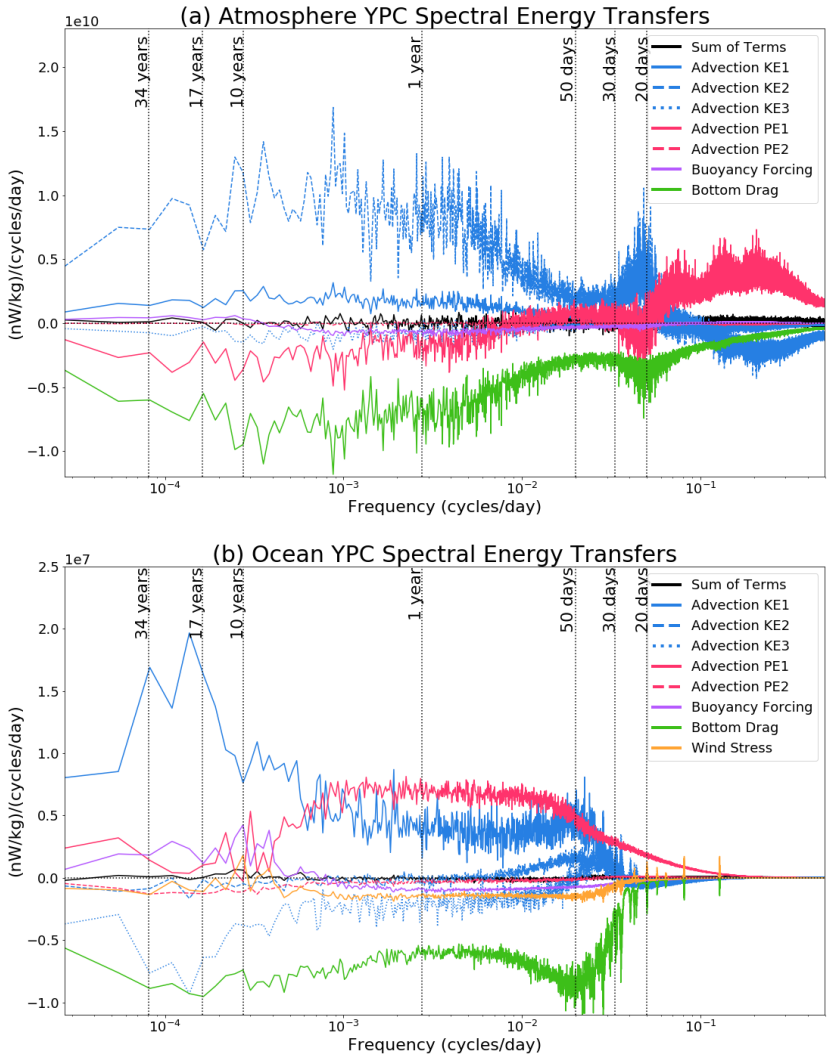

Figure 4.5: YPC domain-integrated spectral energy transfers in the atmosphere (a) and the ocean (b).

term showing the most persistent YPC increase through nearly 100 days. Note that we only display the five terms that we consider the most dominant in the spectral energy budget in Figures 4.6 and 4.7, and have thus chosen not to further discuss the atmospheric KE3 and PE2 terms. Likewise in the ocean, the rest of the figures plot the six most interesting/dominant terms, neglecting the KE2 and PE2 transfers.

With the atmospheric spectral transfers showing up to a 10% increase in magnitude for YPC versus FC, we now examine the ocean spectral transfers with specific interest in any high-frequency differences. The comparison of the individual spectral transfer terms is shown in Figure 4.8 for FC (blue) and YPC (green). Generally, there are very few differences across the two model setups, especially in the KE terms. Since we are currently interested in high-frequency behavior, we turn our attention to the ratios of the ocean transfers for YPC compared to FC in Figure 4.9a, which reveal the high-frequency differences in the domain-integrated ocean transfers. Due to the noisy low-frequency ratios, we have plotted the ocean ratios through 2 years only.

The domain-integrated spectral transfer of ocean buoyancy adjusts very noticeably to the YPC run at high frequencies in Figure 4.9a, showing an over 15% increase in energy transfer from the FC run at all timescales shorter than 30 days. Interestingly, the other ocean transfers show only a marginally greater YPC magnitude at the high frequencies, with the bottom drag displaying essentially no adjustment. As in the atmosphere, it is the ocean buoyancy term that is directly impacted by the SST field. Therefore, this ocean behavior at short timescales suggests that the non-eddying SST field increases the energy transfer at high frequencies in the buoyancy term, but that this information is only minimally translated to the other transfer terms. In the atmosphere, on the other hand, all of the terms show an adjustment at high frequencies. We therefore suggest that SST advection affects the very high frequencies in both the ocean and atmosphere, but the atmospheric terms are more susceptible to changes in the high frequency behavior than the ocean terms. Thus, the impact

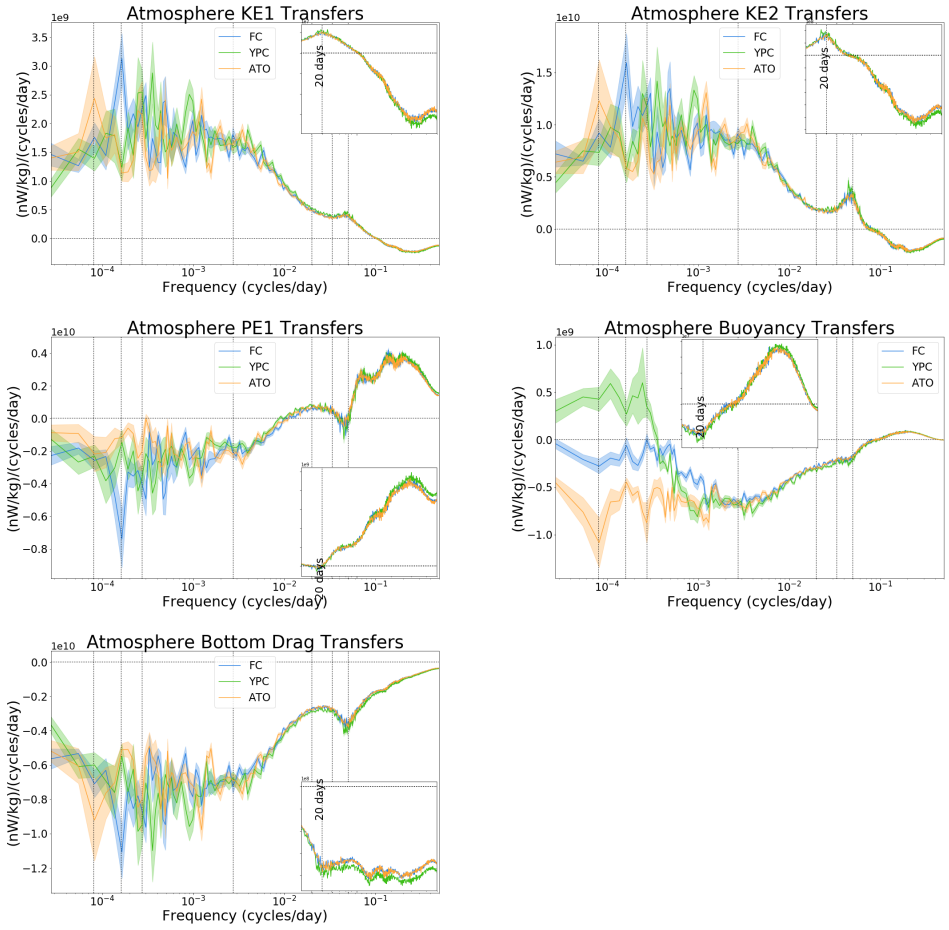

Figure 4.6: Atmosphere spectral energy transfers: comparison between FC (blue), YPC (green), and ATO (orange). The insets show the high-frequency (shorter than 30 days) behavior in variance preserving form—where the spectral transfers are multiplied by frequency—in order to highlight the high-frequency behavior.

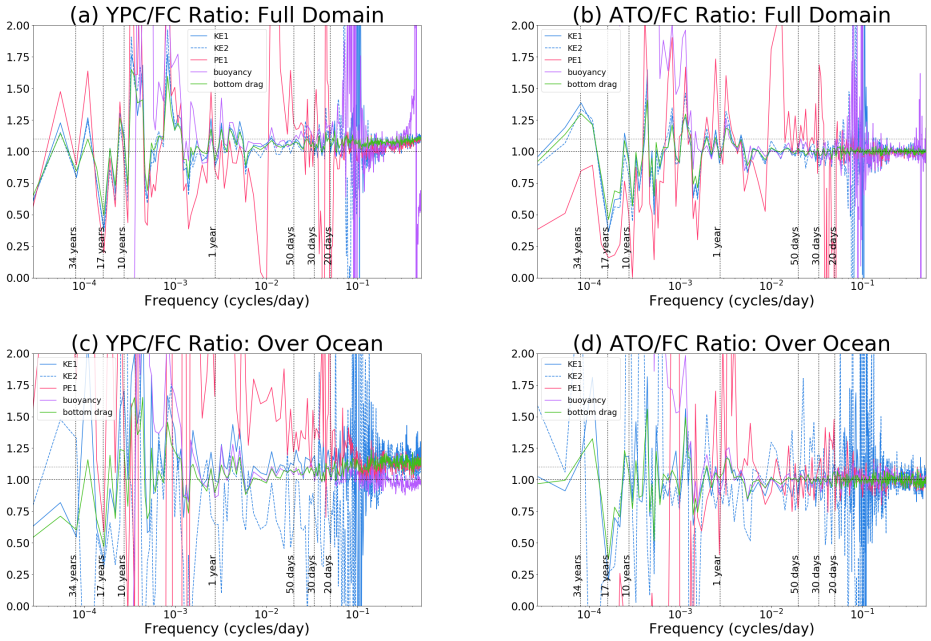

Figure 4.7: Ratios of select atmospheric spectral transfers: YPC versus FC (column 1) and ATO versus FC (column 2). The first row shows ratios of the domain-integrated transfers, while the second row shows ratios of the transfers integrated over the portion of the atmosphere that is directly over the ocean.

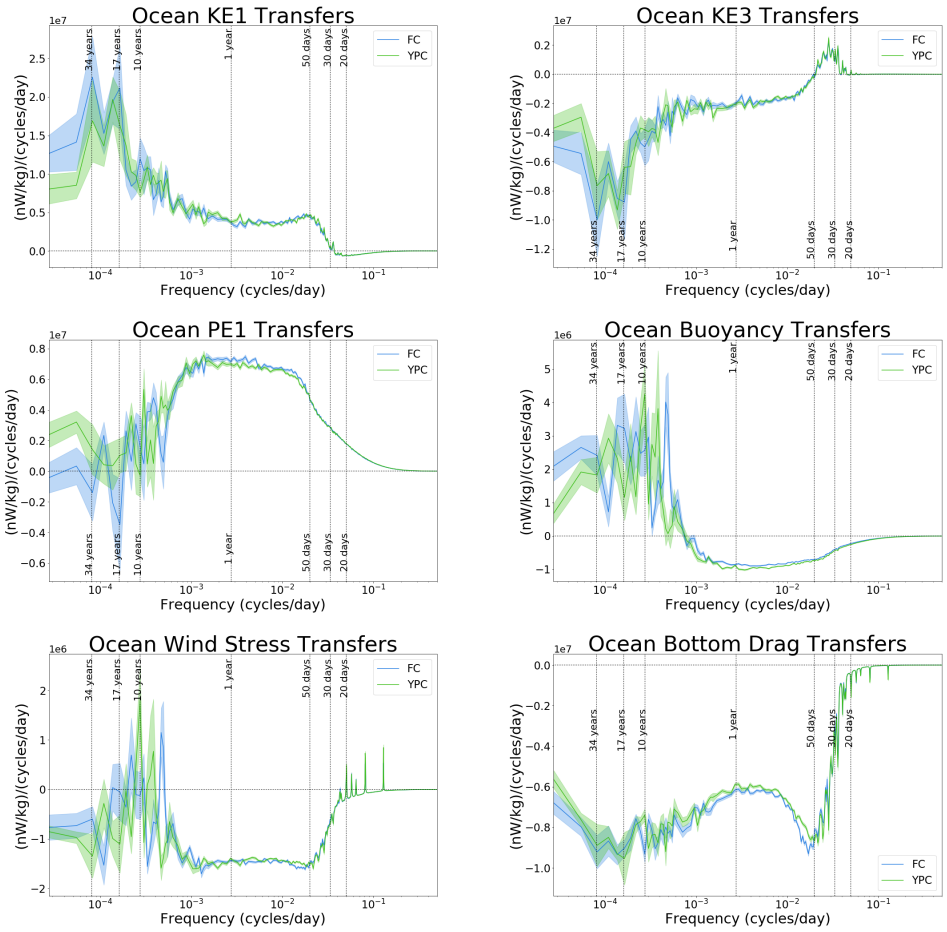

Figure 4.8: Ocean spectral energy transfers: comparison between FC (blue) and YPC (green).

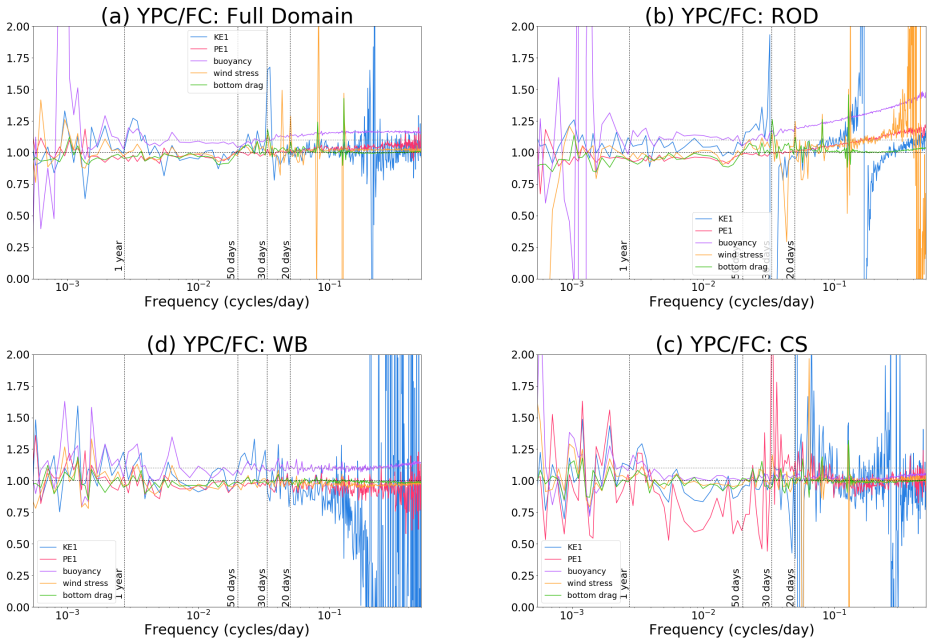

Figure 4.9: Ratios of select ocean spectral transfers: YPC versus FC in the full domain (a), ROD (b), WB (c), and CS (d). Note that the longest timescale in these plots is at 2 years.

of the high-frequency SST in the ocean manifests mostly in the buoyancy term in the domain-wide spectral transfers, whereas every term in the atmosphere shows an increase in energy transfer at the highest frequencies in YPC. We will revisit this high-frequency behavior shortly when we consider regional transfers.

Returning to the atmospheric transfer of buoyancy, another feature that permeates through to all other atmospheric terms is the broad negative peak of YPC centered at 3 years, that spans from about 2 to 4 years. During this time range, YPC buoyancy is between 1.5 and 2 times the magnitude of FC buoyancy. We recall that this 2-4 year time range also showed differences (though smaller) in the KE spectra in the atmosphere. All of the other terms in the atmosphere show a greater YPC versus FC magnitude at these same timescales as well, though none are as obvious as in the

buoyancy term. In each of these cases, the absence of ocean dynamics advecting SST appears to increase the amount of energy transfer at these frequencies, but does not change the shape of the transfer. In fact, all terms except buoyancy have a peak near 3 years in both YPC and FC, but the YPC peak is of greater magnitude. It thus appears that ocean dynamics in the fully coupled model damp the transfer of energy between 2 and 4 years throughout the entire atmospheric energy budget.

In the ocean transfers, we do not see a clear signature at the 2- to 4-year timescale. The ocean buoyancy term displays a greater YPC magnitude from 2 to about 3 years but also, and more notably, at all timescales shorter than 2 years. The wind stress also has marginally greater magnitude in YPC compared to FC between 2 and 3 years. Since these two terms are the ones directly influenced by the atmosphere, this may be an indication that the ocean responds weakly to the atmosphere near 3 years, but this information does not get translated to the other oceanic terms, since there appears to be no behavior of note in that time range in the PE and KE terms. The ocean bottom drag term actually seems to show that the FC term is greater than that of YPC between 2.5 and 4.5 years. But as in the buoyancy term, FC has greater magnitude than YPC throughout many of the mid-frequencies, from 50 days to 2 years, which makes the 2.5 to 4.5 year difference stand out less.

We now turn our attention to the low frequencies, where the atmospheric buoyancy transfer term differs greatly between YPC and FC, as shown in Figure 4.6. Starting at a timescale of 8 years and extending through to 100 years, the YPC term is positive and greater magnitude than the negative FC term. This difference implies that the presence of ocean dynamics affects atmospheric buoyancy significantly at low frequencies, converting it to a sink instead of a source of energy. However, the spectral transfer of atmospheric buoyancy is an order of magnitude less than the dominant terms at low-frequency, and how the large low-frequency differences affect the rest of the atmospheric terms is not clear.

The primary differing feature in the atmospheric transfers at low frequencies between the YPC and FC configurations is at 17 years, as observed in the spectra. In every atmospheric term (excepting buoyancy) we see opposing peaks at 17 years, with FC always having larger magnitude than YPC. It isn't obvious whether or not this peak arises from the buoyancy term. In the ocean transfer plots, there are large 17-year peaks in the KE terms, but these peaks do not appear to change from the FC to the YPC runs, indicating that these peaks are robust to the changes observed in the YPC run. These observations suggest that there may be a 17-year mode of variability in the ocean that is intrinsically driven. This result would agree with our supposition in the previous chapter that the low-frequency 17-year peak is internally sourced by nonlinear advection in the ocean. Furthermore, we find that this mode appears to be translated (in a fully coupled run) to the atmosphere from ocean dynamics via SST advection. We note that the spectral transfers of ocean buoyancy and PE1 do display small differences at 17 years that may just barely be statistically significant, but this information is not communicated to the ocean KE terms (at the 17-year timescale, at least).

We infer that this 17-year intrinsic ocean timescale that we have found is the same as an intrinsic ocean mode found in a similar configuration of Q-GCM by *Hogg et al.* (2006). In their paper, they identify the mode using EOF analysis and also find that it is intrinsically driven by the ocean. (They state that this mode has a spectral peak at about 15 years, but looking at their plots, it does appear as though the peak is actually closer to 17 years.) *Hogg et al.* (2006) find that this interdecadal ocean mode is concentrated over the western boundary current separation region, suggesting that this mode may be caused by, e.g., a meander of the Gulf Stream-like current in the model. This agrees with our result from the previous chapter that the 17-year (as well as the 34-year) peak is seen only in the CS region (and oppositely in the WB), and not in the ROD. *Hogg et al.* (2006) further find that this ocean mode

affects SST variability across the entire ocean basin, indicating that the mode may have widespread effects on the atmosphere beyond the current separation region. Our results are consistent with all of their findings.

Hogg et al. (2006) also postulate that there exists a weakly coupled mode at a decadal timescale in their analysis. Interestingly, in the present analysis there appears to be a clearer 10-year signature in the kinetic energy spectra compared to the spectral transfers. However, close examination of the ocean spectral transfers shows that the KE1, wind stress, and bottom drag terms all do show very narrow opposite peaks right at 10 years, with FC displaying greater energy transfer than YPC. Especially in KE1, the standard deviation is quite large near 10 years, indicating that this is a weak signal, if one at all in that term. The bottom drag shows the strongest decadal peak. None of the terms in the atmosphere show any significant difference at a 10-year timescale. This suggests that whatever energetic mode that exists in the ocean at 10 years may indeed depend on the communication of ocean dynamics to the SST field.

For the remainder of this chapter, we will concentrate on two different timescales that have thus far been shown to make a difference in the atmospheric dynamics: (1) the 17-year peaks and (2) the high-frequency adjustments. In the following section, we examine how the ocean's regionally-integrated transfers might add to the story at these two timescales of interest.

4.3.2.3 Regionally Integrated Spectral Transfers

As demonstrated in Chapter 3, the domain-integrated spectral transfers of inhomogeneous basins like the ocean portion of Q-GCM can mask behavior in different dynamical regions of the domain. We did not see noticeable differences in the spatial maps or in the boundaries of the different dynamical regions. Hence, we turn our attention to the regionally integrated spectral transfers as defined in the previous

chapter. We consider two regions characterized by their intense eddies: the western boundary current separation (CS) and along the western boundary (WB), and a third region that is simply the remainder of the domain (ROD) not included in the CS and WB regions. Our main objective in this section is to examine whether the regionally-integrated spectral transfers show different modifications under the YPC compared to the FC run, particularly at the two timescales of interest: 17 years and near daily.

Comparing the transfers in Figure 4.10, showing all YPC terms in each oceanic region, to those in the FC run in Figure 3.5 of Chapter III, there are very few differences visible. Overall we find, as we concluded from the domain-integrated transfers, that the main features in each region remain largely unchanged between YPC and FC. That is, the KE terms still dominate the CS and WB regions, and the overall signs in each region don't change. By directly comparing the terms, though, we can spot some interesting distinctions between the YPC and FC configurations in the ocean regions that are not apparent in the full domain, and that can help us understand the changes we observe in the atmosphere.

Figures 4.11, 4.12, and 4.13 directly compare the individual transfer terms in both FC (blue) and YPC (green) for the CS, WB, and ROD regions, respectively. In order to study the high-frequency behavior, however, it is easier to look back at the ratios between the ocean transfers, which are shown for the three ocean regions in Figure 4.9b, c, and d. In the full-domain ocean, we observed that buoyancy was the primary term that adjusted to the YPC scenario at high frequencies. Examining the other ocean regions, we notice this is mostly true for the WB region as well, with buoyancy around 10% greater in YPC than FC through roughly 50 days. The other WB terms are, however, very close to the 1:1 line (though we note that the KE1 term has many zero crossings that makes the ratio very noisy and difficult to interpret). In CS, none of the terms show much of a difference at high frequencies.

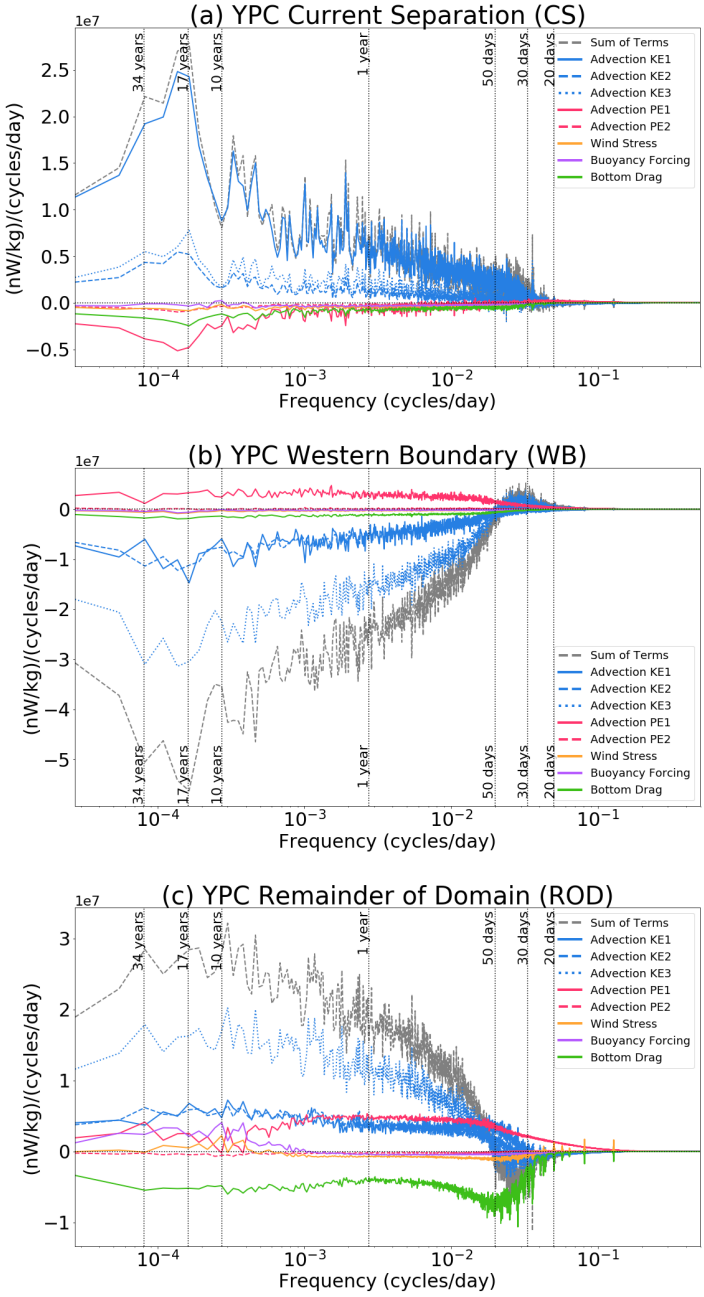

Figure 4.10: Regionally-integrated YPC ocean spectral energy transfers in the CS (a), the WB (b), and the ROD (c).

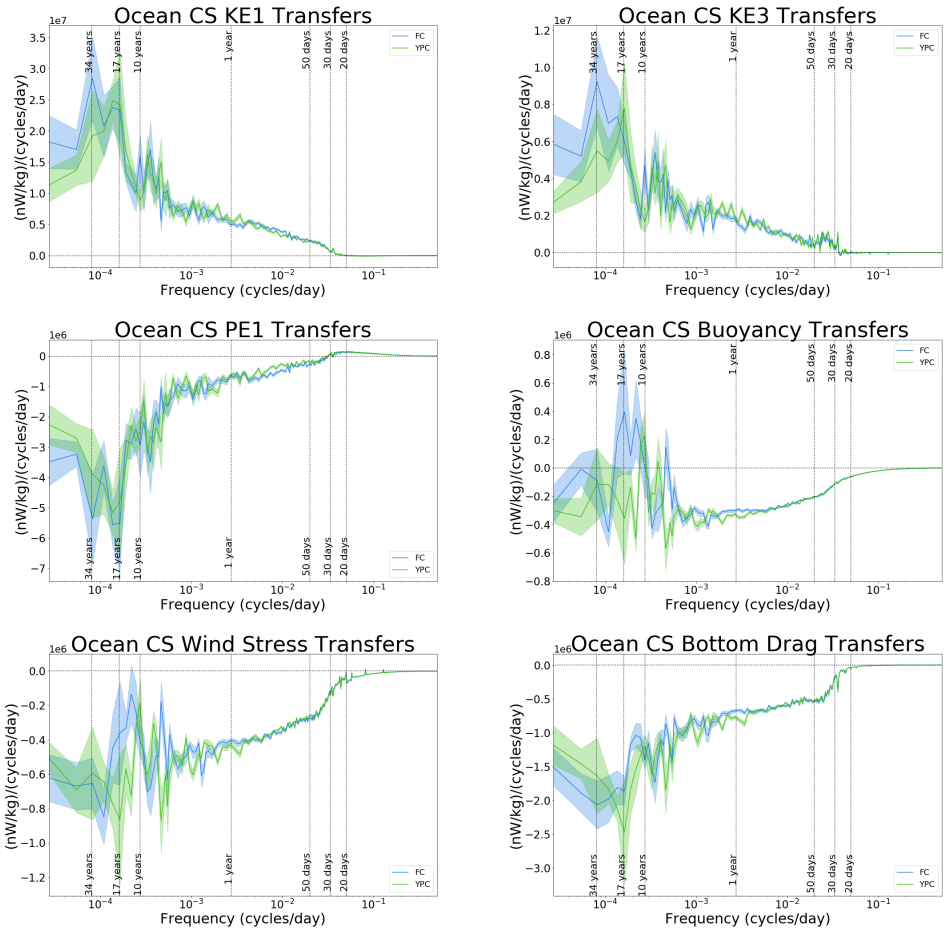

Figure 4.11: Ocean CS spectral energy transfers: comparison between FC (blue) and YPC (green).

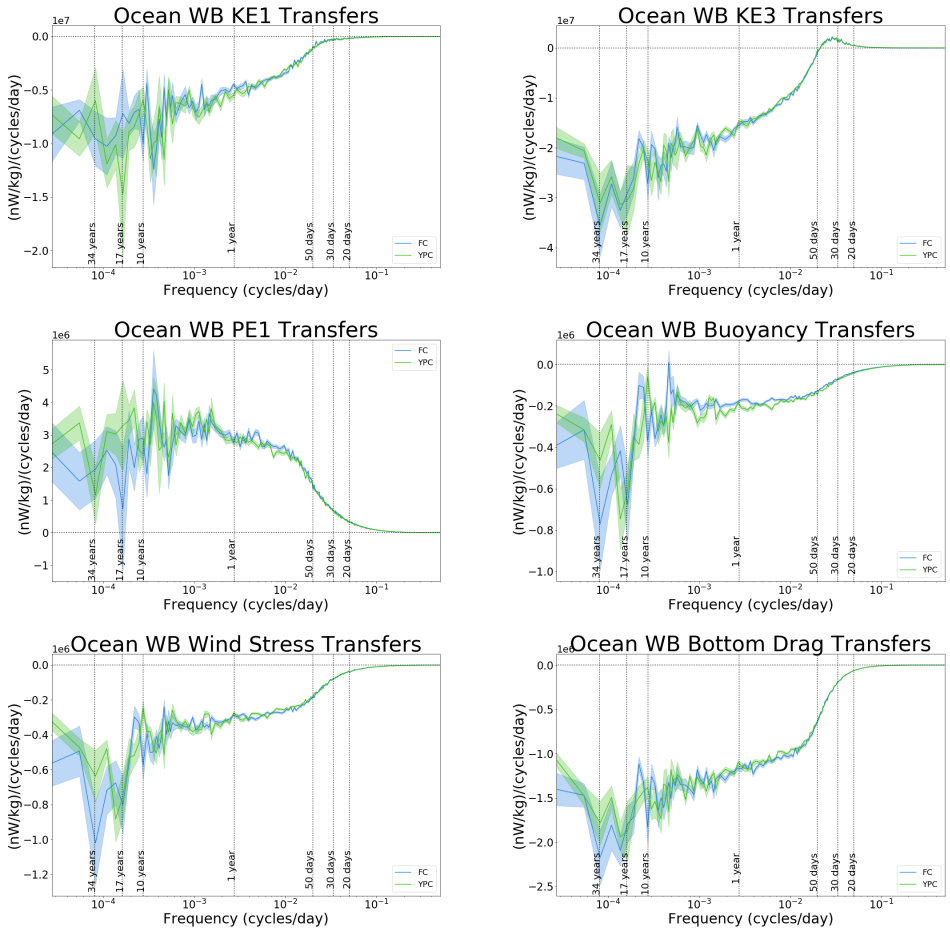

Figure 4.12: Ocean WB spectral energy transfers: comparison between FC (blue) and YPC (green).

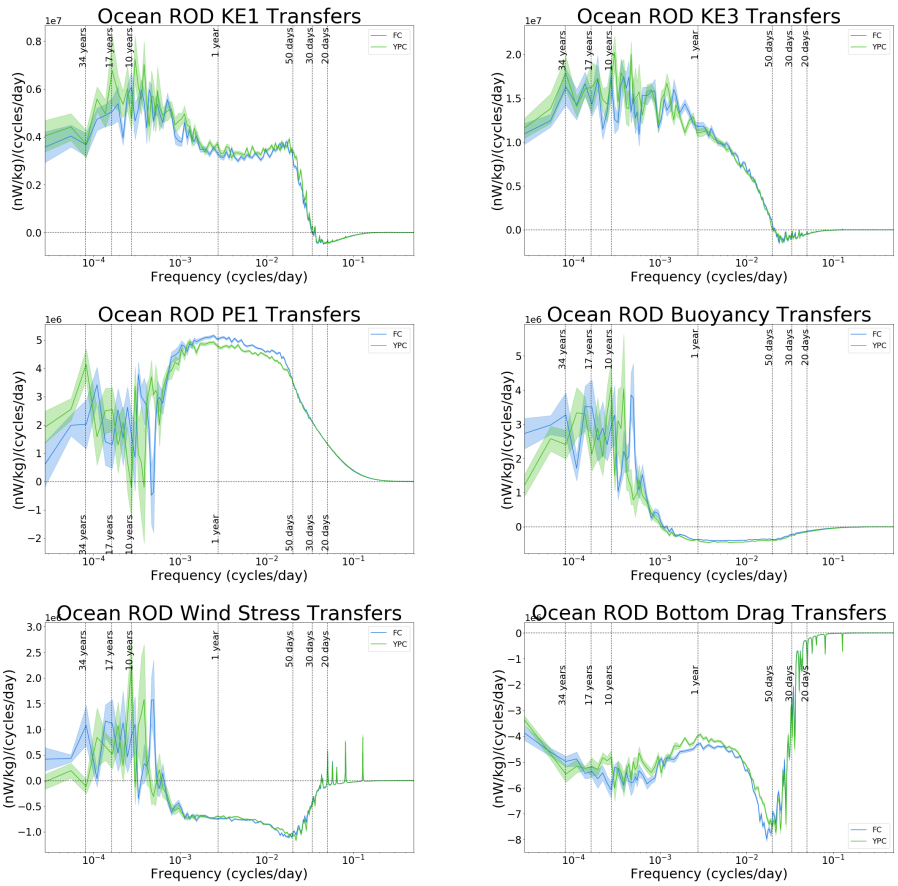

Figure 4.13: Ocean ROD spectral energy transfers: comparison between FC (blue) and YPC (green).

The ROD region (Figure 4.9b) shows greater differences between YPC and FC at high frequencies, compared to either WB or CS. The YPC buoyancy term starts at the shortest timescale of 2 days nearly 45% greater than the FC run and the gap roughly linearly decreases until around 50 days at which time the buoyancy term levels off at a magnitude about 10% greater than coupled until around 200 days. Both the PE1 and wind stress terms in ROD also display greater magnitude at high frequencies in the YPC run, but start at a magnitude about 15% greater, linearly decreasing to the 1:1 line at about 20 days. At high frequencies, then, it appears that the ocean buoyancy term transfers more energy in YPC compared to FC in the ROD and WB regions, but is nearly unaffected in the CS region.

It is not surprising that the buoyancy term sees the greatest impact of the YPC coupling, since it is the term that depends directly on the SST field. However, it is interesting how the other ocean transfer terms adjust (or not) to the change in buoyancy. In the WB, the other terms barely change at all, while in ROD all of the terms are at least 10% different between YPC and FC, except for the bottom drag term, that remains close to the 1:1 line. It thus appears that the removal of ocean dynamics in the advection of SST increases the energy transfer in the buoyancy term throughout the ocean, but with a far lesser impact over the CS region. We interpret this as an indication that the CS region is mostly intrinsically driven at high frequencies. We also propose that these high-frequency results suggest that the WB is somewhat intrinsically-driven, given that the buoyancy term does adjust to the altered SST field, but that the rest of the terms remain relatively robust to the change. By the same reasoning, the high-frequency differences in ROD then suggest that the ocean is less intrinsically-driven and thus more vulnerable to external influence away from the WB and CS regions at short timescales. These regional high-frequency results only further strengthen the argument that the CS is primarily intrinsically ocean-driven.

Next we turn our attention to the 17-year timescale, and Figure 4.11 shows the CS transfer terms. KE1, KE3, and PE1 all show almost complete agreement between YPC and FC at their 17-year peaks, indicating that there is no difference between the two runs in these terms. These are all intrinsically-driven terms, in that they depend only on oceanic variables. The other intrinsic ocean term, the bottom drag, also shows near agreement between YPC and FC at 17 years. On the other hand, the two forced terms, buoyancy and wind stress, show somewhat opposing peaks at 17 years. However, the confidence envelopes are wide and slightly overlap at this timescale, and so we hesitate to draw any conclusions from the behavior. Nevertheless, it appears as though the intrinsic terms do not show a noticeable difference at 17 years, whereas the forced terms do appear to differ between YPC and FC.

The WB region (Figure 4.12) behaves a bit differently at 17 years. The terms that appear the most robust at the 17-year timescale are KE3 and bottom drag, both terms that act near the bottom of the water column. Both the buoyancy and wind stress terms behave very similarly, but don't quite overlap completely at 17 years. The PE1 and KE1 terms don't appear to show opposite-peak behavior, but there are large standard deviations. In the ROD region, we observe almost no peaked behavior at 17 years. These observations give more credence to our claim in Chapter III that the WB is a sink for the energy that is sourced from the CS. We have previously discussed numerous indications that the 17-year peak is an intrinsic mode of ocean variability primarily in the CS region, and the WB results here show that the major sink of energy for the 17-year mode appears to be in the third layer of the WB region. As for the partial coupling, these results also indicate that the ocean's intrinsic terms remain mostly robust to changes in the 17-year mode of variability, despite the observation that the forced terms may adjust to the altered coupling. These regional results thus further validate the theory that there is intrinsic ocean variability at 17 years that increases atmospheric variability at that time scale in the FC run, but that this mode

is damped in the YPC atmosphere.

With the source/sink pairing between CS and WB discussed above, we point out a few other interesting connections between the two regions, specifically in the KE1 term. At timescales of 10 years and longer in KE1, the CS region behaves almost identically to the domain-integrated in both configurations, even displaying the narrow opposing peaks at 10 years. The WB region also doesn't show any significant differences in KE1 between the two configurations at low frequencies. There do, however, appear to be a couple differences at timescales shorter than 10 years in these regional plots compared to their domain-integrated versions. In both CS and WB, the YPC line has a narrow peak toward larger magnitude at 6 years, while the FC peaks in the opposite direction at the exact same timescale. In the domain-integrated result, there is no significant difference between the two runs at 6 years. The same behavior is observed at 2.3 years, and we see that YPC is larger magnitude over a broad range of 250 days to 2 years. What is interesting here, is that in each of these cases, the adjustments that the WB and CS regions make in the YPC configuration compared to the coupled oppose one another quite exactly, which is consistent with the opposing behavior we have just discussed.

The fact that the KE1 term in the CS and WB region responds so identically opposite across the different model setups only strengthens the observation we made earlier and in the previous chapter that the two regions appear to balance one another. Not only do the two regions display opposite behavior but they also seem to respond to an altered model state in the exact opposite ways. This indicates that the two regions work together to balance each other out. However, earlier we saw that the KE1 term in CS appears to be balanced at low frequencies by KE3 in WB. What the previous paragraph suggests is that the KE1 terms balance one another in the mid-range frequencies. To better compare the KE1 terms in these two regions, we plot the ratios of selected transfer terms in CS to those in WB for both FC and YPC,

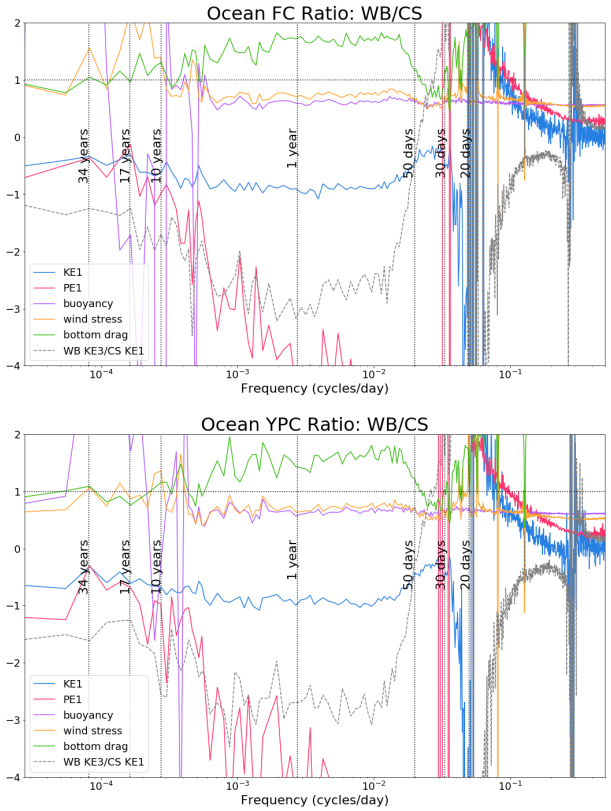

Figure 4.14: Ratios of WB to CS for select ocean spectral transfers in FC and YPC.

shown in Figure 4.14. Based on the above result that energy added to the system by CS KE1 appears to be extracted by WB KE3, we have added their ratio to the plot as a grey dashed line. Indeed, we notice several nearly constant ratios, which signify that the terms behave almost identically (whether the same or the opposite sign).

Between about 80 days and 5 years, the ratio of KE1 in both configurations hovers just shy of -1, and at lower frequencies the ratio drifts toward -0.5. The fact that the ratio remains roughly constant at -1 without large peaks indicates that the CS and WB transfers of KE1 have almost exactly opposite shapes in the mid-range frequencies. The fact that the ratio is almost exactly -1 suggests that KE1 in these two regions really do cancel each other out, though there are likely other terms involved as evidenced by the somewhat constant ratio between WB KE3 and CS KE1 at the same mid-range frequencies. The opposing behavior in the mid-range frequencies appears to also hold true for the bottom drag, wind stress, and buoyancy terms, with the two latter terms roughly constant throughout high frequencies as well. We observe that the ratio of WB KE3 to CS KE1 does appear roughly constant at low frequencies, though are not as obviously connected as we might have guessed from the noticeably peaked regional spectral transfers. All of this behavior is very similar across the FC and YPC model configurations. These ratios strongly indicate that there is a crucial connection between energy generated by the ocean in the CS region being extracted by the ocean in the WB, and that this connection is robust to the removal of ocean dynamics in SST advection.

In this chapter, we have decided to include some regionally-integrated results in the atmosphere as well. Although the atmosphere does not show as distinctly different dynamics in certain regions over others, we are interested in whether the region directly above the ocean is more affected by the oceanic forcing. Therefore, we show the atmospheric spectral transfers, integrated over the the region directly above the ocean (the entire area of the ocean basin) in Figure 4.15. Compared to their

domain-integrated counterparts, the main differences are the diminished increase in KE2 energy beyond 50 days, and the larger negative magnitude in the buoyancy term. Both of these observations make sense: the buoyancy term holds the information from the heat fluxes and SST field from the ocean, and the KE2 term gains a lot of its energy from the higher-velocity motions across the atmospheric channel.

If we compare the transfers over the ocean across the different model configurations, the most visible discrepancy is in the buoyancy and PE1 terms at low frequencies. In the FC case, low-frequency buoyancy approaches and remains close to zero. In YPC, the buoyancy term crosses zero near 8 years and becomes a source of energy, and this source appears to be balanced by the PE1 term that is more negative that in the FC case. Although ATO will be discussed in the next section, we will mention that the buoyancy term in ATO remains negative throughout the low frequencies, and the PE1 responds by remaining (mostly) positive. The buoyancy term behavior in these three plots exactly matches what we observed in the domain-integrated buoyancy transfer in Figure 4.6, indicating that the atmospheric buoyancy term essentially only acts over the ocean domain, which is again, not very surprising. The PE1 term, on the other hand, does not display the same low-frequency behavior in the regionally- versus domain-integrated transfers, and so we can infer that the PE1 term has a large contribution over the land points in the model.

To discern any differences in high-frequency behavior, we look at the atmospheric ratios of YPC versus FC spectral transfers over the ocean, shown in Figure 4.7c. We do observe differences (greater than 10%) at high frequencies in almost all of the terms, except for buoyancy. This is a telling feature of the high-frequency behavior across the YPC and FC configurations. This result implies that the slight increase in energy transfer at high frequencies may not be a direct consequence of the modified SST field, since it is specifically the buoyancy term over the ocean that should respond most directly to the YPC setup. However, what is seen is that the buoyancy is the

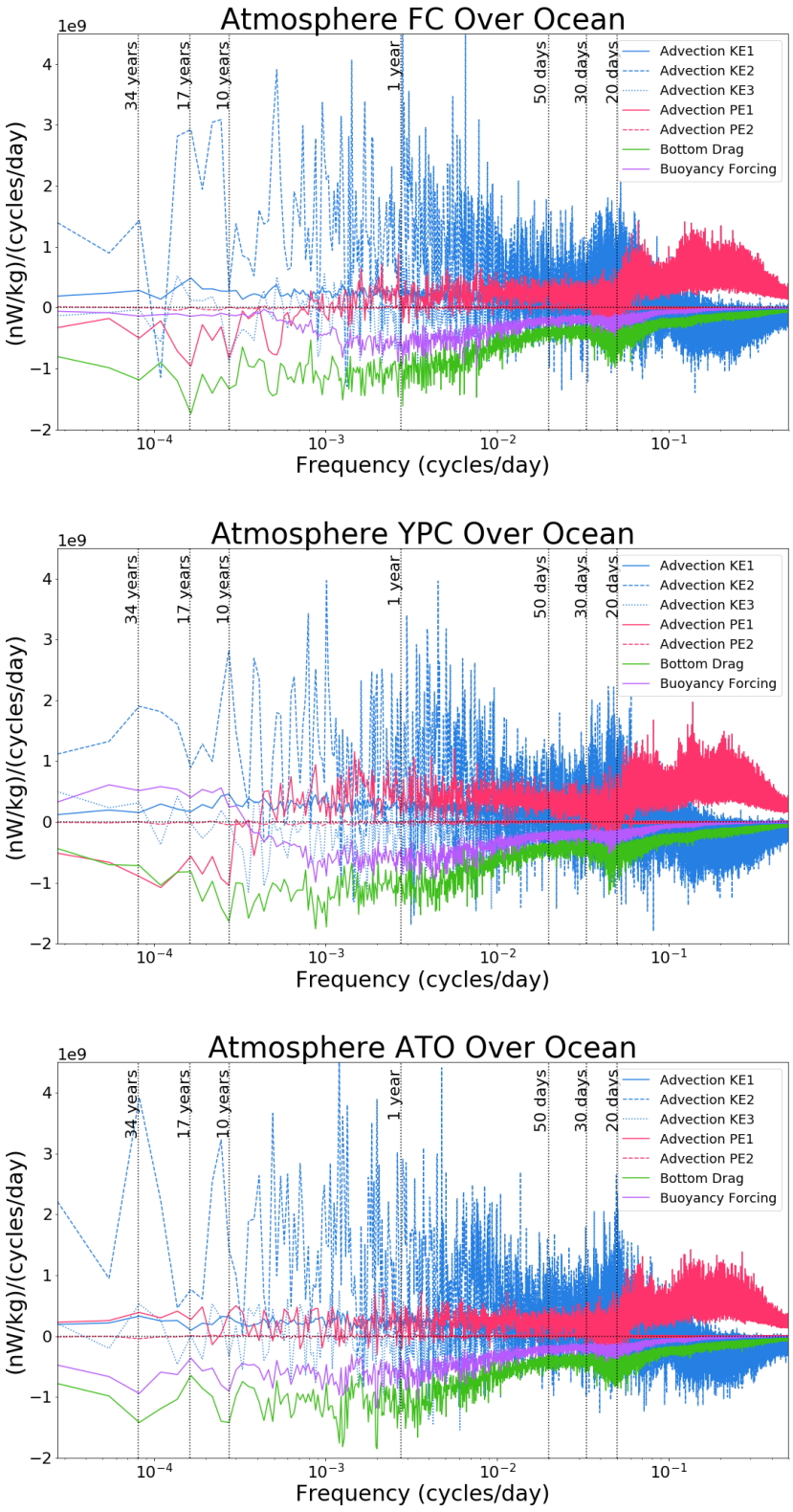

Figure 4.15: Regionally-integrated atmosphere spectral energy transfers directly over the ocean basin for FC, YPC, and ATO.

only term that does not show an increase in YPC energy transfer at high frequencies over the ocean. In the domain-integrated transfers, though, the buoyancy term does appear to be slightly greater at high-frequencies. These observations suggest that the ocean effects on the atmospheric buoyancy term are not directly responsible for these high-frequency discrepancies, which are instead due to other processes adjusting to the partial coupling, possibly a forward energy cascade, or an influence from the relative stress term (bottom drag in the atmosphere) that has greater magnitude for much of the high-frequencies, up through nearly 100 days.

Yet again, these regional ocean results demonstrate that the domain-integrated ocean fails to capture significant regional behavior. We have found numerous differences in the regions, that also indicate how each region responds to a change in SST. We have found three main results so far: (1) there are high-frequency differences between coupled and YPC in the atmosphere and certain ocean terms/regions that is likely not directly due to the modified SST field, (2) there is an ocean-driven mode of variability at 17 years that is translated to the atmosphere via an eddying SST field in the FC run, and is not present in the YPC run, and (3) the CS is primarily intrinsically sourced and directly opposed by the WB. Next, we will look at what we call the atmosphere-only run, where we prescribe a climatological SST field and do not run the ocean portion of the model. In our analysis of the ATO run, we are particularly interested in how the absence of the ocean affects results (1) and (2) above (the results pertaining to the atmosphere).

4.3.3 Atmosphere-Only Configuration

We now consider the atmosphere-only configuration (ATO), where the only oceanic influence in the system is in the form of an averaged SST field. We focus on how the ATO run behaves at the two timescales of interest, namely at (1) short timescales (on the order of days) and at (2) 17 years. There is other interesting behavior in the

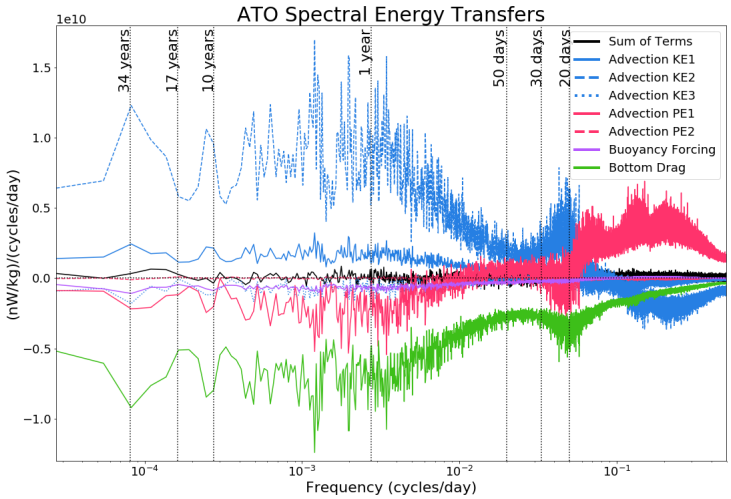

Figure 4.16: Domain-integrated ATO spectral energy transfers

ATO results, but for time constraints we leave this for future work.

For completeness, we plot all of the domain-integrated spectral transfer terms together in Figure 4.16. However, we find the kinetic energy spectra and domain-integrated spectral transfers shown in orange in Figures 4.3a and 4.6, respectively, alongside the FC (blue) and YPC (green) model runs, to be more revealing. Again, the ATO configuration does not show any major differences in the shape and magnitude of either the spectra or spectral transfers. As in the YPC case, one of the largest differences in ATO compared to FC is at 17 years. At this timescale, the ATO and YPC spectra coincide, both showing a dip in energy and energy transfer in all of the terms (except buoyancy), opposing the peak toward larger magnitude in the FC setup. This agreement is expected, given our previous indications that the FC peak at 17 years is driven by intrinsic ocean dynamics, which are either non-existent or not translated to the atmosphere in either the YPC or ATO cases. There does appear to be slightly differing behavior just shy of 17 years in YPC and ATO, though, where the ATO terms (both spectra and transfers) display a broader peak that is centered near 15 years. In future work it would be interesting to tease apart the differences

and similarities between the YPC and ATO configurations, but here we must limit our scope to the two time scales of interest.

With the 17-year opposing peaks in agreement with our findings across the different model runs, we now investigate the high-frequency behavior and observe some puzzling results. The ATO and FC runs appear to behave nearly identically at high frequencies, across all terms in the spectra and spectral transfers, as is visible in the ratios of the spectra (Figure 4.4) and spectral transfers (Figure 4.7b and d). All of the ATO to FC ratios (spectra, domain-integrated transfers, and over-ocean transfers) lie almost perfectly on the 1:1 line at high frequencies, from 2 to around 50 days. This result is surprising, because we might have expected that the ATO run, with more simplifications in the ocean to atmosphere coupling, would show even more differences from the FC run than the YPC run does. However, the high-frequency behavior disagrees with this theory.

To help understand this discrepancy between YPC and ATO, we consider their differences in model configuration. The biggest difference is that YPC still has a dynamic ocean that is able to communicate with the atmosphere via relative wind stress, whereas the ATO setup has no ocean dynamics whatsoever. Previously, we noted that buoyancy is likely not the candidate responsible for the high-frequency differences in YPC and ATO, but that the relative wind stress term might be a contributor. If the relative stress is in fact causing this high-frequency behavior, then it makes sense that the YPC and ATO runs would behave differently at short timescales, and we discuss this hypothesis further in Section 4.4.

4.4 Discussion

We have compared spectral energy transfers across three different Q-GCM model configurations, with a focus on the distinctions between YPC and FC, which indicate the effect that ocean dynamics have on the atmosphere. We identified two primary

differences between YPC and FC: (1) at a timescale of 17 years, YPC is oppositely peaked compared to FC in the atmospheric spectra and spectral transfers; (2) YPC spectra and spectral transfers are greater than those in the FC run at high frequencies in every atmospheric and some oceanic terms. Following these two observations, we investigated these two timescales in the ATO model configuration as well, and found that the ATO corroborates the YPC story at 17-years, but complicates the high-frequency story. While investigating the previous results, we also found a strong connection between the ocean's CS and WB regions, whereby intrinsic ocean energy is sourced in the CS region and is extracted by the WB region.

We postulate that there is an intrinsic mode of variability in the Q-GCM ocean at a 17-year timescale, and that this mode is imprinted in the atmosphere via the role that ocean dynamics play in SST advection. As previously discussed, the 17-year mode of intrinsic ocean variability is consistent with results from *Hogg et al.* (2006), who used a different method to study variability in Q-GCM. In Section 4.1, we mentioned that *Hogg et al.* (2006) found that ocean dynamics projected onto existing modes of atmospheric variability, rather than creating new modes. The analysis used here does not make it clear if this is the case in our results, though the opposite peaks at 17 years could indicate that the ocean in fact excites a new mode at 17 years in the atmosphere. What our findings do show is that there is a 17-year mode of intrinsic ocean variability that is communicated to the atmosphere from the ocean dynamics by way of the SST field. Our results thus suggest that climate models without explicit ocean dynamics may underestimate low-frequency atmospheric variability.

With our finding that the 17-year mode of variability is intrinsically-driven, and dominated by the injection of energy in the CS region (the Gulf-Stream-like current in our model), we have shown that behavior from the CS can penetrate beyond the atmospheric boundary layer and into the troposphere. The 17-year peaks are quite visible in the first and second atmospheric layers, reaching a vertical height of 5

kilometers (roughly half the height of the real troposphere). These results are in agreement with *Minobe et al.* (2008) who find that the Gulf Stream can influence the whole troposphere. Their analysis uses observations, and thus relies on many more aspects of ocean-atmosphere coupling (e.g. clouds and precipitation) than are present in Q-GCM. The present findings indicate that a Gulf-Stream-like current can impact the troposphere via relatively simple momentum and heat flux coupling, without any moisture effects.

There have been other papers that find a similar interdecadal signature of ocean-driven variability as we have found here at 17 years. A turbulent oscillator mode was proposed by *Berloff et al.* (2007b) with a rough timescale of 12 years, and has been found in other QG models (e.g. *Shevchenko et al.* 2016). This mode is characterized by changes to the magnitude and position of the oceanic jet in the western boundary current separation region, and the associated changes to the subtropical gyre. Although we didn't discuss this in detail, we remind the reader that we did observe an asymmetry between the gyres, with a reduction in size of the subtropical gyre, in the YPC SST fields shown in Figures 4.2b and e. It is thus plausible that the turbulent oscillator mode is associated with a 17-year mode of variability in our model, instead of the 12-year signal seen in *Berloff et al.* (2007b). There are other established low-frequency modes of variability in the ocean that may be similar to what we've found here, such as the gyre mode introduced by *Simonnet and Dijkstra* (2002). The gyre mode has been characterized by dynamical systems approaches to studying variability, with the identification of bifurcations in the system, and is typically associated with slightly higher frequency behavior, at timescales closer to 7 or 8 years. More work would be needed to determine if the gyre mode is present in Q-GCM.

While focusing on how the atmosphere is affected by the ocean dynamics, we also found some interesting behavior in the ocean, based on how it adjusts to the YPC

configuration. By comparing the CS and WB regional spectral transfers (particularly the KE terms), as well as observing that they adjust nearly identically to the YPC SST modification, we argue that the CS and WB regions work together as a sort of source/sink dipole. Energy is injected into the ocean in the CS region, and is removed by the WB region. Their opposing role is made clear by their nearly constant ratios of spectral transfer terms in WB to those in CS, combined with the fact that the response of the CS KE terms to the YPC setup is almost identically opposite to the response by the WB KE terms. At decadal scales and longer, this relationship is particularly visible in the KE1 term in CS with the KE3 term in WB. These results thus give credibility to the finding suggested in Chapter III that energy generated in the CS region is extracted in the WB region, and that the low-frequency energy appears to be mostly sourced in the first layer of CS and removed near the bottom of the water column in WB. Our findings are consistent with *Zhai et al.* (2010), as we have previously stated, and add more information about the source of the energy that is extracted along the WB, as well as the timescales involved.

At high frequencies, we have discovered differences between the model configurations in both fluids, at timescales from 2 to 20 days, and even longer in some of the terms. This result could be exciting, as it may indicate that the ocean can impact the atmosphere at short timescales, in contrast to the traditional view espoused by *Bjerknes* (1964) and *Gulev et al.* (2013). We must keep in mind, however, that their results were based on model and in situ data that did not resolve high-frequency and high-wavenumber motions (eddies) in the ocean, and so they did not see these effects on the atmosphere. While there are many studies on low-frequency ocean variability, there has been less interest in high-frequency ocean variability and how it affects the atmosphere, primarily due to the aforementioned and similar studies that assume the ocean is only capable of affecting the atmosphere at long timescales. Our results, however, are not straight forward, and in fact are a bit puzzling. We have shown

that removing the ocean dynamics from SST advection, such that the SST field is advected only by Ekman pumping, increases the magnitude of high-frequency energy transfer in the atmosphere and also, though slightly less ubiquitous, in the ocean. However, if we simplify the system even more by allowing only a time-averaged SST field (from the coupled scenario) to force the atmospheric mixed layer (ATO), the high frequencies match the coupled run almost exactly.

The hypothesis that we consider most likely to explain these results, is that the high-frequency behavior in the atmosphere may not stem directly from the modified, non-eddying SST field in the YPC and ATO runs. Instead, we postulate that the SST field in YPC may directly affect the oceanic buoyancy term (which is the only ocean term mathematically dependent on the SST field) at short timescales, primarily in the ROD, but also in the WB region. In ROD, most of the other terms react to the change in buoyancy at high frequencies, and this information is then translated to the atmosphere via the relative stress term in YPC. This conjecture explains why the YPC and ATO configurations do not match at high frequencies, and also why the ATO and FC setups do match at high frequencies. It also explains why the atmospheric buoyancy term is not greater in the region directly above the ocean in YPC compared to FC (because the high-frequency information is coming from another source), as well as why the stress terms adjust very noticeably at high frequencies. If this is in fact the case, then it is an example as to why we must be careful interpreting partially coupled results, since the entire system will adjust to any changes in the communication channel.

While the above conjecture for the high-frequency behavior may not be physically realistic, since the behavior is likely caused by spurious effects in the ocean due to partial coupling, the fact that the ocean can affect the atmosphere at short timescales remains true. Our hypothesis indicates that the eddying SST field feeds back onto the ocean and slightly damps the high-frequency energy transfer in certain terms, mostly

in the ROD region. We are then suggesting that these high-frequency modifications are translated via relative stress to the atmosphere, implying that the atmospheric stress term communicates ocean behavior at short timescales. We also acknowledge that there may be other behavior that can account for the results that we have found, especially with regards to energy cascades, which we have not addressed here (for the primary reason that they are more difficult to diagnose using the tools employed in this work).

Although the high-frequency differences may be unrealistic in our model, they still indicate that, under certain perturbations to the system, the ocean is capable of affecting the atmosphere at high frequencies. While these differences are only around 10%, this is still a potentially important result that should be considered in more complex models. After all, we know that atmospheric weather models predict weather reasonably accurately, but if the ocean could affect the atmosphere by up to 10%, particularly as certain coupling mechanisms are altered, the ocean may play an important role in improving predictability in weather and climate systems, particularly with regards to a changing climate.

CHAPTER V

Discussion

Identifying the underlying mechanisms driving climate variability is an incredibly difficult task because the system consists of inherently complex and coupled components, including the atmosphere and ocean. In this dissertation, we have used a spectral transfer framework in the frequency domain to identify the sources and sinks of energy across timescales from 2 days to 100 years in an idealized, midlatitude, coupled ocean-atmosphere model. Despite being a simplified and regional model, Q-GCM has yielded some interesting and unexpected behavior in regard to its energy sources and sinks, and the timescales at which coupling occurs in the system.

We have considered two different methods of attributing intrinsic versus forced behavior in each fluid. The first is based on the mathematical formulation of each term in the energy budget, and whether the term depends explicitly on oceanic or atmospheric variables. The second method involves altering the coupling between the fluids, and observing the resulting changes in the spectral transfers. The second method builds upon the first method by helping to determine the underlying drivers behind each of the terms in the energy budget, whether or not they explicitly depend on variables from the other fluid.

In all three of the Q-GCM configurations that we have analyzed in this work—fully coupled (FC), partially coupled with the removal of ocean dynamics driving the SST

field (YPC), and atmosphere-only with a dynamic atmosphere and climatological SST field (ATO)—we have found that nonlinear advection of kinetic energy is the leading source of energy at low frequencies in both fluids, while the potential energy dominates at higher frequencies. Both of these terms depend on variables internal to each fluid and are considered to be indicators of internal variability, and we thus conclude that both fluids are primarily intrinsically driven.

A major result of the ocean spectral transfer analysis is that the spectral transfers behave contrastingly in regions of differing ocean dynamics. We have observed especially interesting behavior in the eddy-active western boundary current separation (CS) region and the region along the western boundary (WB). Not only do we find the CS to be a large source of energy, while the WB is a major sink of energy, but we have also shown that several of the transfer terms (especially KE) in the two regions display opposing behavior. This result indicates that much of the energy input into the system in the CS region is extracted by the western boundary region. Physically, this suggests that eddies generated in the CS region propagate westward and are ultimately dissipated along the western boundary. This result is consistent with *Zhai et al.* (2010) who find that the WB is an eddy "graveyard" for westward propagating eddies. However, they look only at surface eddies in a one-layer model and in satellite data. The results in this dissertation indicate that low-frequency behavior is largely removed by the third layer KE term at the bottom of the WB region. Furthermore, we have shown here that the primary source of eddy energy that ultimately gets extracted by the WB "graveyard" is the upper layer of the CS region. To get a fuller picture of what's happening in our model, we examine an animation of Q-GCM layer 1 potential vorticity - a field that prominently shows the eddying motion in the ocean. The animation shows an eastward jet that protrudes from the western edge of the ocean basin. This eastward jet sheds eddies to the north and south, and it appears as though these eddies then travel westward, back toward the

western boundary. Our results suggest that this behavior is the largest contributor to the energy budget throughout the oceanic domain.

Implied in the explanation given above, in which eddies generated in the CS region are dissipated in the WB, is the fact that the CS region is largely intrinsically-driven. This result is apparent not only due to the fact that the CS region is dominated by kinetic energy advection, but also because the CS region is relatively robust to the coupling changes in the YPC model setup. It is perhaps not surprising that a region of rich eddy activity is mostly intrinsically ocean-driven, and agrees with several previously discussed studies that have also found oceanic modes of variability to be centered around the eddy-active regions in the ocean (e.g. *Hogg et al.* 2006; *Shevchenko et al.* 2016; *Berloff et al.* 2007b; *Penduff et al.* 2011; *Sérazin et al.* 2015; *Kiss and Frankcombe* 2016).

Another focus of this dissertation is to quantify the impact of the ocean on the atmosphere, with special interest in any possible effects at high frequencies. It is generally accepted that the ocean may control low-frequency ocean-atmosphere coupling, but that the atmosphere is the primary driver of high-frequency coupling (*Bjerknes*, 1964; *Gulev et al.*, 2013). However, with increasing ocean resolution in modeling and the emerging research that the oceanic eddy field may play a larger role in ocean energetics and climate variability than previously thought (e.g. *Chelton et al.* 2004; *Small et al.* 2008; *Renault et al.* 2019; *Jia et al.* 2019), there has been renewed interest in determining how much of an imprint ocean eddies leave on the atmosphere. With our highly turbulent and eddy-resolving model, we find that the ocean dynamics may in fact be able to adjust the energy transfer in the atmosphere by up to 10% at scales shorter than 20 days. It it possible that this high-frequency difference could be related to the ability of ocean eddies to imprint small-scale features in the atmosphere, as found by several sources including *Chelton et al.* (2004) and *Moulin and Wirth* (2016), though we have found that these high-frequency differences are likely a result of the

relative stress terms. Although the current work is not conclusive in determining exactly how the ocean affects these high-frequency adjustments in the atmosphere, this is a potentially important result with respect to weather and climate prediction, indicating that the inclusion of ocean dynamics may increase predictability of the system.

Of course, it is important to recognize the limitations of our analysis. As a quasi-geostrophic model, Q-GCM emphasizes the nonlinearity in oceanic and atmospheric flows, which is especially important in midlatitude climate dynamics. However, there are some significant simplifications that are made in Q-GCM such that our results should be taken with caution. For instance, there is no moisture in our model (so no cloud or evaporation feedbacks), the vertical resolution is coarse, the coastlines are idealized, there is no topography, the heat fluxes are parameterized, there is no daily or seasonal variation in the solar radiation, etc. On the other hand, Q-GCM is noticeably more complex than the idealized, single-fluid, doubly periodic, QG turbulence models used in previous work on frequency-domain spectral transfers, such as *Arbic et al.* (2012, 2014). With solid boundaries, Q-GCM displays distinct dynamical regions within its double-gyre configuration, mimicking the ocean circulation in the North Atlantic basin. Additionally, the fact that Q-GCM is a coupled model sets it apart from many models of similar complexity. Despite its shortcomings, we argue that Q-GCM is well-suited for studying ocean-atmosphere variability, and can help with the understanding of more realistic and complex models, as well as the actual climate system.

While our results likely hold true for any double-gyre configuration in the ocean, we have chosen to tune Q-GCM parameters to roughly match those associated with the North Atlantic Ocean. This choice stems from the great interest in predicting North Atlantic variability, largely due to its effect on North American and European weather and climate (e.g. *Sutton and Hodson* 2005; *Scaife et al.* 2008). Aspects of

the North Atlantic Ocean are seen as particularly vulnerable to climate change, and it has been shown (e.g. *Dijkstra and Ghil* 2005 and papers cited therein) that surface dynamics in the North Atlantic Ocean and their coupling with the atmosphere may play a large role in the region's climate variability.

The spectral transfer diagnostic also limits the scope of this work to eddy-eddy interactions, with no explicit eddy-mean flow interactions—an important contributor to climate variability. However, ocean eddies are known to be a dominant component of the climate system in midlatitudes, and Q-GCM is a highly turbulent, eddy-resolving model that aptly captures eddy-driven behavior. Our analysis would likely benefit from a combined frequency-wavenumber analysis, but in order to resolve decadal-scale variability our computing and time resources were limited to focusing only on a frequency-domain analysis. But, future work might benefit from comparing spatial and temporal scales together. Due to the simplifications, we are cautious in interpreting the timescales introduced in this dissertation exactly. Still, we can infer some possible connections with real-world behavior. For example, our 17-year behavior may be related to observed interdecadal climate variability discussed, e.g., by *Moron et al.* (1998), who find a 13- to 15-year mode of variability due to interaction between the Gulf Stream and the subpolar gyre.

In this dissertation, we have shown that the spectral transfer technique, particularly in the frequency domain, is a promising tool for differentiating the contribution of individual processes to the overall behavior of a coupled climate system. While similar in many ways to the kinetic energy spectra, they also reveal some different timescales of variability. An obvious missing piece to the story we have told so far is an explicit spectral transfer analysis within the mixed layers in the system, which would reveal the source and sink behavior of the temperature advection and heat flux terms. Spectral transfers of terms in the temperature variance equation would likely aid in the determination of the source of high-frequency differences between the fully

coupled (FC) and atmosphere-only (ATO) runs compared to the Y_C partial coupling (YPC), since the primary difference between the FC, ATO, and YPC runs lies in the SST field. Such analysis is forthcoming.

There are two model configurations that would be straightforward to run, which could help inform the current results: an ocean-only run (with a prescribed atmospheric surface temperature) and another partially coupled run that is already built into Q-GCM. This other partially coupled run removes the time-varying diabatic forcing from reaching the quasi-geostrophic atmosphere; instead, the atmosphere sees a climatological average contribution of the heat fluxes. The main reason we did not include these runs in the present work is because we considered these two setups to be less indicative of how the ocean affects the atmosphere. A third potentially illuminating model run would be the YPC configuration (and possibly the fully coupled as well) without relative wind stress, in order to test our hypothesis on the source of the high-frequency differences in our results. These three scenarios could be fruitful directions to explore in the near future.

We recognize that the results from the spectral transfer analysis shown here would be bolstered by the comparison with other techniques, such as an analysis based on empirical orthogonal functions (EOFs). Because EOFs are particularly useful for identifying specific modes and patterns of variability, an EOF analysis would compliment the frequency-domain spectral transfer technique used in this dissertation. *Hogg et al.* (2006) perform an EOF analysis on certain Q-GCM variables, as we have discussed in this work, but an EOF analysis on the specific terms relevant to this study would help further explain our results and possibly help diagnose the underlying mechanisms in the behavior we have observed.

Perhaps one of the more intriguing parts of this work has been the wealth of results obtained. We have largely focused here on the important near-daily and interdecadal timescales, but there is additional behavior at other frequencies in our results that

could be very insightful. We have chosen to focus on the two timescales that we find particularly interesting with respect to the ocean impacting the atmosphere, and hope that future work might be able to delve into the other interesting behavior in our results.

It is crucial to highlight the importance of idealized studies like this one, which may seem far removed from the real climate system that it aims to model. However, in complex systems like the Earth's weather and climate, it can be quite challenging to understand the principles underlying the system's behavior. Research using simplified models like we have used in this thesis is crucial to help garner insight into the governing mechanisms of the climate system, and is essential in order to verify that more realistic models are correctly capturing the system's dynamics. In turn, the better the realistic models, the more accurately we can predict future variations in the weather and climate systems.

Weather and climate predictions are vital for human civilization for a number of reasons, including food security, habitability, and mitigation of the effects of extreme weather events. As an example of the importance of predicting climate variability with respect to food security, the rising ocean temperatures and changes in ocean currents are having major effects on marine ecosystems. For instance, coral reefs are an extremely important ecosystem for marine life, and provide a source of seafood for around 500 million people worldwide—an industry with great economic impact and an annual revenue of more than $5 billion (*Porter et al.*, 2014). In the North Atlantic Ocean, studied in this thesis, the coral reef systems in the eastern portion of the Caribbean are under threat due primarily to increasing ocean temperatures, which would have devastating effects on the fishing and tourism industries in those areas. In addition, increasing surface ocean temperatures have been linked to an increase in tropical cyclones and hurricanes, which in turn cause more damage to marine, as well as human, ecosystems (*Hoegh-Guldberg et al.*, 2014). Accurate prediction of how

the climate will change over the coming years and decades is necessary in order to maintain productive fisheries and other food sources to feed the global population.

In conclusion, this idealized study has used a frequency-domain spectral transfer diagnostic to reveal some expected and some surprising behavior in the coupling between the ocean and the atmosphere. This dissertation has also shown that there are still many mysteries regarding the identification of underlying drivers in coupled climate variability. With the increasing complexity of large-scale climate models, which push the boundary of modern-day computing resources, intuition gained from idealized studies, such as this one, could prove extremely valuable to help with the design and interpretation of global climate models. Moreover, comprehending the fundamental exchange of energy between the ocean and atmosphere systems is crucial to better understand, predict, and mitigate against the Earth's evolving climate.

BIBLIOGRAPHY

BIBLIOGRAPHY

Arbic, B. K., R. B. Scott, G. R. Flierl, A. J. Morten, J. G. Richman, and J. F. Shriver (2012), Nonlinear cascades of surface oceanic geostrophic kinetic energy in the frequency domain, *Journal of Physical Oceanography*, *42*(9), 1577–1600, doi: 10.1175/JPO-D-11-0151.1.

Arbic, B. K., M. Müller, J. G. Richman, J. F. Shriver, A. J. Morten, R. B. Scott, G. Sérazin, and T. Penduff (2014), Geostrophic turbulence in the frequency-wavenumber domain: Eddy-driven low-frequency variability, *Journal of Physical Oceanography*, *44*(8), 2050–2069, doi:10.1175/JPO-D-13-054.1.

Barsugli, J. J., and D. S. Battisti (1998), The basic effects of atmosphereocean thermal coupling on midlatitude variability, *Journal of the Atmospheric Sciences*, *55*(4), 477–493, doi:10.1175/1520-0469(1998)055<0477:TBEOAO>2.0.CO;2.

Batchelor, G. K. (1953), *The theory of homogeneous turbulence*, Cambridge University Press.

Berloff, P., W. Dewar, S. Kravtsov, and J. McWilliams (2007a), Ocean eddy dynamics in a coupled ocean-atmosphere model, *Journal of Physical Oceanography*, *37*(5), 1103–1121, doi:10.1175/JPO3041.1.

Berloff, P., A. M. Hogg, and W. Dewar (2007b), The turbulent oscillator: A mechanism of low-frequency variability of the wind-driven ocean gyres, *Journal of Physical Oceanography*, *37*(9), 2363–2386.

Bjerknes, J. (1964), Atlantic air-sea interaction, pp. 1 – 82, Elsevier, doi: https://doi.org/10.1016/S0065-2687(08)60005-9.

Bladé, I. (1997), The influence of midlatitude ocean-atmosphere coupling on the low-frequency variability of a gcm. part i: No tropical sst forcing, *Journal of Climate*, *10*(8), 2087–2106, doi:10.1175/1520-0442(1997)010<2087:TIOMOA>2.0.CO;2.

Charney, J. G. (1971), Geostrophic turbulence, *Journal of the Atmospheric Sciences*, *28*(6), 1087–1095, doi:10.1175/1520-0469(1971)028<1087:GT>2.0.CO;2.

Chelton, D. B., M. G. Schlax, M. H. Freilich, and R. F. Milliff (2004), Satellite measurements reveal persistent small-scale features in ocean winds, *Science*, *303*(5660), 978–983, doi:10.1126/science.1091901.

Dask Website (), Dask: Scalable Analytics in Python, https://dask.org, accessed: 2019-05-11.

Dewar, W. K. (2003), Nonlinear midlatitude ocean adjustment, *Journal of Physical Oceanography*, *33*(5), 1057–1082, doi:10.1175/1520-0485(2003)033<1057:NMOA>2.0.CO;2.

Dijkstra, H. A., and M. Ghil (2005), Low-frequency variability of the large-scale ocean circulation: A dynamical systems approach, *Reviews of Geophysics*, *43*(3), doi:10.1029/2002RG000122.

Duhaut, T. H. A., and D. N. Straub (2006), Wind stress dependence on ocean surface velocity: Implications for mechanical energy input to ocean circulation, *Journal of Physical Oceanography*, *36*(2), 202–211, doi:10.1175/JPO2842.1.

Farneti, R. (2007), Coupled interannual Rossby waves in a quasigeostrophic ocean-atmosphere model, *Journal of Physical Oceanography*, *37*(5), 1192–1214, doi:10.1175/JPO3061.1.

Feliks, Y., A. W. Robertson, and M. Ghil (2016), Interannual variability in north atlantic weather: Data analysis and a quasigeostrophic model, *Journal of the Atmospheric Sciences*, *73*(8), 3227–3248, doi:10.1175/JAS-D-15-0297.1.

Fjørtoft, R. (1953), On the changes in the spectral distribution of kinetic energy for two-dimensional, nondivergent flow, *Tellus*, *5*(3), 225–230, doi:10.1111/j.2153-3490.1953.tb01051.x.

Flierl, G. R. (1978), Models of vertical structure and the calibration of two-layer models, *Dynamics of Atmospheres and Oceans*, *2*(4), 341 – 381, doi:https://doi.org/10.1016/0377-0265(78)90002-7.

Gulev, S. K., M. Latif, N. Keenlyside, W. Park, and K. P. Koltermann (2013), North atlantic ocean control on surface heat flux on multidecadal timescales, *Nature*, *499*, 464 EP –.

Hayashi, Y. (1980), Estimation of nonlinear energy transfer spectra by the cross-spectral method, *Journal of the Atmospheric Sciences*, *37*(2), 299–307, doi:10.1175/1520-0469(1980)037<0299:EONETS>2.0.CO;2.

Hoegh-Guldberg, O., R. Cai, E. Poloczanska, P. Brewer, S. Sundby, K. Hilmi, V. Fabry, and S. Jung (2014), The ocean, in *Climate Change 2014: Impacts, Adaptation, and Vulnerability. Part B: Regional Aspects. Contribution of Working Group II to the Fifth Assessment Report of the Intergovernmental Panel on Climate Change*, edited by V. Barros, C. Field, D. Dokken, M. Mastrandrea, K. Mach, T. Bilir, M. Chatterjee, K. Ebi, Y. Estrada, R. Genova, B. Girma, E. Kissel, A. Levy, S. MacCracken, P. Mastrandrea, and L. White, book section 30, pp. 1655–1731, Cambridge University Press, Cambridge, United Kingdom and New York, NY, USA.

Hogg, A. M., J. R. Blundell, W. K. Dewar, and P. D. Killworth (2014), *Formulation and users' guide for Q-GCM*.

Hogg, A. M. C., and J. R. Blundell (2006), Interdecadal variability of the southern ocean, *Journal of Physical Oceanography*, *36*(8), 1626–1645, doi: 10.1175/JPO2934.1.

Hogg, A. M. C., W. K. Dewar, P. D. Killworth, and J. R. Blundell (2003), A quasi-geostrophic coupled model (Q-GCM), *Monthly Weather Review*, *131*(10), 2261–2278, doi:10.1175/1520-0493(2003)131<2261:AQCMQ>2.0.CO;2.

Hogg, A. M. C., W. K. Dewar, P. D. Killworth, and J. R. Blundell (2006), Decadal variability of the midlatitude climate system driven by the ocean circulation, *Journal of Climate*, *19*(7), 1149–1166, doi:10.1175/JCLI3651.1.

Hua, B. L., and D. B. Haidvogel (1986), Numerical simulations of the vertical structure of quasi-geostrophic turbulence, *Journal of the Atmospheric Sciences*, *43*(23), 2923–2936, doi:10.1175/1520-0469(1986)043<2923:NSOTVS>2.0.CO;2.

Huck, T., O. Arzel, and F. Sévellec (2015), Multidecadal variability of the overturning circulation in presence of eddy turbulence, *Journal of Physical Oceanography*, *45*(1), 157–173, doi:10.1175/JPO-D-14-0114.1.

Hurrell, J. W., and C. Deser (2010), North atlantic climate variability: The role of the north atlantic oscillation, *Journal of Marine Systems*, *79*(3), 231 – 244, doi:https://doi.org/10.1016/j.jmarsys.2009.11.002, impact of climate variability on marine ecosystems: A comparative approach.

Jia, Y., P. Chang, I. Szunyogh, R. Saravanan, and J. T. Bacmeister (2019), A modeling strategy for the investigation of the effect of mesoscale sst variability on atmospheric dynamics, *Geophysical Research Letters*, doi:10.1029/2019GL081960.

Kiss, A. E., and L. M. Frankcombe (2016), The influence of periodic forcing on the time dependence of western boundary currents: Phase locking, chaos, and mechanisms of low-frequency variability, *Journal of Physical Oceanography*, *46*, 1117–1136.

Kolmogorov, A. (1941), The Local Structure of Turbulence in Incompressible Viscous Fluid for Very Large Reynolds' Numbers, *Akademiia Nauk SSSR Doklady*, *30*, 301–305.

Kraichnan, R. (1967), Inertial ranges in two-dimensional turbulence, *Physics of Fluids*, *10*, 1417–1423, doi:10.1063/1.1762301.

Kraichnan, R. H. (1971), Inertial-range transfer in two- and three-dimensional turbulence, *Journal of Fluid Mechanics*, *47*(3), 525?535, doi: 10.1017/S0022112071001216.

Kravtsov, S., P. Berloff, W. K. Dewar, M. Ghil, and J. C. McWilliams (2006), Dynamical origin of low-frequency variability in a highly nonlinear midlatitude coupled model, *Journal of Climate*, *19*(24), 6391–6408, doi:10.1175/JCLI3976.1.

LaCasce, J. H. (2002), On turbulence and normal modes in a basin, *Journal of Marine Research*, *60*(3), 431–460, doi:10.1357/002224002762231160.

Larichev, V. D., and I. M. Held (1995), Eddy amplitudes and fluxes in a homogeneous model of fully developed baroclinic instability, *Journal of Physical Oceanography*, *25*(10), 2285–2297, doi:10.1175/1520-0485(1995)025<2285:EAAFIA>2.0.CO;2.

Larson, S. M., D. J. Vimont, A. C. Clement, and B. P. Kirtman (2018), How momentum coupling affects sst variance and large-scale pacific climate variability in cesm, *Journal of Climate*, *31*(7), 2927–2944, doi:10.1175/JCLI-D-17-0645.1.

Lorenz, E. N. (1979), Forced and free variations of weather and climate, *Journal of the Atmospheric Sciences*, *36*(8), 1367–1376, doi:10.1175/1520-0469(1979)036<1367:FAFVOW>2.0.CO;2.

Maasch, K. A., R. Oglesby, and A. Fournier (2005), Barry saltzman and the theory of climate, *Journal of Climate*, *18*, 2141–2150, doi:10.1175/JCLI3383.1.

Manabe, S., and R. J. Stouffer (1996), Low-frequency variability of surface air temperature in a 1000-year integration of a coupled atmosphere-ocean-land surface model, *Journal of Climate*, *9*(2), 376–393.

Minobe, S., A. Kuwano-Yoshida, N. Komori, S.-P. Xie, and R. J. Small (2008), Influence of the gulf stream on the troposphere, *Nature*, *452*, 206 EP –.

MIT News Office (2008), Edward lorenz, father of chaos theory and butterfly effect, dies at 90, http://news.mit.edu/2008/obit-lorenz-0416, accessed: 2019-03-10.

Moron, V., R. Vautard, and M. Ghil (1998), Trends, interdecadal and interannual oscillations in global sea-surface temperatures, *Climate Dynamics*, *14*(7), 545–569, doi:10.1007/s003820050241.

Morten, A. J. (2015), Spatio-temporal spectra and spectral transfers in fluid dynamics, Ph.D. thesis, University of Michigan, doi:2027.42/116695.

Moulin, A., and A. Wirth (2016), Momentum transfer between an atmospheric and an oceanic layer at the synoptic and the mesoscale: An idealized numerical study, *Boundary-Layer Meteorology*, *160*, doi:10.1007/s10546-016-0153-x.

Müller, M. (Ed.) (2009), *The Free Oscillations*, pp. 23–38, Springer Berlin Heidelberg, Berlin, Heidelberg, doi:10.1007/978-3-540-85576-7.

O'Rourke, A. K., B. K. Arbic, and S. M. Griffies (2018), Frequency-domain analysis of atmospherically forced versus intrinsic ocean surface kinetic energy variability in GFDL's CM2-O model hierarchy, *Journal of Climate*, *31*(5), 1789–1810, doi:10.1175/JCLI-D-17-0024.1.

Oxford English Dictionary online (), Definition of climate in english, https://en.oxforddictionaries.com/definition/climate, accessed: 2019-03-10.

Penduff, T., M. Juza, B. Barnier, J. Zika, W. K. Dewar, A.-M. Treguier, J.-M. Molines, and N. Audiffren (2011), Sea level expression of intrinsic and forced ocean variabilities at interannual time scales, *Journal of Climate*, *24*(21), 5652–5670, doi: 10.1175/JCLI-D-11-00077.1.

Porter, J., L. Xie, A. Challinor, K. Cochrane, S. Howden, M. Iqbal, D. Lobell, and M. Travasso (2014), Food security and food production systems, in *Climate Change 2014: Impacts, Adaptation, and Vulnerability. Part A: Global and Sectoral Aspects. Contribution of Working Group II to the Fifth Assessment Report of the Intergovernmental Panel on Climate Change*, edited by C. Field, V. Barros, D. Dokken, K. Mach, M. Mastrandrea, T. Bilir, M. Chatterjee, K. Ebi, Y. Estrada, R. Genova, B. Girma, E. Kissel, A. Levy, S. MacCracken, P. Mastrandrea, and L. White, book section 7, pp. 485–533, Cambridge University Press, Cambridge, United Kingdom and New York, NY, USA.

Quattrocchi, G., S. Pierini, and H. A. Dijkstra (2012), Intrinsic low-frequency variability of the gulf stream, *Nonlinear Processes in Geophysics*, *19*(2), 155–164, doi: 10.5194/npg-19-155-2012.

Renault, L., M. J. Molemaker, J. Gula, S. Masson, and J. C. McWilliams (2016), Control and stabilization of the Gulf Stream by oceanic current interaction with the atmosphere, *Journal of Physical Oceanography*.

Renault, L., S. Masson, V. Oerder, S. Jullien, and F. Colas (2019), Disentangling the mesoscale ocean-atmosphere interactions, *Journal of Geophysical Research: Oceans*, doi:10.1029/2018JC014628.

Salmon, R. (1978), Two-layer quasi-geostrophic turbulence in a simple special case, *Geophysical & Astrophysical Fluid Dynamics*, *10*(1), 25–52, doi: 10.1080/03091927808242628.

Salmon, R. (1980), Baroclinic instability and geostrophic turbulence, *Geophysical & Astrophysical Fluid Dynamics*, *15*(1), 167–211, doi:10.1080/03091928008241178.

Saltzman, B. (1957), Equations governing the energetics of the large scales of atmospheric turbulence in the domain of wave number, *Journal of Meteorology*, *13*, 513–523, doi:10.1175/1520-0469(1957)014<0513:EGTEOT>2.0.CO;2.

Scaife, A. A., C. K. Folland, L. V. Alexander, A. Moberg, and J. R. Knight (2008), European climate extremes and the north atlantic oscillation, *Journal of Climate*, *21*(1), 72–83, doi:10.1175/2007JCLI1631.1.

Scott, R. B., and F. Wang (2005), Direct evidence of an oceanic inverse kinetic energy cascade from satellite altimetry, *Journal of Physical Oceanography*, *35*(9), 1650–1666, doi:10.1175/JPO2771.1.

Sérazin, G., T. Penduff, S. Grégorio, B. Barnier, J.-M. Molines, and L. Terray (2015), Intrinsic variability of sea level from global ocean simulations: Spatiotemporal scales, *Journal of Climate*, *28*(10), 4279–4292, doi:10.1175/JCLI-D-14-00554.1.

Sérazin, G., T. Penduff, B. Barnier, J.-M. Molines, B. K. Arbic, M. Müller, and L. Terray (2018), Inverse cascades of kinetic energy as a source of intrinsic variability: A global ogcm study, *Journal of Physical Oceanography*, *48*(6), 1385–1408, doi:10.1175/JPO-D-17-0136.1.

Shevchenko, I., P. Berloff, D. Guerrero-López, and J. E. Roman (2016), On low-frequency variability of the midlatitude ocean gyres, *Journal of Fluid Mechanics*, *795*, 423–442, doi:10.1017/jfm.2016.208.

Simonnet, E., and H. A. Dijkstra (2002), Spontaneous generation of low-frequency modes of variability in the wind-driven ocean circulation, *Journal of Physical Oceanography*, *32*(6), 1747–1762, doi:10.1175/1520-0485(2002)032<1747:SGOLFM>2.0.CO;2.

Small, R., S. deSzoeke, S. Xie, L. O'Neill, H. Seo, Q. Song, P. Cornillon, M. Spall, and S. Minobe (2008), Air-sea interaction over ocean fronts and eddies, *Dynamics of Atmospheres and Oceans*, *45*(3), 274 – 319, doi: https://doi.org/10.1016/j.dynatmoce.2008.01.001, oCEANIC FRONTS.

Smith, R. D., M. E. Maltrud, F. O. Bryan, and M. W. Hecht (2000), Numerical simulation of the north atlantic ocean at 1/10°, *Journal of Physical Oceanography*, *30*(7), 1532–1561, doi:10.1175/1520-0485(2000)030<1532:NSOTNA>2.0.CO;2.

Steinberg, H. L., A. Wiin-Nielsen, and C.-H. Yang (1971), On nonlinear cascades in large-scale atmospheric flow, *Journal of Geophysical Research (1896-1977)*, *76*(36), 8629–8640, doi:10.1029/JC076i036p08629.

Stull, R. B. (1988), *An Introduction to Boundary Layer Meteorology*, Kluwer Academic Publishers.

Sutton, R. T., and D. L. R. Hodson (2005), Atlantic ocean forcing of north american and european summer climate, *Science*, *309*(5731), 115–118, doi: 10.1126/science.1109496.

Tennekes, H., and J. Lumley (1972), *A First Course in Turbulence*, MIT Press.

Vallis, G. K. (2006), *Atmospheric and Oceanic Fluid Dynamics*, Cambridge University Press, Cambridge, U.K.

von Storch, J.-S., H. Sasaki, and J. Marotzke (2007), Wind-generated power input to the deep ocean: An estimate using a 1/10° general circulation model, *Journal of Physical Oceanography*, *37*(3), 657–672, doi:10.1175/JPO3001.1.

Wills, R. C., T. Schneider, J. M. Wallace, D. S. Battisti, and D. L. Hartmann (2018), Disentangling global warming, multidecadal variability, and el nio in pacific temperatures, *Geophysical Research Letters*, *45*(5), 2487–2496, doi: 10.1002/2017GL076327.

Wilson, C. (2016), Does the wind systematically energize or damp ocean eddies?: Wind forcing of ocean eddies, *Geophysical Research Letters*, *43*, doi: 10.1002/2016GL072215.

Wilson, C., C. W. Hughes, and J. R. Blundell (2015), Forced and intrinsic variability in the response to increased wind stress of an idealized southern ocean, *Journal of Geophysical Research: Oceans*, *120*(1), 113–130.

World Meteorological Organization website (), What is climate variability?, http://www.wmo.int/pages/prog/wcp/ccl/faqs.php, accessed: 2019-03-10.

Zhai, X., H. L. Johnson, and D. P. Marshall (2010), Significant sink of ocean-eddy energy near western boundaries, *Nature Geosci*, *3*(9), 608–612.